Mechanical Characterization of 3D Printed Polylactic Acid (PLA)

Submitted in partial fulfilment of the requirements
for the award of the degree of

DOCTOR OF PHILOSOPHY
in
CIVIL ENGINEERING

by

Ganja Tejaswi Laxmi Priyanka

(Roll No: 714169)

Supervisor

Dr. T. P. Tezeswi

Associate Professor

ENGINEERING STRUCTURES DIVISION

DEPARTMENT OF CIVIL ENGINEERING

NATIONAL INSTITUTE OF TECHNOLOGY

WARANGAL- 506 004 (T.S.) INDIA

December 2022

NATIONAL INSTITUTE OF TECHNOLOGY

WARANGAL

CERTIFICATE

This is to certify that the thesis entitled '**Mechanical Characterization of 3D Printed Polylactic Acid (PLA)'** being submitted by **Ms Ganja Tejaswi Laxmi Priyanka** for the award of the degree of **Doctor of Philosophy** to the Faculty of Engineering and Technology of **National Institute of Technology, Warangal** is a record of bonafide research work carried out by her under my supervision and it has not been submitted elsewhere for award of any degree.

Dr. T. P. Tezeswi
Thesis Supervisor
Assosiate Professor
Department of Civil Engineering
National Institute of Technology, Warangal

Warangal (T.S.) – INDIA

APPROVAL SHEET

This Thesis entitled "**Mechanical Characterization of 3D Printed Polylactic Acid (PLA)"** by **Ms Ganja Tejaswi Laxmi Priyanka** is approved for the degree of Doctor of Philosophy.

Examiners

_____

_____

_____

Supervisor

_____

Chairman

_____

Date: _____

DECLARATION

This is to certify that the work presented in the thesis entitled **"Mechanical Characterization of 3D Printed Polylactic Acid (PLA)"** is a bonafide work done by me under the supervision of **Dr. T. P. Tezeswi** and was not submitted elsewhere for the award of any degree. I declare that this written submission represents my ideas in my own words and where other ideas or words have been included, I have adequately cited and referenced the original sources. I also declare that I have adhered to all principles of academic honesty and integrity and have not misrepresented or fabricated or falsified any idea / data / fact /source in my submission. I understand that any violation of the above will be a cause for disciplinary action by the Institute and can also evoke penal action from the sources which have thus not been properly cited or from whom proper permission has not been taken when needed.

_____

(**Ganja Tejaswi Laxmi Priyanka**)

(Roll No: **714169**)

Date: _____

Dedicated To

My

Family members

ACKNOWLEDGEMENTS

With great pleasure and proud privilege, I manifest my heartiest thankfulness to my research advisors, **Dr. T. P. Tezeswi**, Associate Professor Department of Civil Engineering, for their invaluable suggestions, sagacious guidance, scholarly advice and comprehensive critical remarks in bringing out this research work with artistry.

I express my sincere gratefulness to **Prof. T.D. Gunneswara Rao**, Head, Department of Civil Engineering and Chairman, Doctoral Scrutiny Committee for his enlightening guidance and immense help rendered in bringing out this work.

I am grateful and thankful to **Prof. C.B.Kameshwara Rao**, **Dr.M.V.N Sivakumar**, Associate Professor in the Department of Civil Engineering and **Prof. N.Narasaiah** in the Department of Metallurgical & Material Engineering, members of Doctoral Scrutiny Committee, National Institute of Technology, Warangal. For their guidance and help during the investigation. I would sincerely like to thank **Prof. Y.Ravi Kumar**, Department of Mechanical Engineering, National Institute of Technology, Warangal.

I am also thankful to **Prof. P. Rathish Kumar**, **Prof. Ramaseshu** the faculty members of Civil Engineering, **Dr. R.Arockia Kumar**, **Dr. Ajoy Kumar Pandey,** Associate Professors the faculty members of Metallurgical & Material Engineering, NITW for the moral support given during the period of research work.

I am also thankful to **Dr. T. P. Tezeswi** Division head, Engineering structures division NITW for the moral support given during the period of research work.

I thank my friends **Manmadha Chary, Navaneet Nandkishore Kabra, Kamlesh Kumar, Ch. Saideep, Kailas Milind, V. Harika, M. Vidhish Naik, V. Uday Kumar, Soumyashree Dixit, P. Madhuri, K. Swetha, V. Guru Prathap Reddy, Harsha Praneeth Pavani** and fellow research scholars for their direct or indirect suggestions throughout the period of my research work.

I am thankful to **Sri Md. Hussain** and Administrative staff for the help done during the research period.

Finally, I thank everyone, who contributed either directly or indirectly in the successful completion of this work.

- **G.T.L Priyanka**

ABSTRACT

Additive manufacturing is the technology of making objects directly from a computer aided design model by adding a layer of material at a time in contrast to conventional subtractive manufacturing methods which involve removing material to reach the desired shape. One of the most popular additive manufacturing techniques (3D printing) is fused deposition modelling (FDM), which is based on adding melted material layer by layer.

The material characterization of 3D printed structures to obtain parameters such as strength and stiffness is a time consuming and costly process which can be simplified by the testing of the fundamental units, which are the extruded strands.

Towards this, single strands and multiple extruded filaments with/without overlap of PLA material with different gage lengths are tested for axial tensile modulus, ultimate strength and failure strain. A probabilistic strength prediction model is developed wherein the 2-parameter Weibull distribution is used to determine the probability of failure of extruded strand material at a particular stress.

To enable prediction of strength of 3D printed parts as a function of porosity, a material strength model is developed for 3D printed PLA materials subjected to quasi-static loading.

Various failure criteria are considered to predict the strength of 3D printed PLA for combined loads. By using the mechanical properties from quasi-static tensile and compression specimens printed at various orientations (0^o, 30^o, 45^o, 60^o, 90^o) and the failure envelope curves for PLA is obtained. To generate failure surfaces MATLAB code is used in this study.

For designing components exposed to extreme loading situations, it is essential to characterize the high strain rate response of 3D printed (fused deposition modelling) materials. In this study, uniaxial quasi-static and dynamic compressive tests were carried out at various strain rates (10^{-2} s^{-1} and 200 s^{-1} to 1800 s^{-1}) for 3D printed PLA. Strain rate dependent compressive response of Polylactide acid (PLA) disk specimens 3D printed at 0^o, 45^o and 90^o orientations was obtained using the Split Hopkinson bar technique. The results show that the compressive strength increases with corresponding strain rates for 0^o and 45^o print orientations. PLA printed at 0^o

has higher compressive strength compared to 45^{o} and 90^{o} orientations under quasi-static as well as high strain rate loading. Toughness was observed to increase with strain rate in all three orientations. A simple modification to the Johnson-Cook model is then proposed, which accounts for the effects of print orientation, porosity and strain softening behaviour.

The dynamic mechanical analysis (DMA) is conducted for 3D printed PLA specimens, produced in different orientations i.e., 0°, 30^{o}, 45° and 90° to determine the viscoelastic properties such as elastic (storage) modulus, loss (viscous) modulus, and tan delta as a function of frequency and temperature.

Contents

List of Tables

List of Figures

ABBREVIATIONS

Symbols

%	Percentage
*	Multiplication
R^2	Correlation Coefficient

Units and Measures

µm	Micrometer (micron)
η	scale parameter
β	shape parameter
R	Reliability
MPa	Mega Pascal
mm	Millimeter
m	Meter
n	Porosity
m	Emperical Constant
cm	Centimeter
exp	Exponential
a	Dimensions of a strand
b	Dimensions of a strand
α	Vertical or horizontal overlapping coefficients
β	Vertical or horizontal overlapping coefficients
n	Porosity
Ra	Arithmetic mean of the absolute values
Rz	Mean peak to – valley height
N	Newton
kN	Kilo Newton
ε	Strain

ε_u	Strain corresponding to ultimate stress
^oC	Temperature
µm	Micrometer (micron)
s	Second
o	Degree
Hz	Frequency
c/s	Cross section
J	Joule
MPa	Mega Pascals
v	Volume
σ	Stress
E	Young's Modulus
p	Porosity
M	Mega

Text Abbreviations

1D	One Direction
3D	Three Dimensional
ABS	Acrylonitrile Butadiene Styrene
AM	Additive Manufacturing
ASTM	American Society for Testing and Materials
CAD	Computer Aided Design
CT	Computed tomography
DMA	Dynamic Mechanical Analysis
Eq	Equation
FDM	Fused Deposition Modelling
FEA	Finite Element Analysis
ISO	International Organization for Standardization
JC	Johnson-cook
MEFWNO	Multiple Extruded Filaments WITHOUT Overlap

MEFWO	Multiple Extruded Filaments WITH Overlap
PC	Polycarbonate
PEEK	Poly ether ether ketone
PLA	Polylactic Acid
SEF	Single Extruded Filaments
SHPB	Split Hopkinson Pressure Bar Technique
STL	Stereo lithography
UTM	Universal Testing Machine
WPP	Weibull Probability Plot

CHAPTER 1

INTRODUCTION

1 Background to the study

Additive Manufacturing (AM) or 3D printing is broadly used for several applications in architecture, bio-medicine, aerospace, defence, semi-conductor, construction, and automotive engineering(Gibson, Kvan, and Ming 2002; Ngo et al. 2018; Sun et al. 2004; Campbell and Gibson 2012). It enables the creation of complex 3D physical models by layer wise deposition of extruded filaments through a layered process using Computer Aided Design (CAD) data. The ISO/ASTM 52900:2015 (ISO 17296-2 2015)standard classifies all AM processes into seven major categories: directed energy deposition (DED), vat photopolymerization (VP), powder bed fusion (PBF), binder jetting (BJ), material jetting (MJ), sheet lamination (SL), and material extrusion (ME). However, the current classification of AM is broadly in terms of raw materials being used: solid, liquid on powder based and is reported to be inconsistent due to the use of different materials at the same time in some AM processes (Altıparmak and Xiao 2021).

Many polymers like Polylactide (PLA), Acrylonitrile butadiene styrene (ABS), Polyetheretherketone (PEEK) and Polycarbonate (PC) filaments are commonly used for AM using solid filaments or wires (Hoskins, Dearn, and Kukureka 2018). Plastics have many advantages such as lower cost and easy formability for various complex designs using 3D printing (Dizon et al. 2018a). Of these, polylactide (PLA) is a biodegradable material which is considered in the current study due to its ubiquity, biodegradability and sustainability (Gross and Kalra 2002; Ayrilmis 2018a; Jašo et al. 2015).

Several studies have been conducted by researchers to characterize the mechanical properties of 3D printed materials such as PLA (Polylactic acid), ABS (Acrylonitrile Butadiene Styrene), PEEK (Poly ether ether ketone) and PC (Polycarbonate) etc (Clark et al. 2017; Chacón et al. 2017; Cantrell et al. 2017; Hoskins, Dearn, and Kukureka 2018). Among 3D printed materials available, PLA is a biodegradable polymer with excellent mechanical properties (Y. Wang et al. 2020; Gross and Kalra 2002; Raj, Muthukumaran, and Jayakrishna 2018; Si et al. 2018b). Due to its many favourable characteristics, PLA is used in packaging and biomedical applications such as controlled release of chemicals/drugs, prosthetic devices, bone screws or scaffolding for tissue engineering (Si

et al. 2018a; Beheshtizadeh et al. 2020; Olewnik-Kruszkowska, Nowaczyk, and Kadac 2017). Therefore, it is important to investigate and understand the mechanical properties and behaviour of PLA under various loading conditions.

The influence of parameters such as infill percentage, raster orientations, infill density, printing speed, nozzle temperature, bed temperature and variations of layer thickness on properties of 3D printed PLA compressive strength, tensile strength and impact or flexural strength has also been studied previously (Dizon et al. 2018b; Popescu et al. 2018).

Mechanical properties of 3D printed materials exhibit intrinsic dependence on the orientation of the deposition as well as inhomogeneity and anisotropic characteristics of the fused material. Extruded filaments are fundamental building blocks and principal load-carrying components of 3D printed materials. The characteristics of extruded filaments significantly influence the effective meso-mechanical and damage characteristics of the fabricated parts, knowledge of which is essential for mechanical analysis of 3D printed parts. The 3D printer builds components by extruding a semi-molten filament through a heated nozzle in a pattern onto a heated bed. Upon cooling, the deposited material solidifies and bonds with the surrounding extruded filament material, thus creating a 3D component.

3D printed objects may be subjected to dynamic loading in many applications due to impact or shock loading. During extreme loading scenarios, such as bird impact on aerospace structures and automotive accidents, the safety-related material parts are expected to absorb energy while exposed to extremely high strain rates and temperatures. Therefore, it is critical to characterize the mechanical behaviour of 3D printed components subjected to high strain rates of loading. The Split Hopkinson Pressure Bar Technique (SHPB) is widely used for investigating material behaviour at high strain rates. Strain rates in the range between 10 s^{-1} to 10^4 s^{-1} can be achieved using this technique.

1.1 Aim and Objectives

1.1.1 Aim:

Development of rate dependent constitutive model for 3D Printed PLA material.

1.1.2 Objectives:

i. Characterization of mechanical properties and prediction of strength of single strands and multiple strands without overlap and multiple strands with overlap extruded form filaments during 3D printing.

ii. Application of available simple material constitutive models for predicting strength of 3D printed tension specimens.

iii. Developing analytical methodology for predicting the effect of overlapping on the strength of 3D printed PLA tension specimens.

iv. Characterization of mechanical properties of tensile specimens (i.e., dog-bone specimen) of orientation 0°, 30°, 45°, 60° and 90°.

v. Characterization of mechanical properties of compressive specimen (i.e., prism specimen) of orientation 0°, 30°, 45°, 60° and 90°.

vi. Development of a failure criteria as applicable to 3D printed PLA.

vii. Characterization of high strain rate behaviour of 3D printed PLA.

viii. Dynamic mechanical analysis for determining visco-elastic properties of 3D printed PLA.

1.2 Scope and limitations of the present investigation

An analytical model based on reduction in mechanical properties due to porosity, and accounting for overlapping of strands, has been developed, and compared with analytical based micro-mechanical models of 3D printed meso-structure. The effects of temperature, filament diameter and length on high strain rate response have not been included in the present study.

1. **Specimen types**:

    a. 3D printed single extruded filaments

b. Multiple extruded filaments with overlap

c. Multiple extruded filaments without overlap

d. Tensile specimens (0°, 30°, 45°, 60° and 90° orientations).

e. Compressive specimens (0°, 30°, 45°, 60° and 90° orientations).

f. Three point-bending (0°, 30º, 45° and 90° orientations).

2. **Experiments**:

   a. ***Tensile testing***- Strands (ASTM D3379-75)

   b. ***Quasi static Testing of Components*** - Tensile (Dog-bone, ASTM D638) and compressive testing (Prism, ASTM D695).

   c. ***High strain rate (SHPB) testing*** - Disk specimens.

   d. ***Dynamic mechanical testing*** – 3 point bending (Rectangular, ASTMD5023-07).

3. **Failure criteria:** Tsai-Hill, Tsai-Wu, Hoffman, Rankine and Tresca.

4. **Rate Dependent Model:** Modification of JC model to account for print orientation and porosity.

5. **DMA analysis:** Results are presented for temperature scanning up to 70ºC for along with two types of tests are conducted on the specimens- i) Varying temperature and frequencies, ii) Varying frequency. Test one is temperature scanning with multi–frequency (1Hz, 3Hz, and 5Hz), and test two is conducted at ambient temperature with a frequency range from 1-200 Hz.

1.3 Thesis Organization

The thesis is organized as follows:

Chapter 1 of the thesis focuses on the background and the necessity of the study, introduction to Additive manufacturing and coming up with problem statement. The chapter also defines aim, objectives, scope and significance of the current study.

Chapter 2 of the thesis reviews the literature on Additive manufacturing, PLA material characterization, biodegradability of PLA, reliability, porosity, failure criteria, high –

strain rate characterization and dynamic mechanical analysis. The literature gaps are then summarized.

Chapter 3 of the thesis details the research methodology used in the study. In this chapter the systematic procedure used for achieving the desired objectives is discussed. Based on this, the research questions and methodology are developed. The current study is categorized in five phases. All the five phases of the project are discussed under subsequent chapters.

Chapter 4 of the thesis details the tensile experiments on 3D printed single strands and Weibull analysis for strength prediction.

Chapter 5 of the thesis deals with the analytical procedures for prediction of strength and stiffness are then developed.

Chapter 6 of the thesis investigates failure criteria of 3D printed PLA.

Chapter 7 of the thesis investigates high strain rate characterization of 3D printed PLA.

Chapter 8 of the thesis presents results of dynamic mechanical analysis of 3D printed PLA.

CHAPTER 2
LITERATURE REVIEW

2 Introduction

In the present chapter, extensive research conducted in the field of 3D printing is summarized. This section presents a report on the development of failure criteria, high strain rate characterization using SHPB and DMA.

2.1 Review of Literature on 3D printing

John Ryan C. Dizona et.al., (2018), discussed various methods of additive manufacturing (AM) and its technologies were described. Various mechanical testing methods of ASTM and ISO for 3D printed polymers were discussed. Experimental investigations for various AM methods for different materials were performed with a special focus on properties at low temperatures (Dizon et al. 2018a).

L.G. Blok et.al., (2018), Planted carbon fibres into a thermoplastic matrix to improve its strength and stiffness. 3D printing of short and long fibre of carbon was characterized. It was concluded that the mechanical properties of continuous fibre showed better results compared to unidirectional epoxy matrix composites. It was observed that continuous fibres have diminished design freedom due to their brittle nature, while short microfibres showed better printing capabilities. However, the increase in mechanical properties due to short microfibres was marginal (Blok et al. 2018).

Wenzheng Wu et.al., (2015), studied the effect of layer thickness and raster orientation on the strength of 3D printed PEEK. Mechanical properties of PEEK specimen for various layer thicknesses, print orientations were investigated and compared to that of ABS specimen. It was observed that the PEEK specimen of 300µm layer thickness with 0^o print orientation produced the best results. This study concluded that the strength characteristics of PEEK were superior to that of ABS (Wu et al. 2015).

Todd Letcher et.al., (2014), examined the strength and fatigue characteristics of 3D printed PLA for various print orientations (0°, 45° & 90°). In the case of tensile strength, 45° print orientation showed to favourable results while 0° specimen produced better flexure strength. Fatigue testing result was inconclusive. It was observed that filament

strength and strength of 3d printed materials was almost the same (Letcher and Waytashek 2014).

Daniel Farbman et.al., (2016), looked at 3D-printed test specimens with printing parameters such as infill percentage & geometry (hexagonal, rectilinear), loading parameters such as orientation and strain rate were evaluated. Experimental results were then compared with finite element models. It was observed that the hexagonal pattern infill generated favourable mechanical properties, whereas finite element analysis showed lower deformation for rectilinear geometries. This inconsistency may be due to stress concentration in experimental samples (Farbman and McCoy 2016).

Prasanna Kumar Ilankeeran, et.al., (2012), elaborated on the importance of mechanical and damage properties of fibres used in composites. They studied mechanical properties such as axial tensile modulus, ultimate strength and strain at failure of carbon and glass single fibre. ASTM D3379-75 standard was followed for the aforementioned tests. It was observed that carbon single fibre produced high strength properties where glass fibre had high failure strain. Statical analysis was performed results on numerous experimental specimens (Ilankeeran, Mohite, and Kamle 2012).

Y. Song, et.al., (2017), investigated mechanical properties of specimens cut from fully dense PLA blocks having unidirectional filaments were studied. It was observed that the plastic behaviour of the material was orthotropic and showed tension-compression asymmetry. When the material was loaded in a longitudinal direction it exhibited higher stiffness. The results were then compared to that of injection-moulded homogenous PLA, which showed that 3D printed specimens promised better results. Voids can be reduced by opting for better printing parameters such as temperature and speed of extrusion. Both injection-moulded and 3D printed PLA produces a similar elastic response. It was observed that the specimen showed brittle behaviour when tested out-of-plane (Song et al. 2017).

Heechang Kim, et.al., (2017), investigated, the tensile strength of 3D printed PLA & ABS for various experiment variables are studied. The results of the single-material specimen were compared with dual-material printed specimens to assess their structural effectiveness. In the case of a single material experiment longitudinal with a 100% infill

ratio showed favourable results. Voids and overlap at the boundary of two materials is observed while fabricating the dual-material specimen (Kim et al. 2017).

Vladimir E. Kuznetsov, et.al., (2018), assessed specimens printed using different nozzle diameters and for various layer heights were assessed. It was observed that for a given layer height, strength was more for higher nozzle diameters. Strength decreased when layer height increases. To estimate the strength of 3D printed samples a new method was proposed. To avoid critical direction, tubular samples were checked for flexural strength. SEM analysis was conducted to detect the reason for failure in the specimen (Kuznetsov et al. 2018).

Anoop Kumar Sood, et.al., (2010), investigated the effect of process parameters like layer thickness, raster orientation, angle & width and air gap on the mechanical properties of 3D printed materials is studied. To reduce the experimental runs CCD was used. The relation between response and process parameters was obtained using empirical models. The models were validated by the variance of analysis using ANOVA. The optimal parameter setting for each response was obtained using response surface plots. For maximizing responses simultaneously, the desirability function was used (Sood, Ohdar, and Mahapatra 2010).

L. Li and Q. Sun, et.al., (2002), determined the constitutive models of 3D printed ABS theoretical and experimental analyses. As part of theoretical calculation, void density was studied. Microscopic analysis was performed to determine void density, for the longitudinal and transverse directions of the fibre. If the negative gap was low voids appeared at equal intervals. When the negative gap increased, dimension accuracy and surface quality decreased. Stiffness properties for various print parameters such as deposition densities and orientations were assessed. To determine the elastic constants (Young's and shear modulus) a set of equations was proposed. The analytical results were compared with experimental results (L. Li et al. 2002).

Céline Bellehumeur, et.al., (2004), investigated bond formation between filaments of 3D printed ABS. Under the process of 3D printing semi-molten adhesive bond developed. To assess the bond formation between filaments, sintering experiments were done at constant and ramped temperatures. Qualitative prediction was made based on experimental results to determine the degree of bonding. Better cooling conditions may

have a good effect on the final part manufactured using FDM process (Bellehumeur et al. 2004).

Lalit Singh Mehta, et.al., (2017), looked at the compressive strength of cylindrical specimens made of 3D-printed PLA with a nozzle size of 0.25mm. Cylindrical samples were modelled in solid works software and ultimaker was used as a 3D printing machine. Cura was used as a slicer engine for ultimaker. As fill density increases, the compressive strength of the specimen also increases (Mehta, Pillai, and Mehta 2017) .

Ahn et.al., (2002), used Fused Deposition Modelling (FDM) 1650 for characterizing ABS parts (P400) properties, because studying ABS parts properties is very essential to understand FDM parts mechanical behaviour. The effect of various parameters of ABS plastic such as raster orientation, air gap, bead width, colour, temperature on tensile strengths and comprehensive strengths was studied using the design of experimental analysis (Ahn et.al., 2002). From their experimental analysis, it was found that air gap and raster orientation exercise a profound effects on tensile strength while Bead width, model temperature and colour have minimal effects. From the comparative analysis of tensile and comprehensive strengths in terms of raster direction, it was found that comprehensive strength has relatively higher strength than tensile strength. Hence, the authors have recommended build rules to improve the strength and quality of FDM parts(Ahn et al. 2002).

Barbero et.al., (2000), has studied the mechanical behaviour of composite materials through Statistical analysis (Barbero et.al., 2000). In this study the authors have used two-parameter Weibull statistic static method for analysis of strength properties of on the basis of sample size (P_A & P_B) and estimation method. A total of 30 samples were used for 3 point bending test and from their experiments they have concluded that the probability of strength of A base material was 694, 745 and 749. The probability of P_A base material is 99.9%, 99.7% and 99.7%. Similarly, the probability of estimation method for B base material strength was 834, 853 and 857. Whereas, the probability of P_B is 97.2%, 95.6% and 95.1% (Barbero, Fernández-Sáez, and Navarro, n.d.).

Ghosh et.al., (1999), developed a computer program for estimating the samples mechanical strength by using two-parameter Weibull distribution. Two methods, such as linear regression and maximum-likelihood estimator methods, were employed to study

Weibull modulus and scale parameters (Ghosh et.al., 1999). In addition, order statistics were employed for estimation of the cumulative distribution function. The computer program code is verified by taking into account of 2 published data sets, one data set of drought data and one data set carrying information of carbide insects. The estimation results from the computer program were compared with the published graphical results. Finally, from their computer code analysis, they have concluded that the estimated datasets were in agreement with the original data (Ghosh, n.d.).

AI selmy et.al., (2013), analysed experimental results statistically using two-parameter Weibull distribution function. The experimental results which looked at tensile strength, tensile strain at failure and young's modulus showed these were scattered with Weibull distribution. Also, they studied failure probabilities. From the curve fitting concept, the authors concluded that the predicted and experimental results were in agreement with each other. Hence, they concluded that Weibull distribution can be used as one of the versatile functions to study the mechanical strength of composite materials (Selmy, Azab, and El-Baky 2014b).

Baojiang et.al., (2012), has studied the aeronautical engineering composite materials tensile strength by using Weibull distribution. Abnormal data, estimate parameters and assumed distribution were studied by using Maximum normed residual (MNR) test, graphical methods and Kolmogorov test respectively (Baojiang et.al., 2012). From the comparative analysis of predicted and measured values, it was observed that there was only slightly deviation accounting for 0.24%. Hence, the authors have concluded that Weibull distribution can be employed to study the tensile strength of composite materials (Du et al. 2012b).

Joffe et.al., (2009), tested single filaments and bundles of Cordenka 700 Super fibres by using three parameter Weibull distribution due to non-linear behaviour of fibres. These fibres are of great importance because they have application as reinforcement in polymer composites. The strength of the bundle fibres was studied by using microwave drying for 50^{o}C 24 hours and then the samples were immediately tested. It was clear that drying of the fibre resulted in increase of strength and reduction of single fibre properties. They have also reported that the bundle of fibres will prevent failure but stress is a limiting factor. They further concluded that the properties of the fibres are highly non-linear exhibiting visco-elastic behaviour (Joffe, Andersons, and Spārniņš, n.d.).

2.2 Review of Literature on Failure criteria

NT Mascia et.al., (2013), studied the failure criteria for orthotropic material such as Hill, Tsai-Hill, Tsai-Wu, Hoffman and Norris for wood species such as pinus elliotti and goupia glabra. Tensile and compressive strength were tested along the x-axis and y-axis and shear tests were conducted. Theoretical failure criterion was compared with experimental results using Mathematica software. The first (tension - tension), second (tension - compression), third (compression - compression) and fourth quadrant (compression - tension) strength values have taken. They concluded Hoffman criterion shown best result for strength evaluation (Mascia and Simoni 2013).

JM Cabrero et.al., (2012), developed failure theory for composite materials. This researcher applied the same failure theory for orthotropic material i.e., wood. The specimen orientations such as 0^o, 7.5^o, 15^o, 30^o and 45^o were collected from literature (Eberhard Steiner, 2002) for uniaxial and multiaxial (transversal and longitudinal tension) testing. The results were analysed with Failure theories such as linear and quadratic criteria – Quadratic, Vonmises, Tsai-Hill, Norris and Tensor derived criteria has applied for wood material. It was concluded that biaxial stress state is best to predict failure (Cabrero et al. 2012).

M Koca et.al., (2014), investigated failure behaviour of fibre-reinforced composites (for 0°, 5°, 15°, 30°, 45°, 60°, 75°, and 90° fibre angles) using Four-Point bending test is investigated. Tsai-Wu, maximum stress, maximum strain, Hashin, Tsai-Hill, Hoffman and quadric surfaces failure theories were studied for fibre-reinforced composites. And also, analytical modelling classical lamination theory (CLT) and numerical modelling using finite element method (FEM) were compared with experimental behaviour of materials (Nur Koç et al. 2014).

N Nyambeni et.al., (2018), Under thermomechanical loading and failure criteria for laminated composite structure. The stacking sequences (90^o; 0^o; 45^o; -45^o;90^o; 90^o; -45^o; 45^o; 0^o; 90^o) of graphite/epoxy lamina were restricted to ten layers. Mathematical modelling was used based on classical lamination theory, Failure theories were employed to test Tsai-Hill, Tsai-Wu & Hoffman criteria while numerical computations were done using MATLAB code. Failure occurs for a value less than 1 which indicates the structure will not fail or if the value is greater than 1, the structure will collapse. It was also

concluded that (graphite/epoxy) structure is safer compared to other materials (Nyambeni and Mabuza 2018).

2.3 Review of Literature on High strain rate characterization

Y.C Lin et.al., (2010), studied the effect of alloy steel characteristics like flow stress, strain rate and forming temperature using Johnson-Cook (JC) model, Zerilli-Armstrong (ZA) and combined JC-ZA model has been developed based on experimental results. Cylindrical specimens were made 10 mm in diameter and 12 mm in height. Compression tests were performed with three different strain rates 1 s^{-1}, 10 s^{-1} & 50 s^{-1} and with a temperature range of 850 – 1150^{o}C. In the JC model, the difference in testing strain rate and reference strain rate increases, and the prediction accuracy decreases. Also, as the difference in testing temperature and reference temperature increases, the error in predictions increases. It results in a modified JC-ZA model, which provides more accurate results of flow stress compared to JC and ZA models (Lin and Chen 2010b).

F. Gomes et.al., (2019), compared quasi-static and dynamic tests conducted for Split Hopkinson pressure bars (SHPB) for compressive behaviour of pinus pinaster Ait along radial (0^{o}) and tangential (90^{o}) axes. Both quasi-static and dynamic tests were performed for the digital image correlation technique to determine in-plane strain fields across the region of interest of specimen. Compression tests were performed on rectangular prismatic specimens along the radial and tangential directions coupled with digital image correlation. In case of radial and tangential directions for both quasi-static to dynamic tests, the modulus of elasticity, yield stress increases & poisson's ratio were found to reduce (Gomes, Xavier, and Koerber 2019).

Xin Li et.al., (2016), used carbon fibre with epoxy resin for two types of fabric warp-knitted and plain weave, to test quasi-static and dynamic strain rates. The compressive and tensile tests were performed to study the effect of strain rate. The laminate sequence for carbon fibre was [-45^{o}/0^{o}/45^{o}/90^{o}]. It shows that the average quasi-static tensile strength of the warp-knitted fabric is higher than plain weave carbon fabric. As the strain rate increases, the dynamic tensile strength also increases for both warp-knitted and plain weave carbon fibre. In the case of dynamic compressive tests, warp-knitted fabric shows a weaker strain rate effect than plain weave (X. Li et al. 2016).

2.4 Review of Literature on Dynamic Mechanical Analysis (DMA)

K. Arunprasath et.al., (2022), studied the viscoelastic behaviour of 3D printed polymers using Dynamic mechanical analysis (DMA) technique. The properties of DMA for 3D printed ABS and PLA with tension mode for temperature (-10 to 120 ^{o}C), absorbing, storage and dissipating behaviour of specimens were studied. In case of energy storing capacity, it was concluded that, ABS at 90^{o}C and PLA at 48^{o}C were the maximum temperature. Higher energy dissipation in the form of heat was seen for ABS from 110^{o}C and for PLA from 58^{o}C, which was proof of poor energy dissipation. Degree of crystallinity of PLA decreases at 55^{o} C whereas it increases up to 95^{o}C for ABS (Arunprasath et al. 2021).

Shuheng Wang et.al., (2020), derived AM of PLA mechanical properties for tensile and dynamic mechanical properties based on parameters such as printing orientation, layer thickness of 0.1mm and 0.2 mm, infill rate and nozzle temperature. In the case of tensile mechanical properties of print orientation, the bonding strength between 0^{o} - 90^{o} depends on interlayer and intralayer fractures. The increase in layer height causes an increase in interlayer air gaps. Therefore, it results in the bonding strength being reduced. As fill rate increases, the elastic modulus, tensile strength and elongation at break increase. Mechanical properties will be better only when 210^{o}C – 215^{o}C nozzle temperature occurs (S. Wang et al. 2020).

2.5 Literature gap

After a thorough literature review, it was observed that:

- There exists little data on reliability characteristics of 3D printed PLA materials. Previous studies on tensile mechanical behaviour of 3D printed PLA have primarily focused on variation in strength based on build orientation. To the authors knowledge, no study exists on the probabilistic strength characterization of 3D printed strands.

- Further, to the author's knowledge, there is a lack of data on the effects of length scaling on strength characteristics of extruded filaments in the literature.

- There is lack of published literature on failure criteria suitable for 3D printed polymer materials.
- There is lack of published research on high strain rate response of 3D printed PLA.
- Studies of visco-elastic response of 3D printed materials are also scarce.

CHAPTER 3

METHODOLOGY

3 Introduction

In this chapter the procedures employed in this study are systematically discussed. In the current work both experimental and analytical methods are used. The study was conducted in 5 phases:

Phase - 1 of the project work deals with experimental investigation of single extruded filaments long with/without overlap followed by Weibull statistical analysis.

Phase - 2 of the project studies the effect of porosity as well as overlap between adjacent strands, on the strength and modulus of the material.

Phase - 3 of the project presents results of experimental investigation of 3D printed PLA of tensile and compressive strengths based on ASTM standards followed by failure criteria determination.

Phase - 4 of the project presents the characterization of rate dependent compressive mechanical behaviour of 3D printed PLA printed at 0^o, 45^o & 90^o orientations. High strain rate (SHPB) tests are conducted at ambient temperature to characterize dynamic response. A simple empirical flow stress model based on modification of Johnson-Cook model is proposed in this study, which accounts for the effects of print orientation, porosity and strain softening behaviour in PLA.

Phase - 5 of the project presents the dynamic mechanical analysis (DMA) conducted for 3D printed PLA specimens, produced in different orientations i.e., 0°, 30^o, 45° and 90° to determine the viscoelastic properties such as elastic (storage) modulus, loss (viscous) modulus, and tan delta as a function of frequency and temperature.

3.1 Detailed phases of the research work:

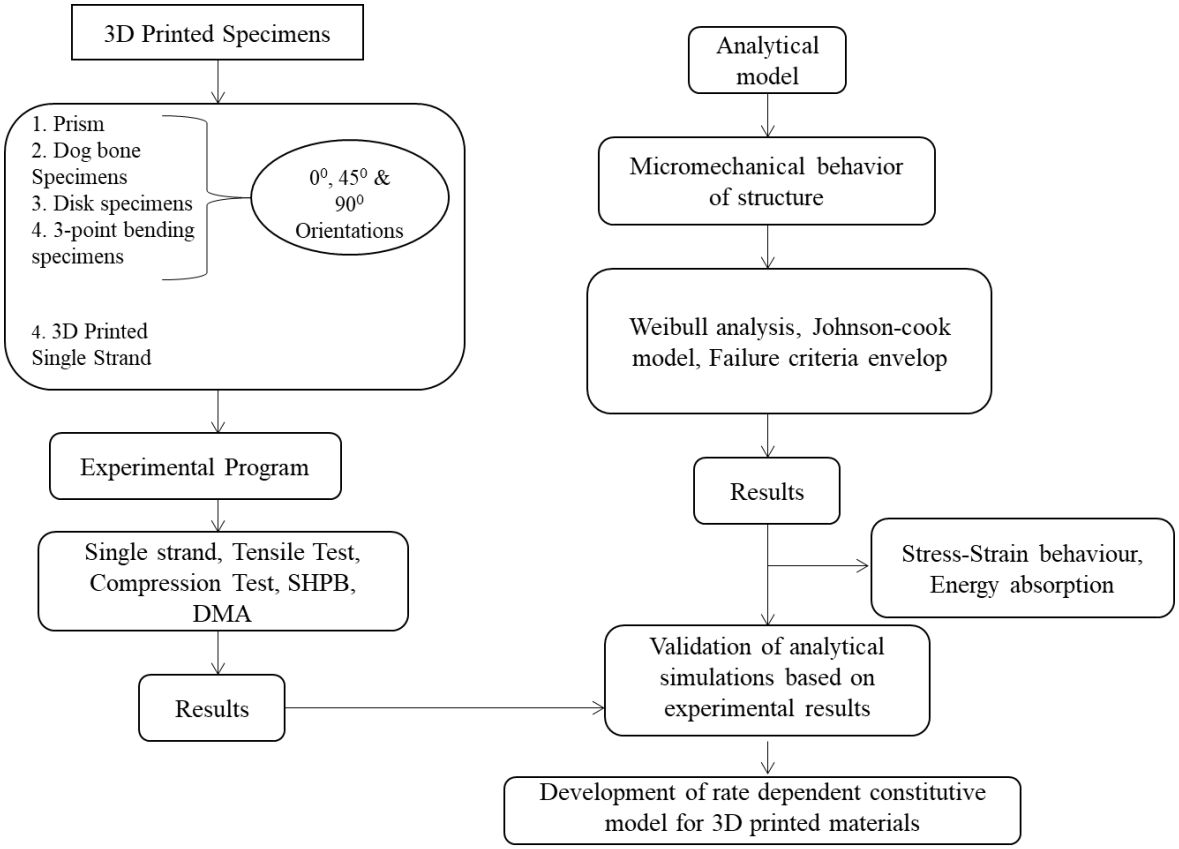

Figure 3.1: Overview of research work

3.1.1 Phase-I

Experimental characterization of mechanical properties of the individual strands of 3D printed PLA material.

Phase-1 of the research consists of:

i. Uniaxial tensile test on Single Extruded Filaments (SEF).

ii. Uniaxial tensile test on Multiple Extruded Filaments Without Overlap (MEFWNO) specimen.

iii. Uniaxial tensile test on Multiple Extruded Filaments With Overlap (MEFWO) specimen.

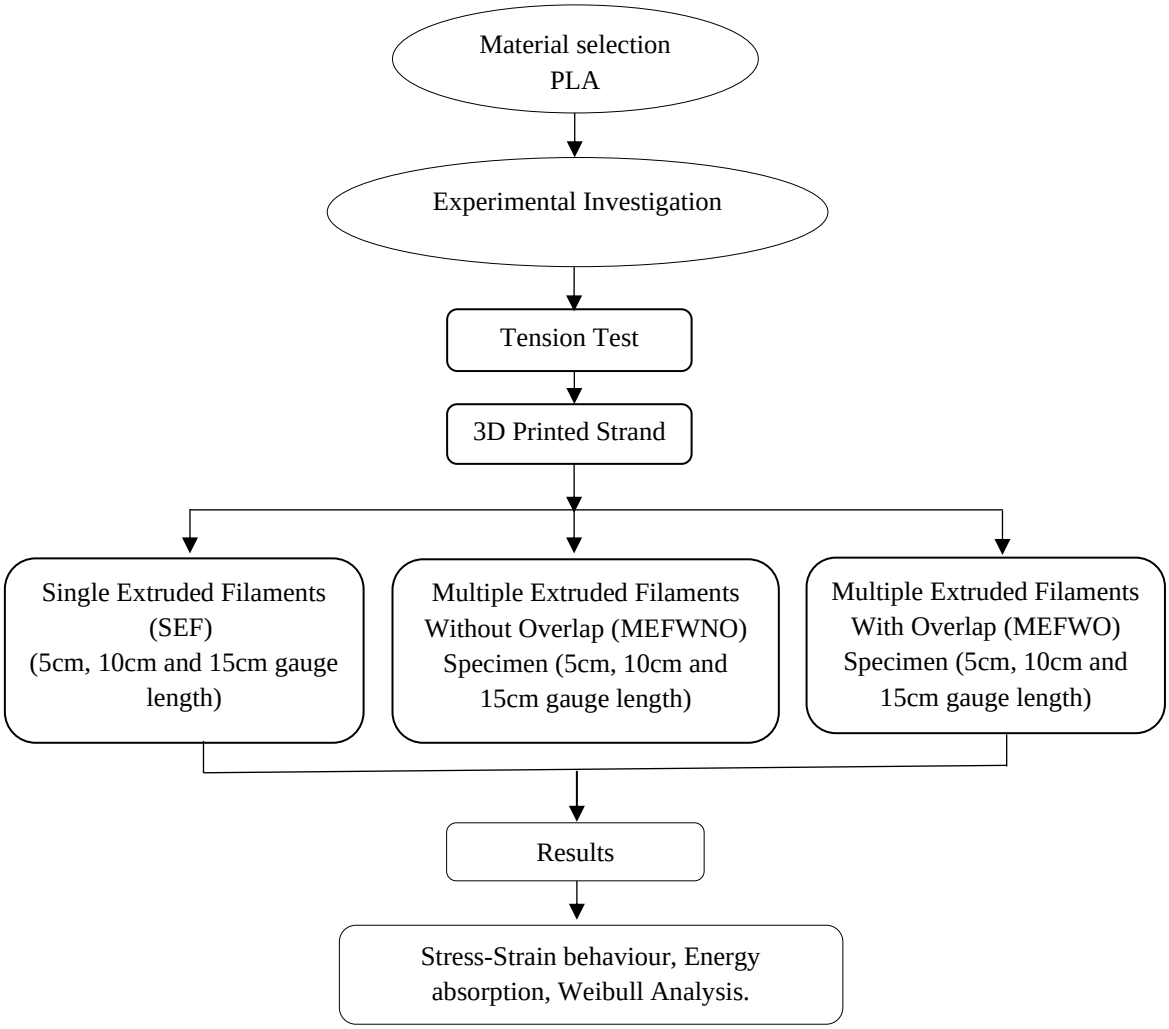

Figure 3.2: Overview of Phase-I

3.1.2 Phase-II

Based on the results of phase-I, micromechanical behavior is analyzed in phase-II. The effect of different overlapping lengths on the strength of 3D printed specimens, was looked at elliptical shape strands used. Porosity parameter is used to study the variation of strength with overlapping length and without overlapping length. The effect of porosity on strength and stiffness models are studied.

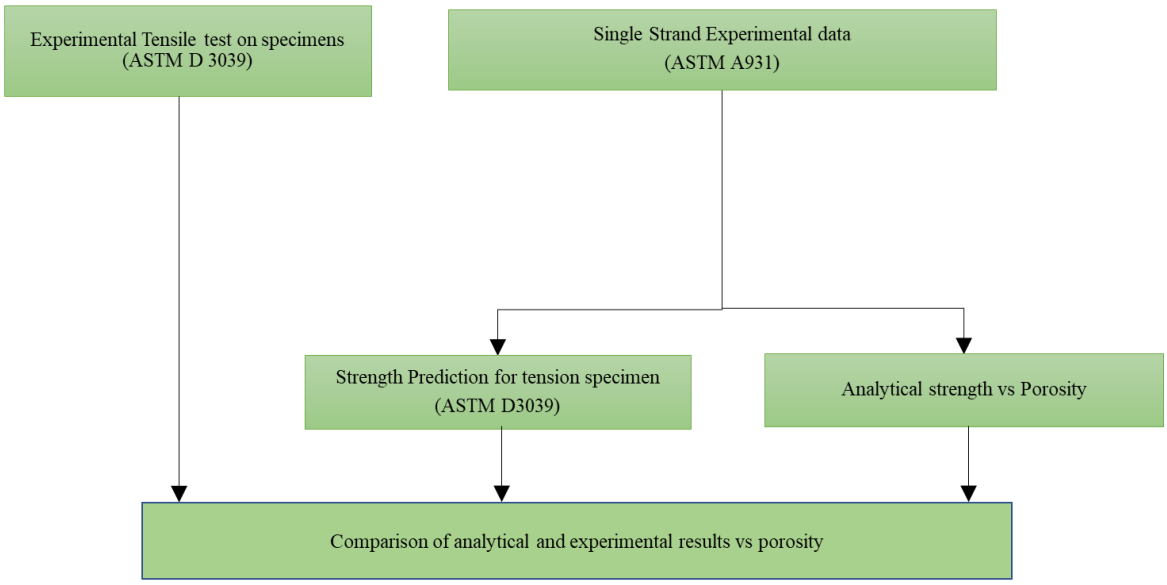

Figure 3.3: Overview of Phase-II

3.1.3 Phase-III

Phase-III developed failure criteria of 3D printed PLA specimens at 0^o, 30^o, 45^o, 60^o & 90^o orientations based on quasi-static compression and tensile results. In this phase, failure criteria is considered to predict the strength at combined loads. Using the mechanical properties and the equations of each failure criterion, the failure envelope surface for 3D printed PLA is achieved.

3.1.4 Phase-IV

This phase-IV focuses on characterizing the rate dependent compressive mechanical behaviour of 3D printed PLA printed at 0^o, 45^o and 90^o orientations, which is considered in this study due to its ubiquity, biodegradability and sustainability. Quasi static compression tests are conducted on specimens with 100% infill, which enables quantification of the effect of print orientation on strength properties. High strain rate (SHPB) tests are conducted at ambient temperature to characterize dynamic response. A simple empirical flow stress model was proposed in this study, which accounts for the effects of print orientation, porosity and strain softening behaviour in PLA.

3.1.5 Phase-V

Phase-V aims to characterize the dynamic mechanical analysis of 3D printed PLA at 0^o, 30^o, 45^o and 90^o orientations is to determine viscoelastic properties such as elastic

(storage) modulus, loss (viscous) modulus and tan delta as a function of frequency, temperature are significant transitions in the thermomechanical behaviour. A rectangular specimen, was chosen for the present study to study its visco-elastic behaviour. The reference standard for the determination of the dynamic mechanical properties of plastic materials is "ASTM D5023-07 Standard Test Method Plastics: Dynamics Mechanical Properties: In Flexure (Three-Point Bending)".

CHAPTER 4

MECHANICAL RELIABILITY OF EXTRUDED FILAMENTS

4 Mechanical Reliability of Extruded Filaments (Phase-I)

This chapter is concerned with the preparation and testing of extruded filament specimens with and without overlap, followed by Weibull statistical analysis of experimentally generated strength data for various extruded filament lengths. A probabilistic strength prediction model for different extruded filament lengths (5 cm, 10 cm and 15 cm) is presented, which takes into account the effects of extruded filament overlap.

4.1 Experimental Methodology

4.1.1 Preparation of specimens

In phase-I, specimens consisting of single extruded filaments (SEF), multiple extruded filaments (10 nos.) without overlap (MEFWNO) and multiple extruded filaments (10 nos.) with overlap (MEFWO) are printed in ULTIMAKER2+$^{(R)}$ (3D Printer) using spooled filament with an average diameter of 2.85 mm. A nozzle of diameter 0.4 mm printed the "extruded filaments" onto a hot bed, to create specimens of SEF, MEFWNO and MEFWO by fused deposition of Polylactic acid (PLA) as shown in Fig. 4.1 (a-c). Filaments are extruded as a raft on the bed which is in raft mode and printed using in g-code format from Cura software. The raft parameters are described in Table 4.1. The specimens are prepared by cutting from the longest filament that could be extruded on the bed. For fused filaments with overlap, the diameter is obtained from measurement of microscopic images using ImageJ software. For individual fused filaments without overlap, the diameter is measured at 5 locations using digital Vernier callipers.

Table 4.1: Extruded filament Raft parameters

Parameter	Ultimaker^{2+} PLA value for MEFWNO	Ultimaker^{2+} PLA value for MEFWO
Air gap (mm)	0.0	0.0
Extrusion width (mm)	0.35	0.35
Nozzle size (mm)	0.4	0.4
Filament color	White	White
Infill Density (%)	100	100
Printing Temperature (°C)	200	200
Build plate temperature (°C)	60	60
Print speed (mm/s)	50	50
Travel speed (mm/s)	120	120
PLA Spool Diameter (mm)	2.85	2.85
Raft base width (mm)	0.4	0.4
Raft base line width (mm)	0.4	0.4
Raft base line spacing (mm)	0.0	0.1

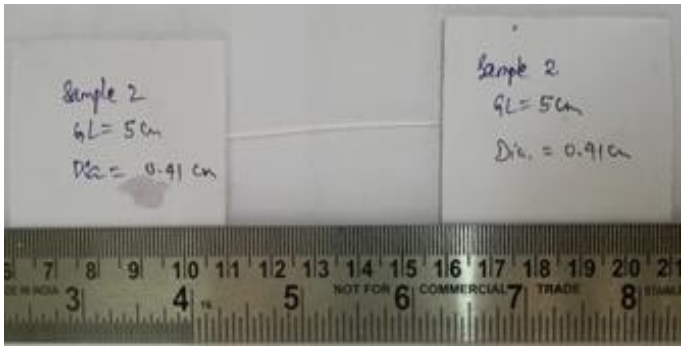

(a)

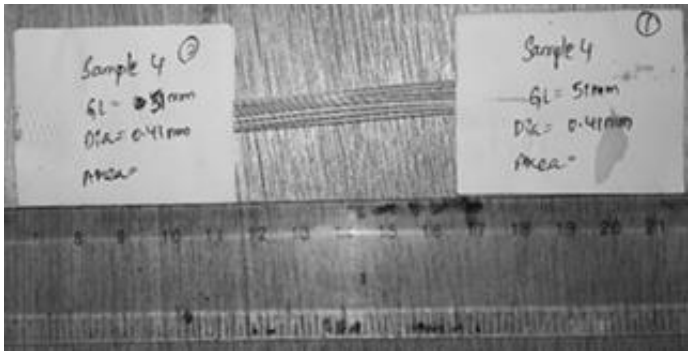

(b)

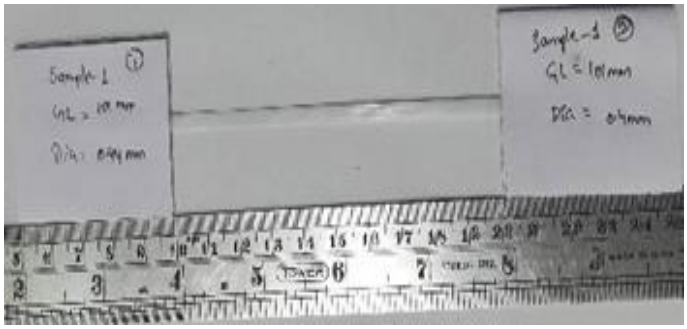

(c)

Figure 4.1: (a) SEF specimen (b) MEFWNO specimen and (c) MEFWO specimen.

The extruded filaments are observed to show variation in diameter (apart from several other defects) as shown in Fig.4.2, which may affect the mechanical characteristics of 3D printed components (Fig.4.3). The average surface roughness (Fig.4.5) Ra is the arithmetic mean of the absolute values of the profile deviations from the mean line and is by far the most commonly used parameter in surface finish measurement. Ra is 0.67µm for MEFWO (Fig.4.4). Mean peak to-valley height (Rz) can be calculated from the peak-to-valley values of five equal lengths (Ayrilmis 2018b).

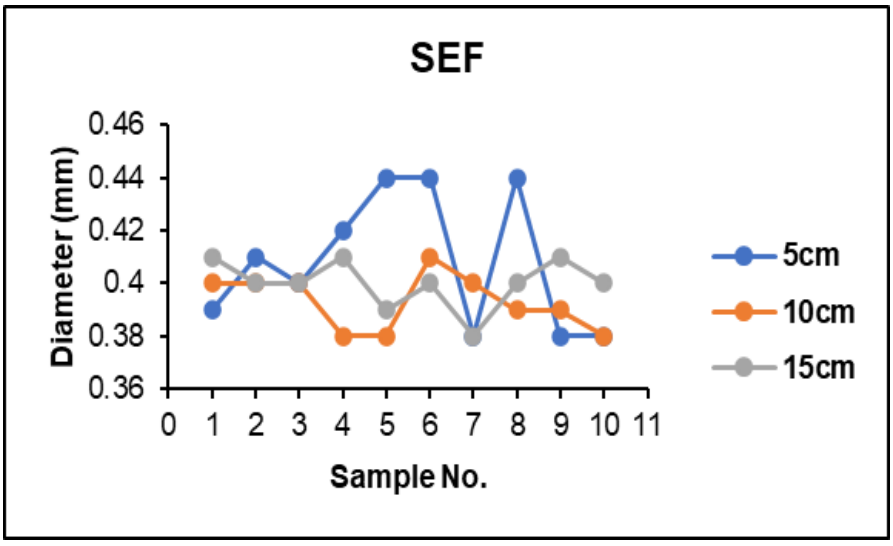

Figure 4.2: Diameter variation of SEF specimens.

Figure 4.3: Microscopic image of MEFWO with varying voids.

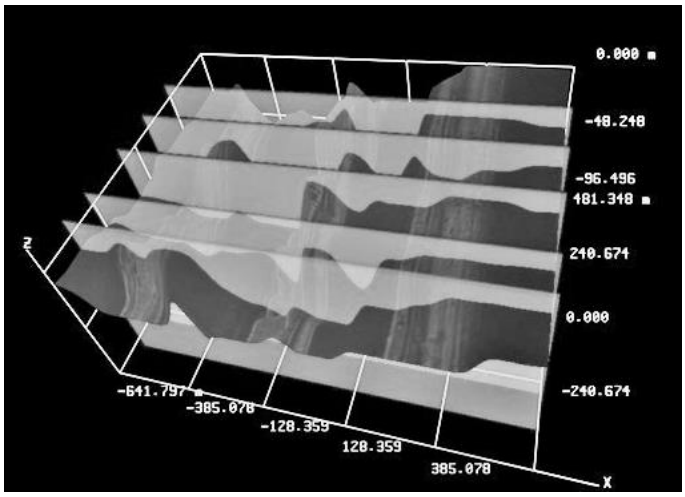

Figure 4.4: Surface Roughness for MEFWO.

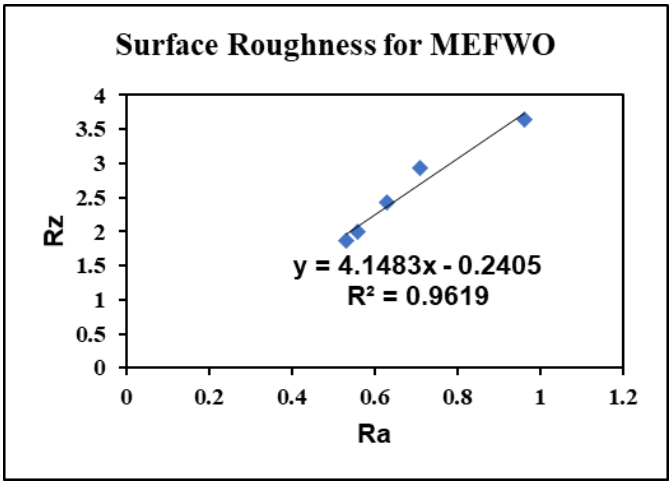

Figure 4.5: Graph of Surface roughnes for MEFWO.

4.1.2 Testing of specimens

Tensile testing of SEF, MEFWNO and MEFWO specimens is performed using a Universal Testing Machine (UTM) of capacity 100kN. All the specimens are tested at room temperature ($\pm 28^0$C) with a load cell of 5kN and displacement rate of 0.5mm/min until the failure of the specimen. Extruded filaments of three different overall lengths 15 cm, 20cm and 25 cm, (including the grip length of 5 cm on top and bottom for holding the extruded filaments in grips) are tested. Hence, the gauge length of the specimens are 5 cm, 10 cm and 15 cm respectively. The diameter of PLA extruded filaments is measured at five points along the length of each specimen using Digital Vernier Callipers/ Optical Microscope instruments. Paper tabs are attached to specimens as shown in Fig.4.6 in order to avoid failure at or within the grips according to ASTM D3379-75 procedure (Ilankeeran, Mohite, and Kamle 2012; "Standard Test Method for Tensile Strength and Young's Modulus for High-Modulus Single-Filament Materials 1," n.d.).

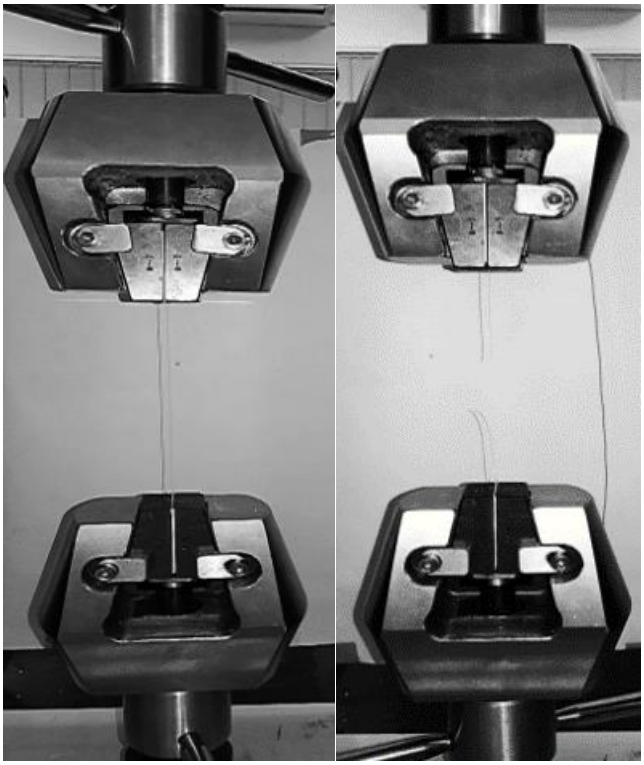

(a)

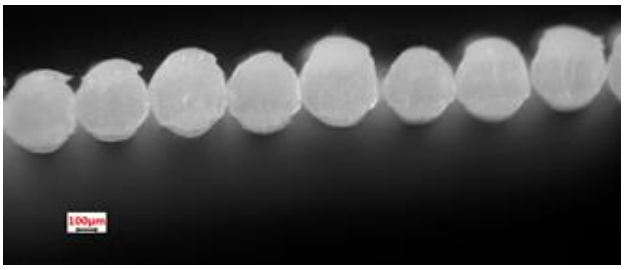

(b)

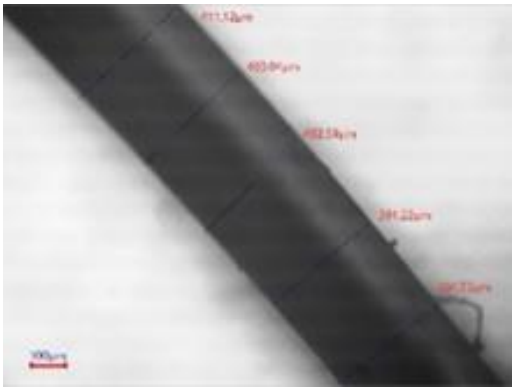

(c)

Figure 4.6: (a) SEF before and after testing, (b) Microscope image of C/S of MEFWO specimen and (c) Microscope image of C/S of SEF specimen.

4.2 Reliability analysis

The two-parameter Weibull distribution, typically used in fracture strength studies, is used for reliability analysis in this study. The distribution is given in Equation (4.1) below (Selmy, Azab, and El-Baky 2014a):

$$F(x;\eta,\beta) = 1 - \exp\left(-\left(\frac{x}{\eta}\right)^{\beta}\right) \qquad \textbf{(4.1)}$$

The determination of *x*-values, corresponding to a predefined failure probability enables estimation of reliability of structural and mechanical components. In the Weibull distribution, F (x; η, β), is the probability that the fracture strength is less than or equal to 'x'. From the expression: F (x; η, β) + R (x; η, β) = 1, reliability R (x; η, β), which is the probability that the fracture strength is *'x'* or greater than 'x', is given by:

$$R(x;\eta,\beta) = \exp\left(-\left(\frac{x}{\eta,}\right)^{\beta}\right) \qquad \textbf{(4.2)}$$

$$\eta \geq 0;\ \beta \geq 0$$

The scale parameter 'η' and shape parameter 'β' of Weibull distribution function F (x; η, β) can be obtained from the experiments. The methods usually employed in the estimation of these parameters are - linear regression, method of maximum likelihood, and method of moments (Du et al. 2012a). The commonly used linear regression enables parameter estimation in the present work.

4.2.1 Linear regression

A linear regression model in the form (Y = mX + c) is obtained by rearranging Eq. (4.2) into: 1- F (x; η, β) = exp $\left(-\left(\frac{x}{\eta,}\right)^{\beta}\right)$ and taking logarithms twice on both sides, as shown below:

$$\ln\left(ln\left[\frac{1}{1-\mathrm{F}\,(x;\,\eta,\beta)}\right]\right) = cln(x) - cln(\eta) \qquad \textbf{(4.3)}$$

F (x; η, β) is estimated from experimental strength values by arranging 'n' observations in ascending order of magnitude, where x_i denotes the i^{th} smallest observation (i=1 corresponds to the smallest and i= n corresponds to the largest). Then the median rank of x_i, which is a good estimator of F (x_i; η, β) is:

$$\hat{\mathrm{F}}(x_i;\eta,\beta) = \frac{\mathrm{i} - 0.3}{n + 0.4} \qquad \textbf{(4.4)}$$

The estimates for 'η' and 'β' are obtained by linear regression of (X, Y) $=\left(ln(x), ln\left(ln\left[\frac{1}{1-\mathrm{F}\,(x;\,\eta,\beta)}\right]\right)\right)$ for the model in Eq. (4.3). The curve generated by X_i and Y_i, is the Weibull Probability Plot (WPP) of the material. If the regression curve is a straight line, i.e., the correlation coefficient of X_i and Y_i is close to 1, the material strength distribution can be described using the two-parameter Weibull distribution (Joffe, Andersons, and Sparniņš 2009). The tensile strength and tensile failure strain (%) result obtained from the experiments are shown in Table 4.2 in next section.

In order to determine η and β, the values given in Table 4.3 and 4.4 are arranged in ascending order and (X, Y) values are computed. Then linear regression model between the (X, Y) values, are obtained for different specimens having lengths of (5 cm, 10 cm and 15 cm) respectively.

The slope of the line which gives shape parameter 'η' and value of 'β' is determined from the intersection point of the regression line and Y-axis, in $b = e^{-(\frac{Y}{\beta})}$.

Shape parameter (Weibull modulus) ‘β’, indicates the shape of the distribution. The value of shape parameter β < 1.0 implies a decreasing failure rate. Similarly, β = 0 indicates constant failure, and β > 1.0 implies an increasing failure rate. The scale parameter ‘η’, indicates the spread in the distribution of data as well as peak amplitude and is related to mean fracture stress (Barbero, Fernández-Sáez, and Navarro, n.d.).

4.3 Results and Discussion

4.3.1 Uniaxial tensile behavior

4.3.2 Uniaxial tensile response of SEF

The stress vs strain curves of uniaxial tensile test on 3D printed SEF, MEFWO and MEFWNO specimens of each length 5 cm, 10 cm and 15 cm are shown in Fig. 4.7 respectively.

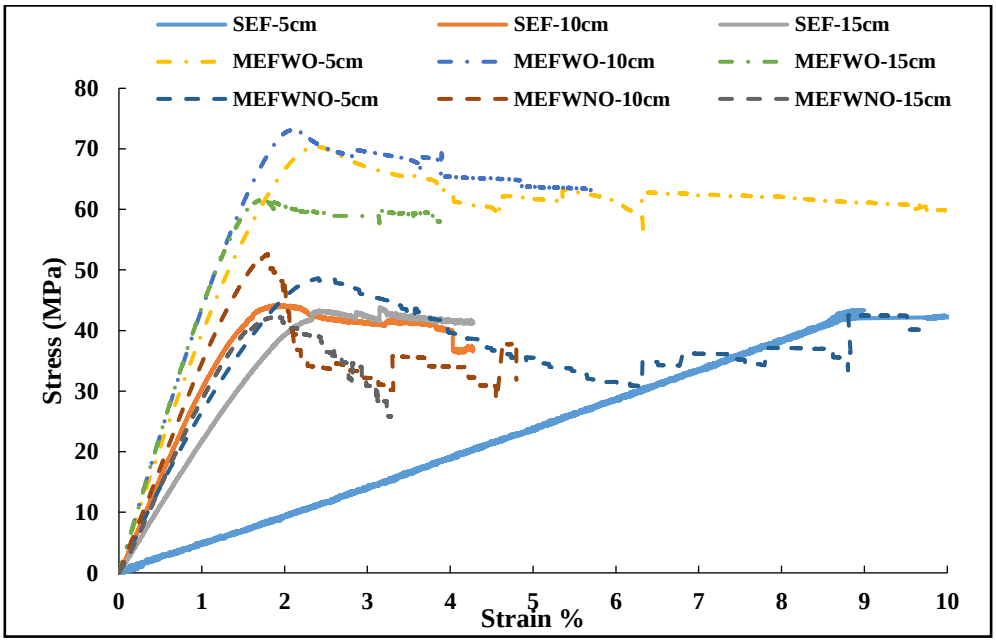

Figure 4.7: Stress vs Strain (avg.) for SEF, MEFWO and MEFWNO having 5 cm, 10 cm,15 cm gauge length.

As shown in Fig.4.7, it is observed from the uniaxial tensile tests that single strand specimens of 5 cm specimens demonstrate 3% and 4% higher strength than 10 cm and 15 cm specimens respectively. 5 cm specimens have additional strain at failure of 93% and 148% more than 10 cm and 15 cm specimens respectively. 5 cm specimens have additional toughness of 85% and 157% compared to 10 cm and 15 cm specimens

respectively. However, 15 cm specimens show greater increase in Young's Modulus of 13% and 4% when compared to 5 cm and 10 cm specimens respectively.

4.3.3 Uniaxial tensile response of MEFWNO

The stress vs strain curves of uniaxial tensile test on 3D printed MEFWNO specimens of length 5 cm, 10 cm and 15 cm are shown in Fig.4.7 respectively. The post-peak stress-strain curve for MEFWNO specimens is a stepped curve because extruded filaments fracture one by one due to global redistribution of stresses between the individual extruded filaments. In Fig.4.7, 10 cm long MEFWNO specimens have more tensile strength of 9% and 27%, which is more compared to 5 cm and 15 cm long specimens respectively. The 5 cm long specimens have more strain at a failure of 140% and 154% compared to 10 cm and 15 cm specimens respectively. 5 cm long specimens have better toughness of 160% and 207% compared to 10 cm and 15 cm specimens respectively. However, 10 cm specimens have better value of Young's modulus of 26% and 21% compared to 5 cm and 15 cm length of specimens respectively.

Table 4.2: Averaged load-displacement and stress-strain response of extruded filaments (SEF, MEFWNO & MEFWO) of 5 cm, 10 cm and 15 cm length.

Sample	Ultimate Load (N)	Displacement (mm)	Ultimate tensile Stress (MPa)	Strain @ UTS %	Stress @ failure (MPa)	Strain @ failure %	Toughness ($M.J.m^{-3}$)	Young's modulus, E (MPa)
SEF5 cm	5.93	2.87	44.77	1.90	33.00	5.93	1.85	2.95
SEF10 cm	5.28	3.09	43.53	1.81	39.84	3.08	1.00	3.19
SEF15 cm	5.42	3.64	43.00	1.56	39.56	2.39	0.72	3.32
MEFWNO 5 cm	60.59	3.85	49.60	2.44	25.73	7.73	2.76	2.80
MEFWNO 10 cm	57.53	3.13	54.12	1.81	30.75	3.23	1.06	3.53
MEFWNO 15 cm	52.28	4.60	42.74	1.84	27.20	3.05	0.90	2.92
MEFWO5 cm	64.37	3.62	70.74	2.42	57.65	7.16	3.41	3.79
MEFWO 10 cm	66.77	3.94	73.38	2.10	65.30	4.00	2.17	4.46
MEFWO 15 cm	56.12	4.35	61.80	1.91	56.70	3.11	1.50	4.07

Relatively greater variation is observed in the stress-strain curves of SEF specimens having 5 cm gauge length compared to SEF specimens of 10 cm and 15 cm gauge lengths. This can be attributed to several factors- i) variation of strand diameter along the length, ii) presence of defects within the volume of the extruded filament.

4.3.4 Uniaxial tensile response of MEFWO

The stress vs strain curves of uniaxial tensile test on 3D printed multiple extruded filaments with overlap (MEFWO) specimens of length 5 cm, 10 cm and 15 cm are shown in Fig.4.7 respectively. In Fig.4.7, it is observed from the uniaxial tensile test on MEFWO specimens that 10 cm long specimens have an additional tensile strength of 4% and 19% compared to 5 cm and 15 cm long MEFWO specimens respectively. The 5 cm specimens have greater strain at failure of 79% and 130% compared to 10 cm and 15 cm specimens respectively. The 5cm long specimens have additional toughness of 57% and 127% when compared to 10cm and 15 cm specimens respectively. However, 10 cm specimens show additional increase in Young's modulus of 18% and 10% when compared to 5 cm and 15 cm specimens respectively. In the case of MEFWO specimens, the post-peak stress-strain curve is smoother because of local to global stress redistribution which causes the extruded filaments to fail simultaneously once critical stress is achieved.

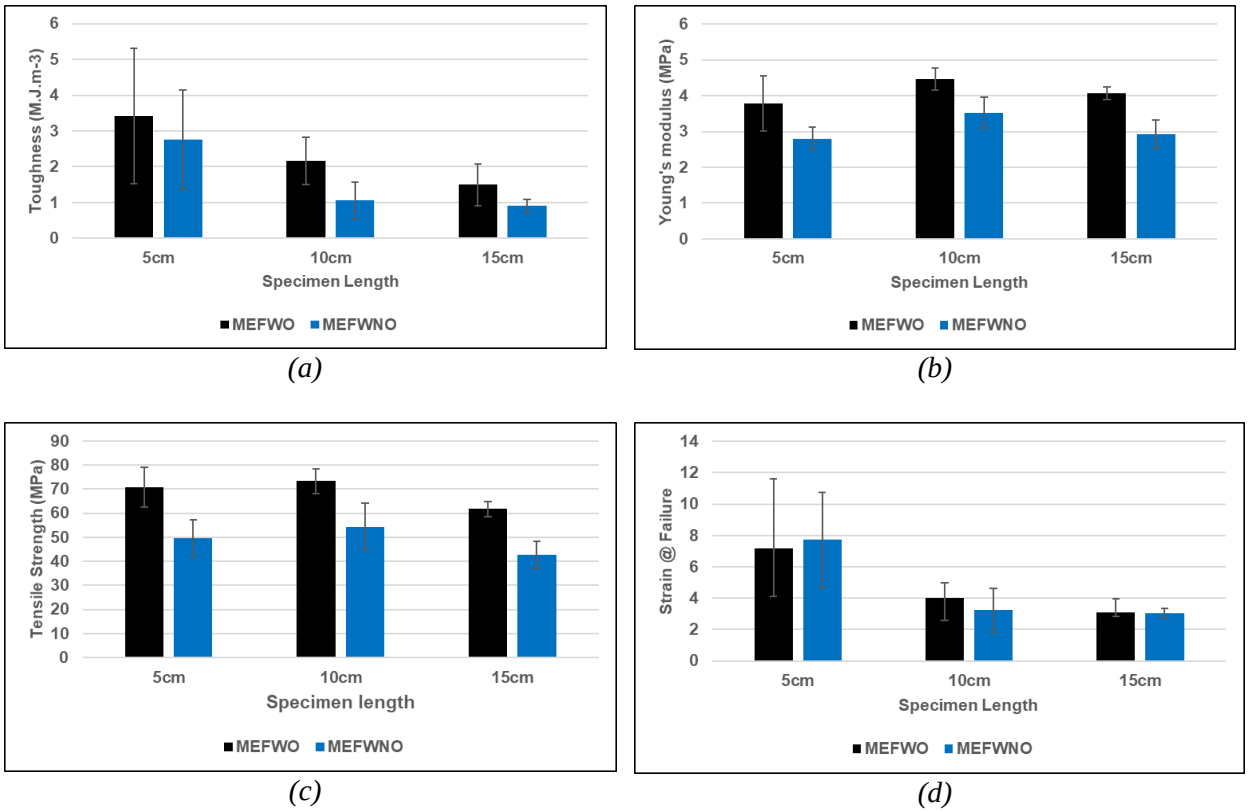

Figure 4.8: Comparison of mechanical properties of MEFWNO and MEFWO specimens (error bar shows the standard deviation).

The MEFWO specimens have more tensile strength than MEFWNO with an increase of 43%, 36% and 45% for 5 cm, 10 cm and 15 cm gauge length respectively, as shown in

Fig.4.8. The multiple extruded filaments (10 nos.) with overlap (MEFWO) specimens display more toughness than multiple extruded filaments (10 nos.) without overlap (MEFWNO) specimens with an increase of 24%, 105% and 67% for 5 cm, 10 cm and 15 cm gauge lengths respectively. MEFWO specimen has lower strain at failure at 5 cm of 8% compared with MEFWNO. For 10 cm and15 cm, MEFWO has more strain at failure than MEFWNO with an increase of 24% and 2% respectively. MEFWO specimens has higher Young's modulus than MEFWNO with an increase of 35%, 26% and 39% for 5 cm, 10 cm and 15 cm gauge length.

It is observed that the variation in diameter along the length significantly impacts the mechanical properties of extruded filaments and is the source of scatter in strengths. Although a parameter study on the effect of diameter of the fused extruded filament or layer thickness on mechanical characteristics is not conducted in this study, it is expected that there might exist an optimal diameter of fused filament, which would satisfy the conflicting criteria of low porosity and high strength vs economical amount of material.

4.4 Weibull Analysis

The trends of tensile strength and tensile failure strain for different specimens are shown in Figs. 4.9-4.13. The values of R^2, related equations, shape parameter (η) and scale parameter (β) of Weibull distribution function have been calculated for tensile strength (Figs. 4.9-4.11) and tensile failure strain (%) (Figs. 4.12 - 4.13) from linear regression equations and their values are listed in Tables 4.3 and 4.4 respectively.

The slope of the line for SEF specimens of 5 cm length in Fig.4.9 is 4.99 (i.e., β = 4.99) and b values are computed to be η = 48.71, using the point of line intersects the at Y-axis (-19.376) at $b = e^{-(\frac{Y}{\beta})}$. Therefore, β= 4.99 indicates that there is a higher probability that the material will fracture with every unit of increase in stress. The values of η and β obtained are listed in Table 4.3 and 4.4. The plot of R (x; η, β) is shown in Figs (4.15 and 4.16). Fig. (4.15) shows the reliability curve of tensile strength and Fig. (4.16) shows the reliability curve of tensile strain at failure for different specimens having different lengths.

The reliability curve for SEF specimens in Fig.4.15 shows that fracture strength values which are roughly less than or equal to 19 MPa, 25 MPa & 31 MPa (for 5 cm, 10 cm and 15 cm specimens respectively) provide high reliability (0.95). Here, a reliability

level of 0.95 is considered for analysis. When these values are substituted in R (x; η, β) in Eq (4.2) and solved for x, the fracture strengths of 26.8 MPa, 31.40 MPa and 34.61 MPa (for 5 cm, 10 cm, and 15 cm specimens respectively) are obtained. In other words, this material will fail with 0.95 probability for 26.8 MPa, 31.40 MPa and 34.61 MPa (for 5 cm, 10 cm and 15 cm specimens respectively) or more.

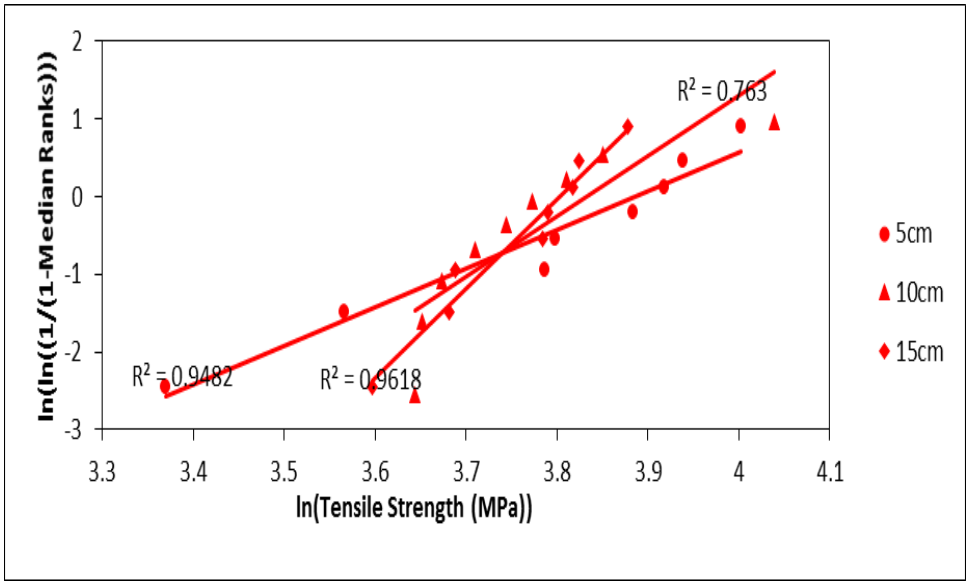

Figure 4.9: Tensile strength data for SEF specimens of different lengths 5 cm, 10 cm and 15 cm.

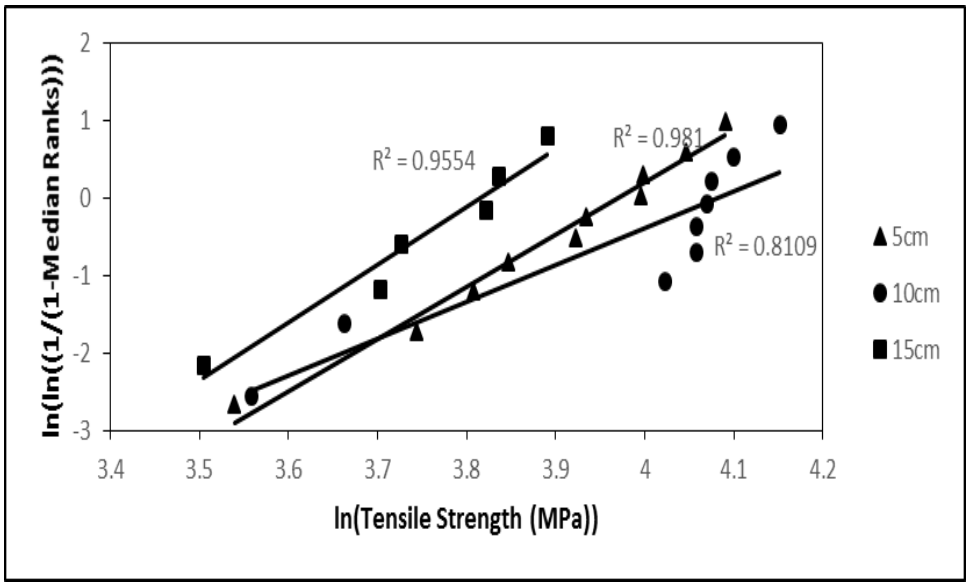

Figure 4.10: Tensile strength data for MEFWNO specimens of different lengths 5 cm, 10 cm and 15 cm.

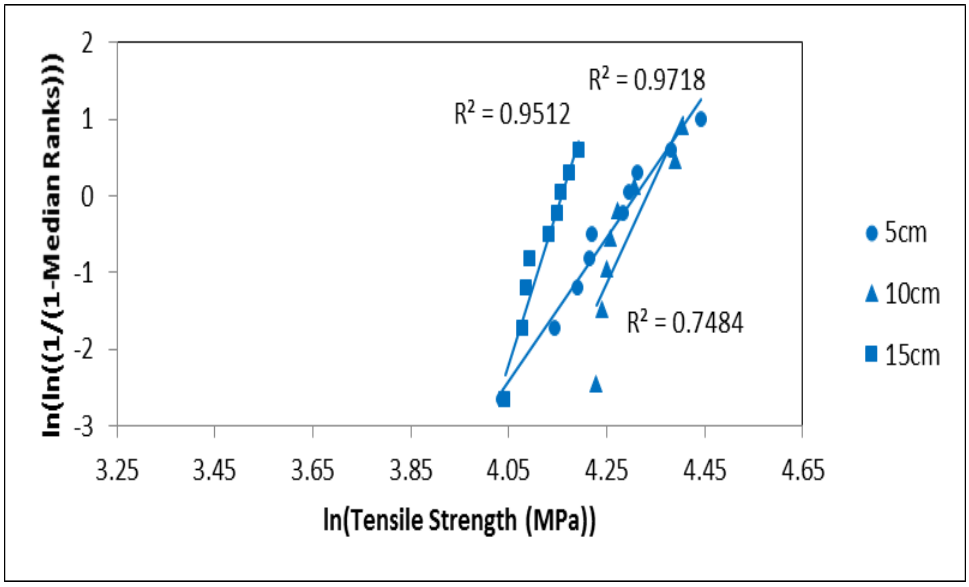

Figure 4.11: Tensile strength data for MEFWO specimens of different lengths 5 cm, 10 cm and 15 cm.

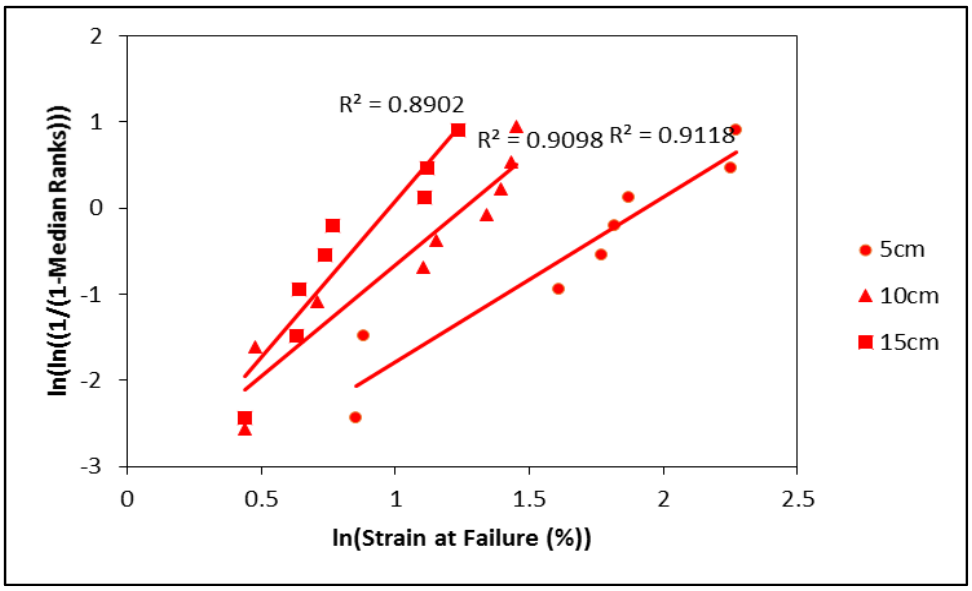

Figure 4.12: Tensile strain at failure (%) data for SEF specimens of different lengths 5 cm, 10 cm and 15 cm.

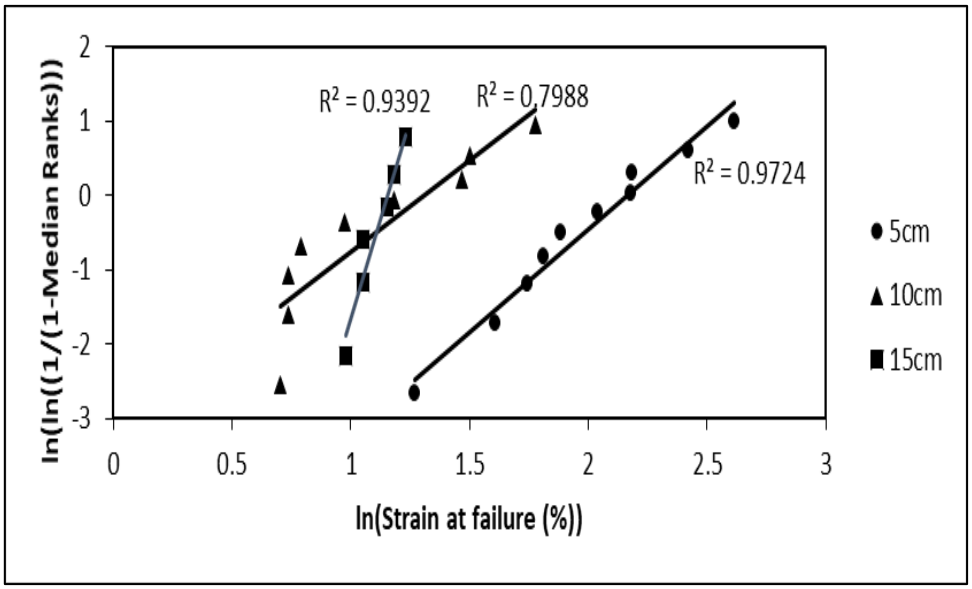

Figure 4.13: Tensile strain at failure (%) data for MEFWNO specimens of different lengths 5 cm, 10 cm and 15 cm.

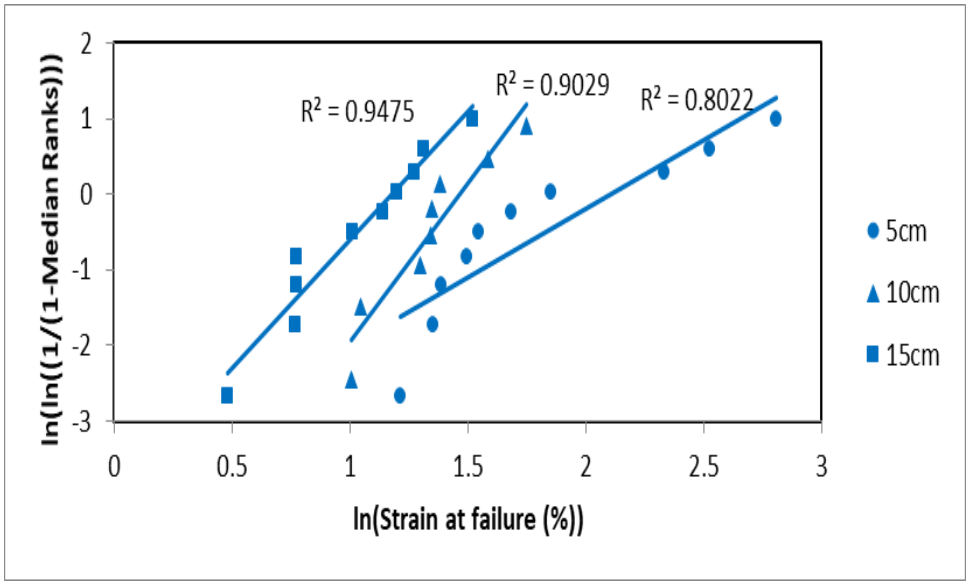

Figure 4.14: Tensile strain at failure (%) data for MEFWO specimens of different lengths 5 cm, 10 cm and 15 cm.

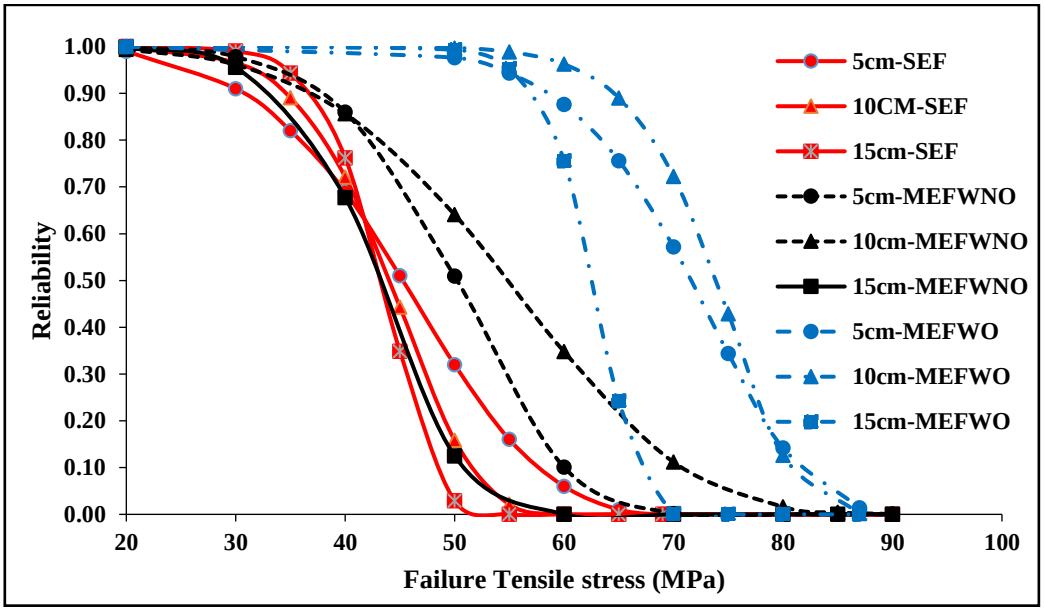

Figure 4.15: Reliability curve of Tensile Strength for SEF, MEFWNO & MEFWO Specimens having length 5 cm, 10 cm and 15 cm.

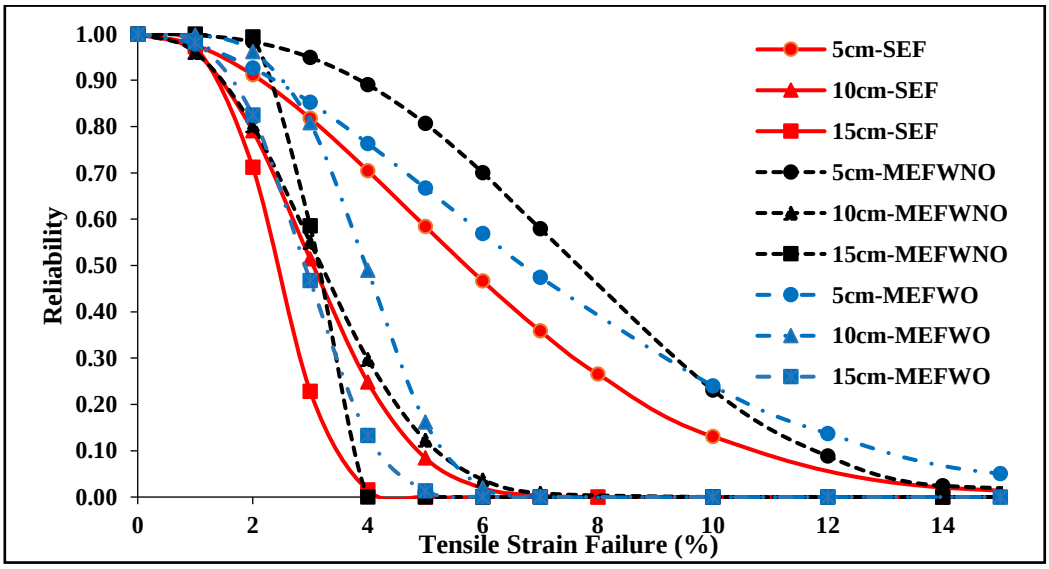

Figure 4.16: Reliability curve of Tensile Strain at failure (%) for SEF, MEFWNO & MEFWO Specimens having length 5 cm, 10 cm and 15 cm.

Table 4.3: Values of Weibull parameters of Tensile Strength.

Weibull Parameters	5 cm length	10 cm length	15 cm length
		SEF Specimens	
R^2	0.948	0.763	0.962
Related Equation	y = 4.9862x - 19.376	y = 7.7474x - 29.697	y = 11.515x - 43.781
Scale parameter 'η'	48.71	46.21	44.79
Shape Parameter 'β'	4.99	7.75	11.52
		MEFWNO Specimens	
R^2	0.981	0.811	0.955
Related Equation	y= 6.7112x - 26.646	y = 4.7378x - 19.343	y = 7.5004x - 28.608
Scale parameter 'η'	53.00	59.31	45.35
Shape Parameter 'β'	6.71	4.74	7.50
		MEFWO Specimens	
R^2	0.97	0.75	0.95
Related Equation	y = 9.3638x – 40.346	y = 13.87x – 60.05	y = 20.23x – 84.1
Scale parameter 'η'	74.48	75.91	63.89
Shape Parameter 'β'	9.36	13.87	20.23

Table 4.4: Values of Weibull parameters of Strain at Failure.

Weibull Parameters	5 cm length	10 cm length	15 cm length
		SEF Specimens	
R^2	0.912	0.91	0.890
Related Equation	y = 1.9211x - 3.7134	y = 2.5713x - 3.2332	y = 3.6255x - 3.5394
Scale parameter 'η'	6.91	3.52	2.69
Shape Parameter 'β'	1.92	2.57	3.63
		MEFWNO Specimens	
R^2	0.972	0.80	0.9392
Related Equation	y = 2.7681x – 5.9926	y = 2.4563 – 3.2134	y = 10.794x – 12.484
Scale parameter 'η'	8.17	3.70	10.79
Shape Parameter 'β'	2.77	2.46	3.18
		MEFWO Specimens	
R^2	0.802	0.903	0.948
Related Equation	y = 1.8169x - 3.8292	y = 4.1984x - 6.1577	y = 3.3857x - 3.9926
Scale parameter 'η'	8.23	4.33	3.25
Shape Parameter 'β'	1.82	4.20	3.39

Conversely, let R (x; η, β) =0.368, then, consider SEF specimens of 5 cm length (Fig.4.15) and let $x=\eta$, therefore R (48.71; 48.71, 4.99) = exp $\left(-\left(\frac{x}{\eta}\right)^{c}\right)$= 0.368, that is 36.8% of the tested specimens have a fracture strength of at least 48.71 MPa. For specimen with a length of 10 cm (η=46.21 and β=7.75), let $x=\eta$, therefore R (46.21; 46.21, 7.75) = 0.37, that is 37% of the specimens are estimated to show a fracture strength of equal to or greater than 46.21 MPa.

4.5 Conclusions

The tensile tests of 3D printed PLA extruded single extruded filaments (SEF), Multiple extruded filaments with no overlap (MEFWNO) and Multiple extruded filaments with overlap (MEFWO) are conducted to obtain Young's modulus, ultimate strength, strain at failure and toughness for various gauge lengths. Reliability analysis for tensile failure is conducted while considering the effect of different lengths of deposited PLA filaments as well as the effect of overlap of extruded filaments.

Characteristics such as failure strength and strain to failure are governed by the number of defects per unit volume of the material: hence the observed size effect observed at higher volume (length) specimens having, in general, lower predicted strength and strain at failure; which is consistent with Weibull statistical fracture theory. It is observed that overlapping of the extruded filaments typically results in higher strain at failure, higher toughness and higher Young's modulus compared to non-overlapped extruded filaments of the same length.

It is assumed that during tensile loading of MEFWO specimens, the overlap zones act in a manner similar to the matrix in a fibre reinforced composite, wherein a shear transfer mechanism occurs in which a high shear stress is generated in the overlap region around any fracture (in a filament).This enables bridging of stress over the discontinuity, leading to local stress re-distribution, until the shear stress exceeds the capacity of the overlap zone and global stress redistribution between overlapped extruded filaments occurs, until eventual global failure. Hence, the post-peak stress-strain curve is smoother because of a transition from local to global stress redistribution mechanism, which causes all the extruded filaments to achieve similar stresses and fail almost simultaneously once critical stress is achieved. In the case of MEFWNO specimens, there cannot exist a similar local stress redistribution mechanism. The extruded filaments fracture one by one due to

global redistribution of stresses between the individual extruded filaments, which leads to post peak softening prior to failure compared with SEF.

Weibull analysis presented in this study enables determination of probabilistic values of ultimate strength of fused deposited extruded filaments, as well as reliability indices to enable further high-fidelity FEA modelling towards determination of micro-mechanics based constitutive relationship for 3D printed polymer materials.

CHAPTER 5

ANALYTICAL MODELING OF STRENGTH

5 Analytical modeling of strength (Phase – II)

The material strength and modulus properties are modelled using reduction factors derived from mechanics of materials-based analysis, which take into account the effect of porosity as well as overlap between adjacent strands, on the strength and modulus of the material.

5.1 Analytical prediction of Strength and Stiffness of 0º & 90º tension specimens

FDM 3D printers form layers by depositing lines of PLA. This process means that layers are not bonded together as strongly as the strands (filament extrusion) themselves; there are voids between the strands and it's possible that layers may not fully adhere to one another (there are air gaps between strands). 'Air Gap' is defined as the distance between adjacent extruded fibres. For example, if adjacent fibres of width 0.4 mm are deposited with 0.36 mm axis to axis distance, the air gap is -0.04 mm is present (i.e., overlapping of 0.04 mm). Setting a negative air gap (overlapping) in this manner will increase the transverse and intralaminar shear strength of the printed part, as air gap directly alters the bond area between adjacent fibres.

As seen in Fig.5.1, the bond area gives an effective cross-sectional area for transverse loading. As all transverse load must be transferred through the bond area, this region is the 'weakest link' for transverse loading. Mechanical performance under these loading modes is therefore directly dependent on the overlapping length. Fig.5.2 shows the decrease in transverse bond area with decreasing overlapping length.

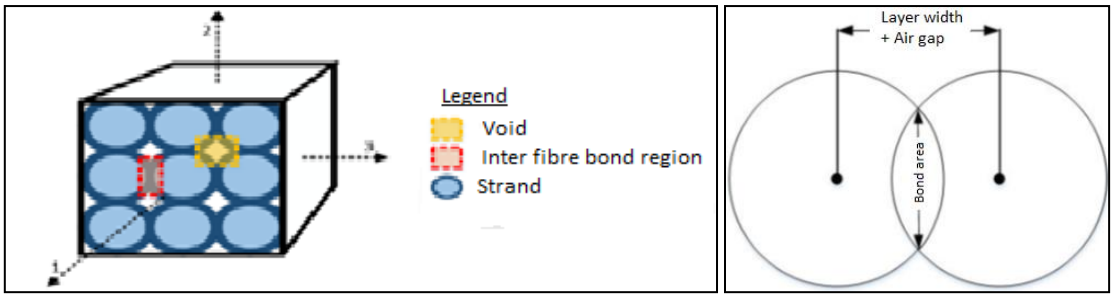

Figure 5.1: Showing void region and overlapping between strands

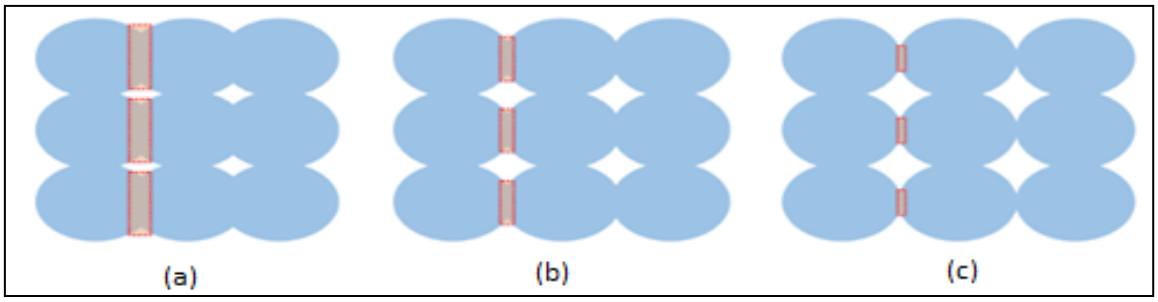

Figure 5.2: Illustration of the change in bond area (shown by red areas) with decreasing overlapping length as shown from (a) to (c) (Ziemian, Sharma, and Ziemian, n.d.)

3D printed prismatic specimens are cut at the middle sections to observe the shape, size and spacing between the strands in printed tensile specimen part. Once the part is cut, sandpaper is used to rub the particles deposited during cutting and then the specimen is observed under optical microscope. It is observed that the tension specimens consisted of elliptical sections (Fig.5.3) when a portion of the specimen is observed under optical microscope, and this due to compression of layers during 3D printing.

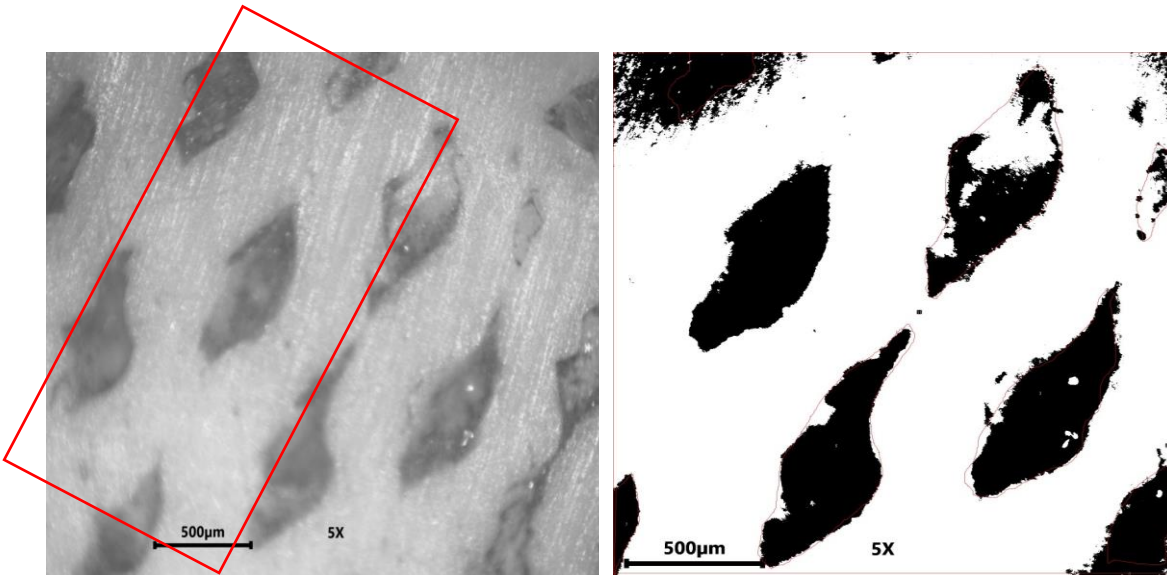

Figure 5.3: Cross section of 3D printed part observed under optical microscope (left) and binary form of it in ImageJ analyzer (right).

Hence for studying the effect of different overlapping lengths on the strength of 3D printed specimens, elliptical shaped of strands is used. Porosity parameter is used to study the variation of strength with the overlapping length. **Porosity** or **void fraction** is a measure of the void (i.e., “empty") spaces in a material, and is a fraction of the volume of voids over the total volume. It ranges between 0 and 1, or as a percentage between 0 and 100%. Strictly speaking, some tests measure the "accessible void", i.e., the total

amount of void space accessible from the surface. There are many ways to test porosity in a substance or part, such as industrial CT scanning, optical microscopy etc. In our study an optical method (i.e., determining the area of the material versus the area of the pores visible under the microscope) is considered to evaluate the amount of porosity. The "areal" and "volumetric" porosities are equal for porous media with random structure according to ("Copyright_1992_Porous-Media," n.d.).

The image obtained from optical microscope is then loaded into 'Image J' analysis software. Image obtained from optical microscopy is converted to binary form, in which black pixels correspond to air voids and white pixels correspond to PLA strands (Fig.5.3 (right)). An 'ImageJ measure' is then taken of a representative sample of voids, which counts the black pixels to find the total void area. This void area divided by the sample area gives the void density or porosity. As the 3D printed material has a regular pore distribution per unit thickness (Fig.5.3), this value is assumed to be approximately the same as volumetric porosity. In the case of 90^o specimens consisting of two layers, the porosity is extracted from two layers in the prismatic specimen.

Area of voids $= 4.10 \times 10^5 \mu m^3$

Area of Surface $= 2.49 \times 10^6$ µm3

Hence porosity $= \frac{Area\ of\ voids}{Total\ Area} = 0.164$

In this study the porosity in both 0^o and 90^o material specimens is assumed to be 0.164.

5.1.1 Without Overlapping

Consider a volume element of unit length as shown in Fig.5.4 (b). Let a and b be the dimensions of elliptical strands. In this study, rectangular configuration of strands is used in deriving the equation of porosity and during actual 3D printing, strands are laid in this type of configuration. The values of a and b is assumed to be such that the ratio of (a/b) equals 0.6. The deviation of strand cross section from circular to elliptical occurs due to the compression of layers during 3D printing (Fig.5.4 (a)). Since the printer from which specimens are printed has a nozzle of dia. 0.4mm (which is taken as 'a'), the value of 'b' obtained to maintain the ratio is 0.67.

Area of rectangle (A) $= 4a \times 4b$

Area of Strands $= 4\pi ab$

Hence, Area of voids (A_v) = 4ab (4-π)

Porosity = $\frac{V_v}{V} = \frac{4ab\,(4-\pi)}{16ab} = 0.2145$

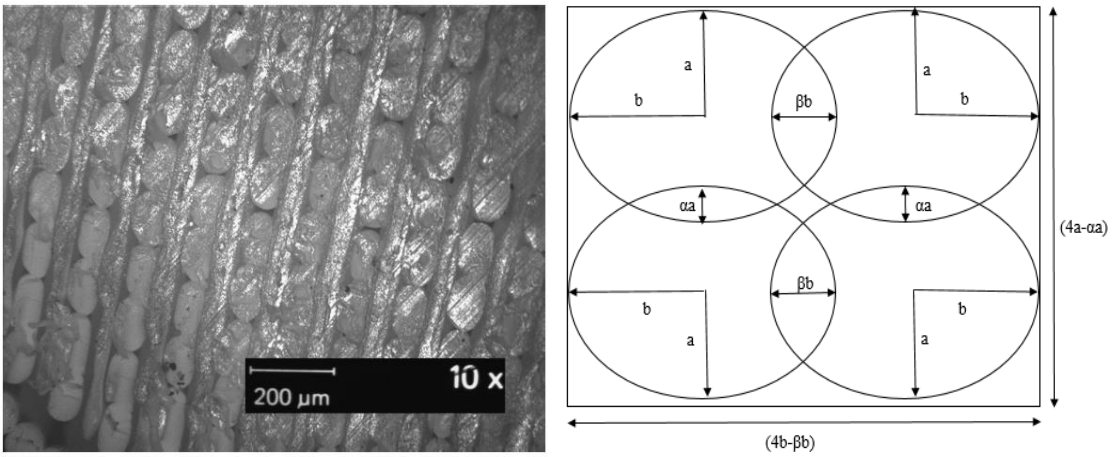

(a) (b)

Figure 5.4: (a) Deviation of strand cross section from circular to elliptical due to compression during printing (Butadiene Styrene 2007) ***(b) Volume element of unit length with horizontal & vertical overlapping***

5.1.2 With Overlapping

In Fig.5.4 (b), let a and b be the dimensions of each strand and 'αa'& 'βb' (α & β are vertical and horizontal overlapping coefficients) be the overlapping length in vertical & horizontal direction respectively.

Area of rectangle (A) = (4a- αa) x (4b-βb)

Area of Strands = 4πab

Hence, Area of voids (A_v) = ab [(4-α) (4-β)-4π)]

Porosity = $\frac{A_v}{A} = \frac{[(4-\alpha)(4-\beta)]-4\pi}{(4-\alpha)\ (4-\beta)}$ (5.1)

For different combinations of α & β, values of porosity is presented in Table 5.1.

Table 5.1: Values of porosity for different overlapping coefficient α & β.

β \ α	0	0.1	0.2	0.3	0.4	0.45
0	0.215	0.194	0.173	0.151	0.127	0.115
0.1	0.194	0.174	0.152	0.129	0.105	0.092

0.2	0.173	0.152	0.130	0.106	0.081	0.068
0.3	0.151	0.129	0.106	0.082	0.057	0.043
0.4	0.127	0.105	0.081	0.057	0.030	0.017
0.45	0.115	0.092	0.068	0.043	0.017	0.003

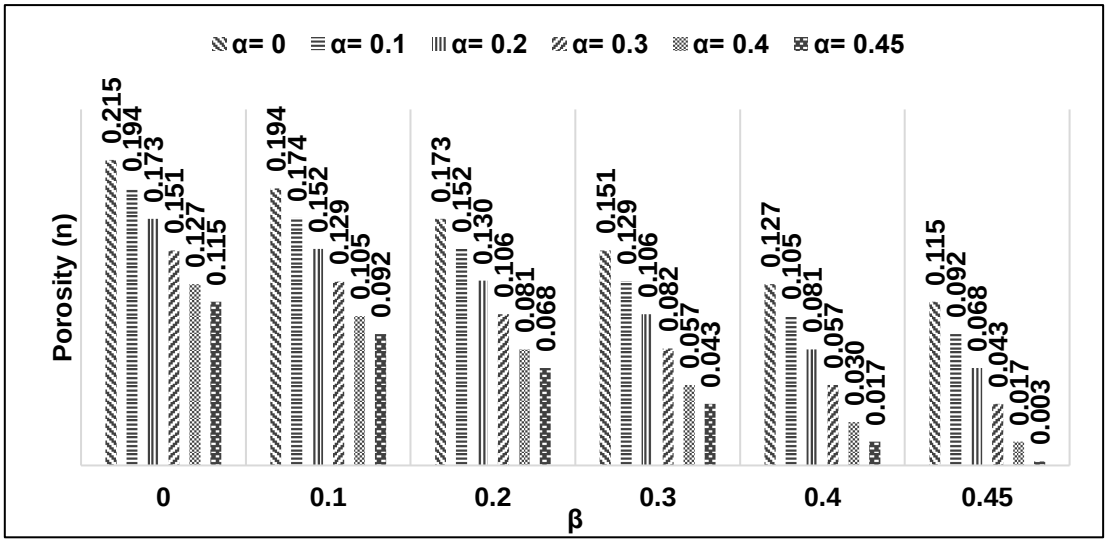

Figure 5.5: Variation in porosity due to both vertical and horizontal overlap

In this study only horizontal overlap is presented (Fig.5.6), due to limitations during comparison with TexGen software, which allows only horizontal overlapping. Fig.5.7 shows the variation of porosity as a function of horizontal overlapping coefficient (β) for (α=0).

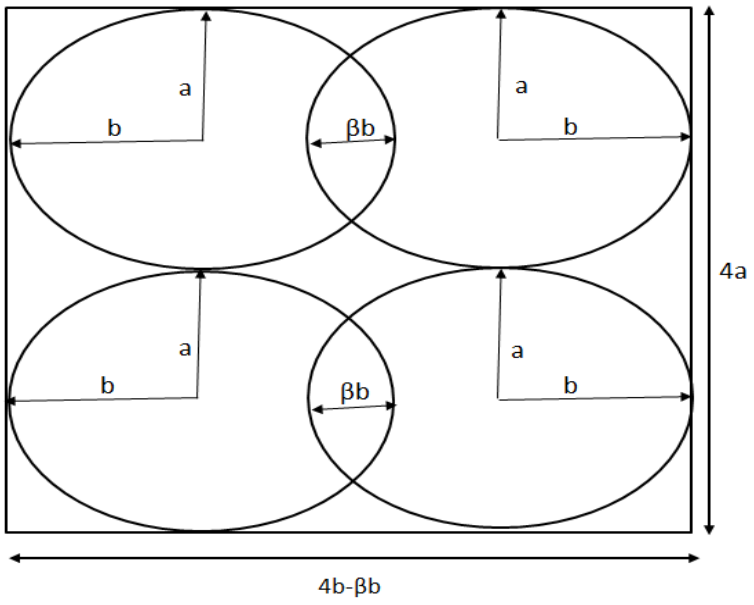

Figure 5.6: Volume element of unit length with horizontal overlapping only

Table 5.2: Values of Porosity for different vertical overlap coefficient (α=0) and different horizontal overlapping coefficient (β)

a (mm)	b (mm)	a/b	β	Vol. of strands (mm^3)	Total vol. of voids (mm^3)	Volume of rectangle (mm^3)	Porosity
0.4	0.67	0.60	0	3.351	0.916	4.267	0.215
0.4	0.67	0.60	0.1	3.351	0.809	4.160	0.194
0.4	0.67	0.60	0.2	3.351	0.702	4.054	0.173
0.4	0.67	0.60	0.3	3.351	0.596	3.947	0.151
0.4	0.67	0.60	0.4	3.351	0.489	3.840	0.127
0.4	0.67	0.60	0.45	3.351	0.436	3.787	0.115
0.4	0.67	0.60	0.6	3.351	0.276	3.627	0.076
0.4	0.67	0.60	0.67	3.351	0.201	3.552	0.057

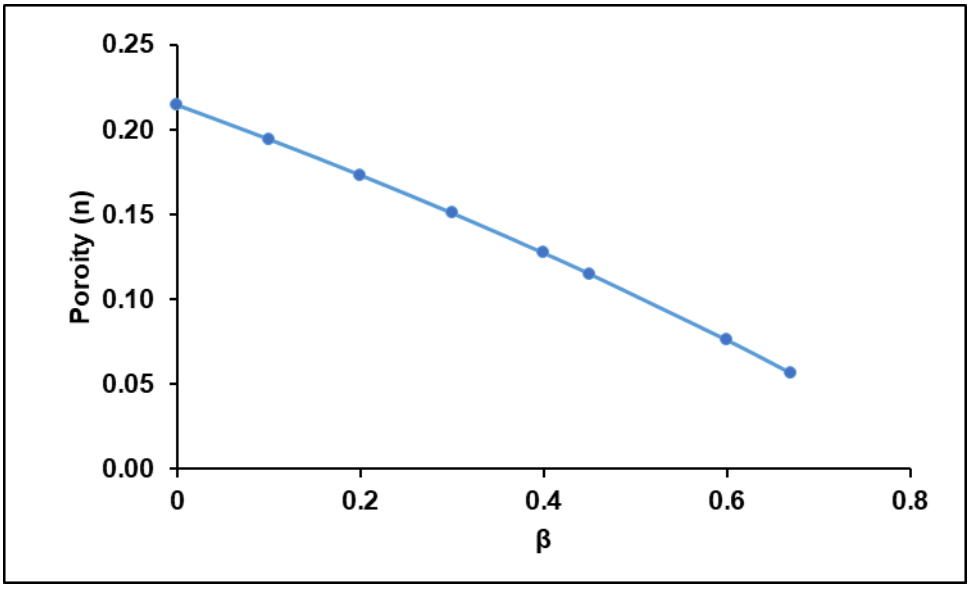

Figure 5.7: Analytical prediction of variation of porosity with respect to horizontal overlapping coefficient (β)

5.2 Strength Models proposed by different Researchers

Various researchers have studied the effect of porosity on the tensile strength (Ryshkewitch, n.d.; Li Li and Aubertin 2003). Equations proposed by them relating

strength and porosity are presented below and are compared with the experimental strength vs porosity values. It is assumed that the 3D printed 0^o and 90^o tension specimens have the same porosity of 0.164. The experimental strength ratio of 3D printed 0^o and 90^o tension specimen are 0.46 & 0.10 respectively compared to solid injection moulded specimens.

5.2.1 Power Law Equation

One of the first expressions proposed to measure σ_{un} dependency is due to Bal'shin (1949), who used the following power law for determining uniaxial tensile strength:

$$\boldsymbol{\sigma_{tn} = \sigma_{to}(1-n)^m} \qquad \textit{(5.2)}$$

Where, 'σ_{tn}' is the uniaxial tensile strength of the material with a porosity 'n', 'σ_{to}' is a parameter representing the (calculated) strength of a similar nonporous material (i.e., for n=0), and 'm' is an empirical constant. The value of 'm' is found to be between 3 (metals) to 6 (ceramics). In the present work, σ_{to} = 64.835 MPa, m = 4 for 0^o and 9 for 90^o 3D printed tension specimen.

Table 5.3:Ratio of σ_{tn}/σ_{to} according to Power Law Equation

n	**(σ_{tn}/σ_{to}) Ratio for 0^o tension specimen**	**(σ_{tn}/σ_{to}) Ratio for 90^o tension specimen**
0	1.00	1
0.057	0.79	0.59
0.076	0.73	0.49
0.115	0.61	0.33
0.127	0.58	0.29
0.151	0.52	0.23
0.173	0.47	0.18
0.194	0.42	0.14
0.215	0.38	0.11

5.2.2 Ryshkewitch and Duckworth Equation (1953)

Instead of using power law equation for representing the nonlinearity of σ_{u-n} relationship, an exponential function is employed (Ryshkewitch, n.d.). The basic equation, as a result of the work of Ryshkewitch et.al., (1953), can be written as:

$$\sigma_{un} = \sigma_{uo} e^{-bn} \quad (5.3)$$

Where, 'σ_{uo}' is the (calculated) strength of non-porous material (i.e., n = 0) and 'b' is an empirical constant whose value ranges from 3 to 7. The formula is applicable for both compression and tension. In the present work, strength vs porosity for tensile tests is necessary hence, ($\sigma_{uo} = \sigma_{to}$ and $\sigma_{un} = \sigma_{tn}$). In present work, σ_{to} = 64.835 MPa, b = 4.5 for 0^o and 10 for 90^o 3D printed tension specimen are used.

Table 5.4:Ratio of σ_{tn}/σ_{to} as per Ryshkewitch and Duckworth Equation (1953)

Porosity (n)	**(σ_{tn}/σ_{to}) Ratio for 0^o tension specimen**	**(σ_{tn}/σ_{to}) Ratio for 90^o tension specimen**
0	1.00	1.00
0.057	0.77	0.57
0.076	0.71	0.47
0.115	0.60	0.32
0.127	0.56	0.28
0.151	0.51	0.22
0.173	0.46	0.18
0.194	0.42	0.14
0.215	0.38	0.12

5.2.3 Li Li and Michel Aubertin Equation

Li Li et.al., (Li Li and Aubertin 2003) proposed an equation for determining the relation between tensile strength and porosity which incorporates a generalized form of power law and Ryshkewitch et.al., (1953) law in it. The following equation is proposed by the author:

$$\boldsymbol{\sigma_{tn} = \sigma_{to}\left(1 - sin\left(\frac{\pi}{2}\frac{n}{n_{ct}}\right)^{x_1}\right)} \quad (5.4)$$

Where, 'σ_{tn}' is the uniaxial tensile strength of the material with a porosity 'n' and 'n_{ct}' is critical porosity (max. porosity). In present work, σ_{to} = 64.835 MPa, x = 4 for 0^o and 1.5 for 90^o 3D printed tension specimen are used.

Table 5.5: Ratio of σ_{tn}/σ_{to} as per Li Li and Michel Aubertin Equation

Porosity (n)	n/n_{ct}	$(\sigma_{tn}/\sigma_{to})$ Ratio for 0° tension specimen	$(\sigma_{tn}/\sigma_{to})$ Ratio for 90° tension specimen
0	0.00	1.00	1.00
0.057	0.27	0.97	0.74
0.076	0.35	0.92	0.62
0.115	0.53	0.69	0.36
0.127	0.59	0.59	0.28
0.151	0.70	0.37	0.16
0.173	0.80	0.17	0.07
0.194	0.90	0.05	0.02
0.215	1.00	0.00	0.00

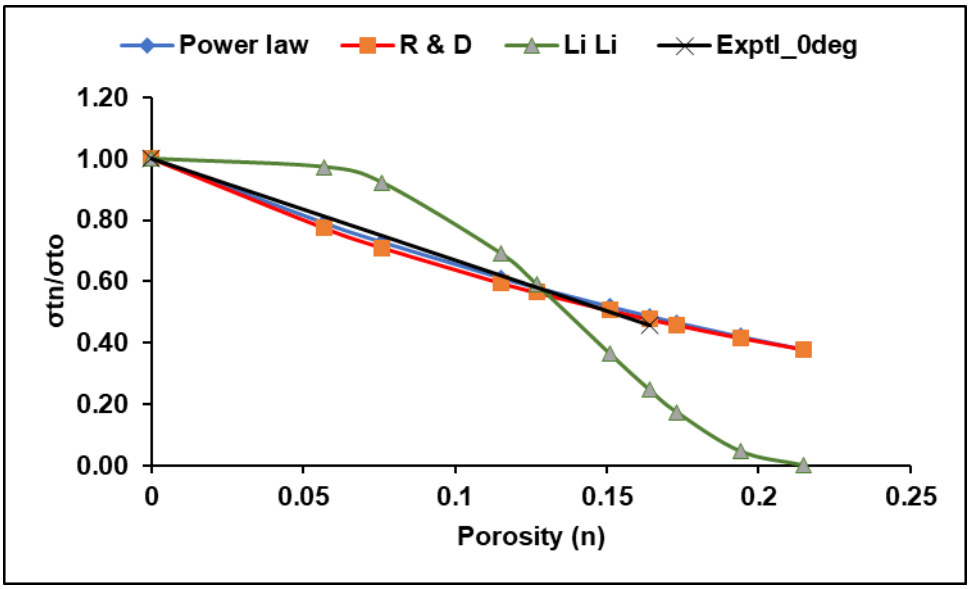

(a)

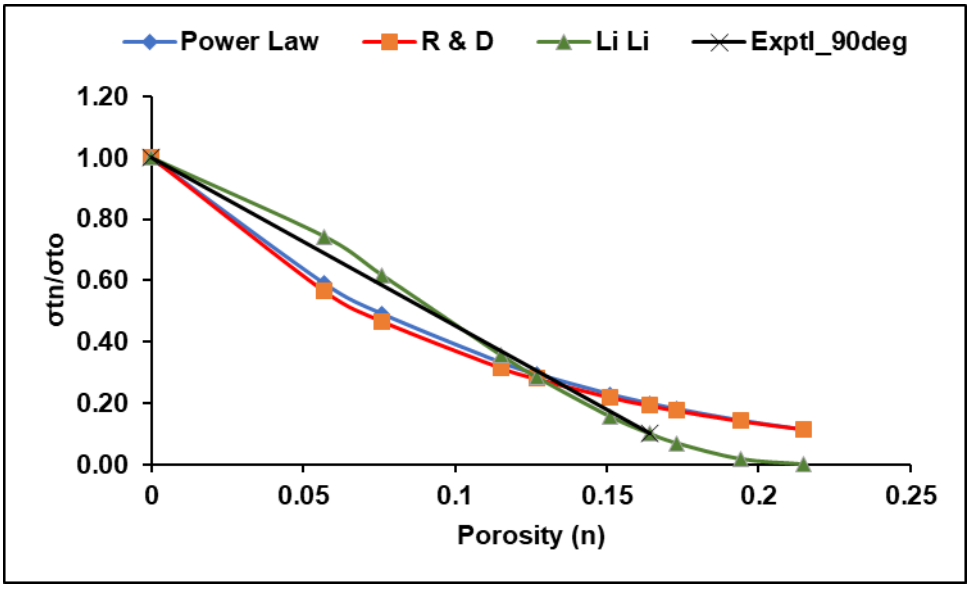

(b)

Figure 5.8: Comparison of experimental strength ratio [(a) for 0º& (b) for 90º] with analytical porosity-based equations

Observations:

The following observations emerge from the above graphs:

- For 0º tension specimen (Fig. 5.8 (a)), the Power law equation with empirical constant m=4, and Ryshkewitch and Duckworth (1953) equation with empirical constant b=4.5 predict well in comparison with experimental values. However the equation developed by Li Li and Michel Aubertin (2003) with x=4, over predicts the strength for a certain range and then suddenly under predicts the strength vs porosity values for other ranges.
- For 90º tension specimen (Fig. 5.8 (b)), the Power law equation with empirical constant m=9, Ryshkewitch and Duckworth (1953) equation with empirical constant b=10 as well as Li Li and Michel Aubertin with x=1.5, provide good agreement with experimental values.

5.3 Stiffness Models proposed by different Researchers

It is interesting to compare the experimental results with predictions of various micromechanical schemes for a porosity of 0.164. For this, we use(Cramer and Sevostianov 2009) non-interaction approximation, differential scheme and Mori-Tanaka scheme. According to these schemes, effective Young's modulus is expressed as follows:

a) Rule of Mixture: To use this rule, matrix is considered to be composed of air voids while strands are considered as fibers.

$$E = E_f V_f + E_m V_m \quad (5.4)$$

Where, 'E_f' is taken as modulus of solid specimen (2290.8 MPa [30]) and 'E_m' is taken as modulus of air (0 MPa). 'V_f' denotes volume fraction of fibres w.r.t solid specimen and 'V_m' is volume fraction of air voids. For different values of 'β' V_f & V_m are calculated and accordingly the value of 'E'. Then the ratio of calculated 'E' to 'E_o' ('E' of solid specimens) is compared with different porosity based elastic modulus equations mentioned below.

b) Non-interaction approximation:

$$E^* = \frac{E_0}{1 + 3p} \quad \textbf{(5.5)}$$

c) Differential scheme:

$$E^* = E_0(1 - p)^3 \quad \textbf{(5.6)}$$

d) Mori-Tanaka scheme:

$$E^* = \frac{E_0(1 - p)}{1 + 2p} \quad \textbf{(5.7)}$$

Where, E_0 = Elastic modulus for solid material, p = Porosity & E*= Elastic modulus for porous material. The value of E_o = 2290.8 MPa (Kumar et al. 2017) is used and 'E*' are calculated for different porosity values as shown in Table 5.6.

Table 5.6: Ratio of (E^*/E_o) obtained from different formulas (Cramer and Sevostianov 2009)

Porosity (n)	**E/E_o for (Rule of mixture)**	**E^*/E_o for (Non-interaction approximation)**	**E^*/E_o for (Differential scheme)**	**E^*/E_o for (Mori–Tanaka scheme)**	**E^*/E_o for (Particulate Dispersion)**
0.215	0.79	0.61	0.48	0.55	0.96
0.194	0.81	0.63	0.52	0.58	0.97
0.173	0.83	0.66	0.57	0.61	0.97
0.151	0.85	0.69	0.61	0.65	0.98
0.127	0.87	0.72	0.66	0.70	0.99
0.115	0.88	0.74	0.69	0.72	0.99
0.076	0.92	0.81	0.79	0.80	0.99
0.057	0.94	0.90	0.84	0.85	0.99
0	1.00	1.00	1.00	1.00	1.00

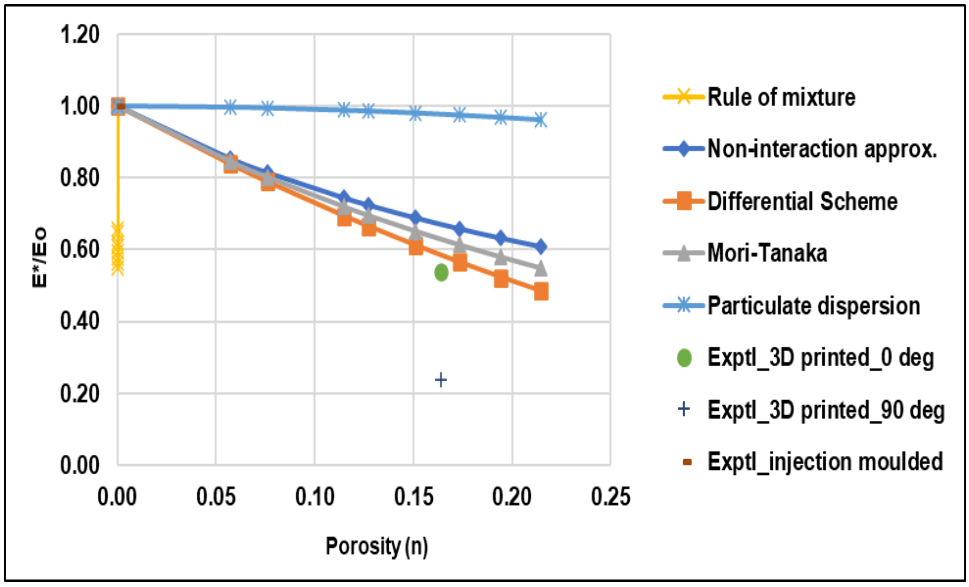

Figure 5.9: Comparison of experimental elastic modulus with analytical porosity-based equations (Cramer and Sevostianov 2009)

It is **observed** from the above graph that Differential scheme and Mori-Tanaka scheme closely predicted experimental values, but rule of mixture and particulate dispersion stiffness models failed to match experimental results.

5.4 Conclusions

From analytical strength prediction models, based on reduction in mechanical properties due to porosity, proposed by different researchers, it is observed that:

- For 0^o tension specimen, the Power law equation with empirical constant m=4; and Ryshkewitch and Duckworth (1953) with empirical constant b=4.5; are in fine agreement with experimental values. But Li Li and Michel Aubertin with x=4, over predicts the strength for certain range and then suddenly under predicts the strength vs porosity values for other ranges.
- For 90^o tension specimen, Power law equation with empirical constant m=9; Ryshkewitch and Duckworth (1953) with empirical constant b=10 and Li Li & Michel Aubertin with x=1.5 provide good comparison with experimental values.
- From analytical stiffness predictions models, Differential scheme and Mori-Tanaka scheme predicted the experimental values with <15% difference, but the rule of mixture and particulate dispersion stiffness models had >50% difference compared to experimental results.

CHAPTER 6

ANALYSIS OF FAILURE CRITERIA APPLICABLE TO PLA

6 Analysis of failure criteria applicable to PLA (Phase -III)

Phase-III developed failure criteria of 3D printed PLA specimens at 0^o, 30^o, 45^o, 60^o & 90^o orientations based on quasi-static of compression and tensile results. Various failure criteria are considered to predict the strength at combined loads. By using the mechanical properties and the equations of each failure criterion, the failure envelope curves for PLA is achieved. To generate failure criteria MATLAB code is used in this study.

6.1 Static test on 3D Printed PLA Prism specimens

The compressive properties of PLA specimens in different orientations (i.e., 0°, 30°, 45°, 60°, and 90°), produced with the FDM technique implemented in an Ultimaker^{2+} 3D printer. The reference standard for the determination of compressive properties of plastic materials is "ASTM D-695 – 02a Standard Test Method for Compressive Properties of Rigid Plastics" (ASTM D695 2010). In the case of isotropic materials, at least five specimens must be tested. For this reason, ten specimens were employed in the present test. When compressive strength is desired, the specimens must have the form of a right cylinder or prism where the length is twice its principal width or diameter. A rectangular specimen suitable for compressive testing has been chosen for the study of static compression behaviour (Brischetto et al. 2017).

6.1.1 Materials and specimen fabrication (Prism specimens)

The materials tested in this study used poly-lactic acid (PLA) to produce samples in an Ultimaker^{2+} 3D-printer. The specimens and select dimensions for specimen types are shown in Figure 6.1. The prism specimen is first created in Creo, exported in stereo lithography (STL) format, and then imported into each 3D printer's respective slicer software to create the G-code used to print each specimen type.

The layer height, extrusion width, air gap (the space between the bead of material), printing temperature (the temperature of the air around the part and the bed temperature), build plate temperature, nozzle size (width of the hole through which the material is

extruded), and colour, print speed, and infill density are all held constant values. The entire list of constant or default values used during this study is shown in Table 6.1. Like tensile specimens, for investigation of the properties of prism specimens, the orientations selected are 0°, 30°, 45°, 60°, and 90°.The specimens are printed in the 0°, 45° and 90° orientation angles as shown in Figure 6.1. Ten identical specimens are printed for each orientation and the results for all ten tests averaged to find the properties in each direction.

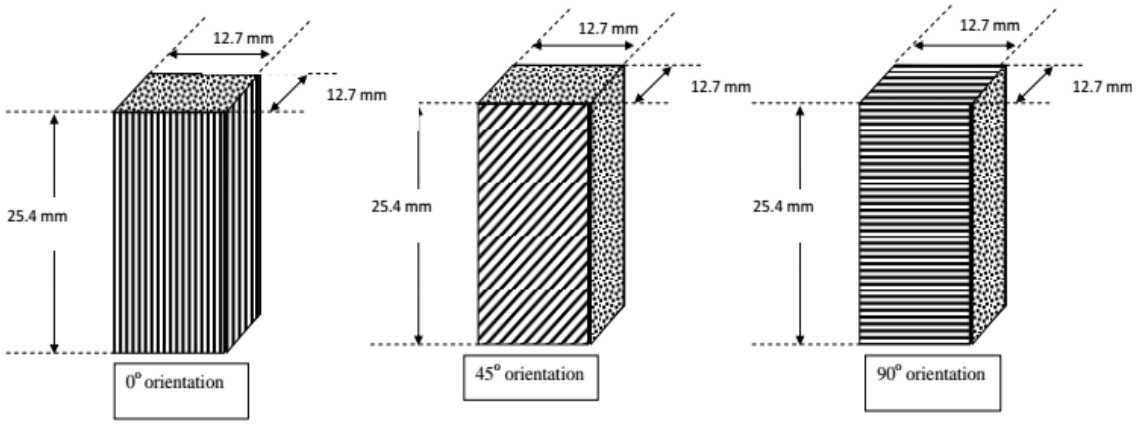

Figure 6.1: Schematic representation of the ASTM D695-02a prism specimen geometry with relevant dimensions in mm. Prism specimen for compression testing with dimensions and orientations.

6.1.2 Experimental set-up for compressive testing of prism specimens

The compression testing of prism specimens is done on a Universal testing machine (UTM) of capacity 30KN (Fig.6.2). Before starting the experiment, it is compulsory to measure the width and thickness of each specimen to the nearest 0.01 mm, at several points along its length and record the mean value. The length of each specimen must be also measured. All dimensions are measured using digital vernier calliper. All the specimens are tested at room temperature with a load cell of 10kN and displacement rate of 1 mm/min, till failure of the specimen. The program noted the load applied and the corresponding displacement by measuring the distance moved by the crossheads. The compressive strength results obtained from the experiments are shown in Table 6.2 in next section.

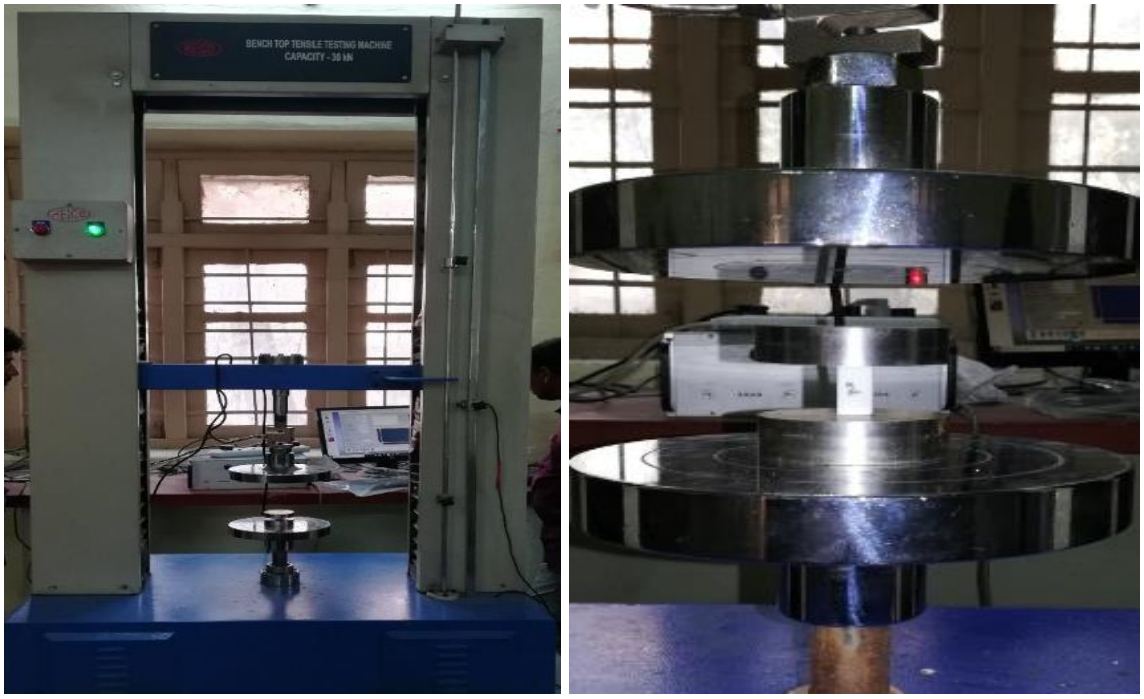

(a) **(b)**

Figure 6.2: (a) UTM of 30kN capacity used for compressive testing, (b) Experimental set-up for compression testing.

6.2 Static test on 3D Printed PLA Dogbone specimens

The materials tested in this study is poly-lactic acid (PLA) which are used to produce samples in an Ultimaker2+ 3D-printer. The specimen geometries followed specifications outlined in ASTM D-638 for Type V tensile specimens ("Standard Test Method for Tensile Properties of Plastics 1," n.d.). The specimens and select dimensions for specimen types are shown in Fig.6.3. The specimen is printed at a thickness of 2 mm (0.0787 in). The tensile specimen is first created in Creo, exported in stereo lithography (STL) format, and then imported into each 3D printer's respective slicer software to create the G-code used to print each specimen type in different orientations of 0°, 30°, 45°, 60°, and 90°.

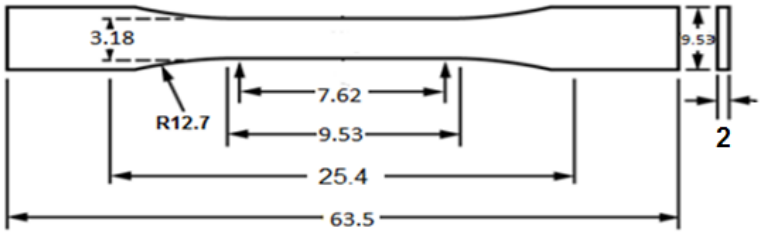

Figure 6.3: Schematic representation of the ASTM D638 Type V tensile specimen geometry with relevant dimensions in mm

6.2.1 Materials and specimen fabrication (Dogbone specimens)

The specimens printed on the Ultimaker^{2+} used a default slice height of 0.1 mm (0.004 in.) and extrusion width (the width of each layer of deposited material, also known as the road width) of 0.35 mm (0.016 in). The layer height, extrusion width, air gap (the space between the bead of material), printing temperature (the temperature of the air around the part and the bed temperature), build plate temperature, nozzle size (width of the hole through which the material is extruded), and colour, print speed, and infill density are all kept constant values. The entire list of constant or default values used during this study is shown in Table 6.1. Like compressive specimens, for investigation of the properties of dogbone specimens, the orientation angles selected are 0°, 45° and 90° directions as shown in Fig. 6.4. Ten identical specimens are printed for each orientation and the results for all ten tests averaged to find the properties in each direction.

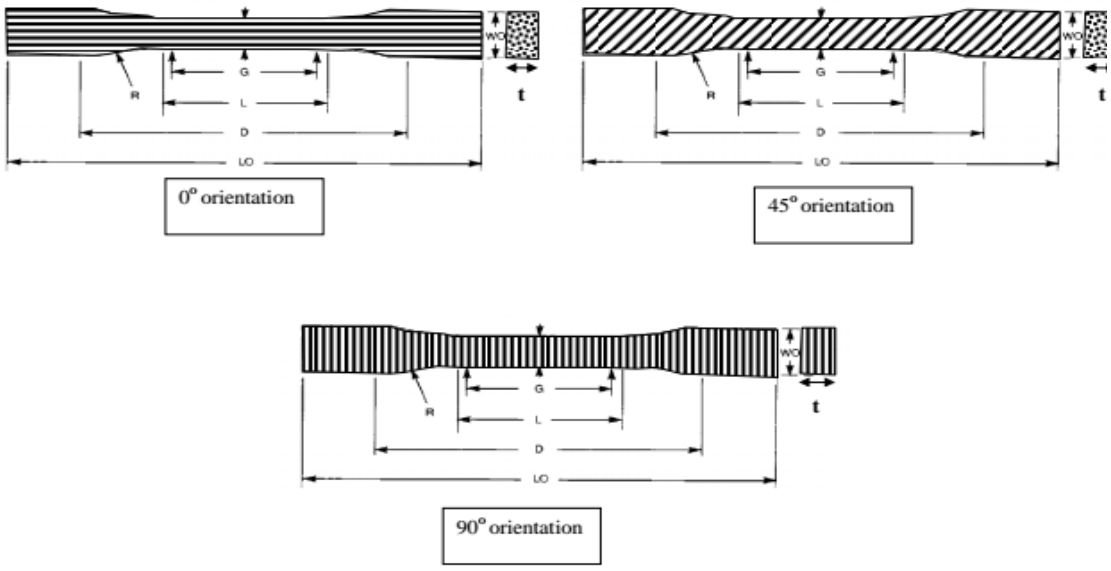

Figure 6.4: Different printing orientations for Dog-Bone specimen

Table 6.1: Constant 3D-printing process settings for the Ultimaker2+ printer

Parameter	Ultimaker^{2+} PLA value
Air gap (mm)	0.0
Layer height (mm)	0.1
Extrusion width (mm)	0.35
Nozzle size (mm)	0.4

Filament color	White
Infill Density (%)	100
Wall thickness (mm)	0.1
Printing Temperature (°C)	200
Build plate temperature (°C)	60
Print speed (mm/s)	50

6.2.2 Experimental set-up for tensile testing of Dogbone specimens

The tensile testing of dog-bone specimens is done on Universal testing machine (UTM) of capacity 100kN, according to ASTM D 638-14 "Standard Test Method for Tensile Properties of Plastics" ("Standard Test Method for Tensile Properties of Plastics 1," n.d.). Before the commencement of the test, all dimensions of specimens are measured at three different locations using vernier calliper and the mean value is taken. All the specimens are tested at room temperature with a load cell of 5kN and displacement rate of 1 mm/min, till failure of the specimen. The program noted the load applied and the corresponding displacement by measuring the distance moved by the crossheads. For tensile testing the average stress in the specimen, at any given load, is determined by dividing the load by the cross-sectional area. The strain is determined by dividing crosshead displacement by gauge length.

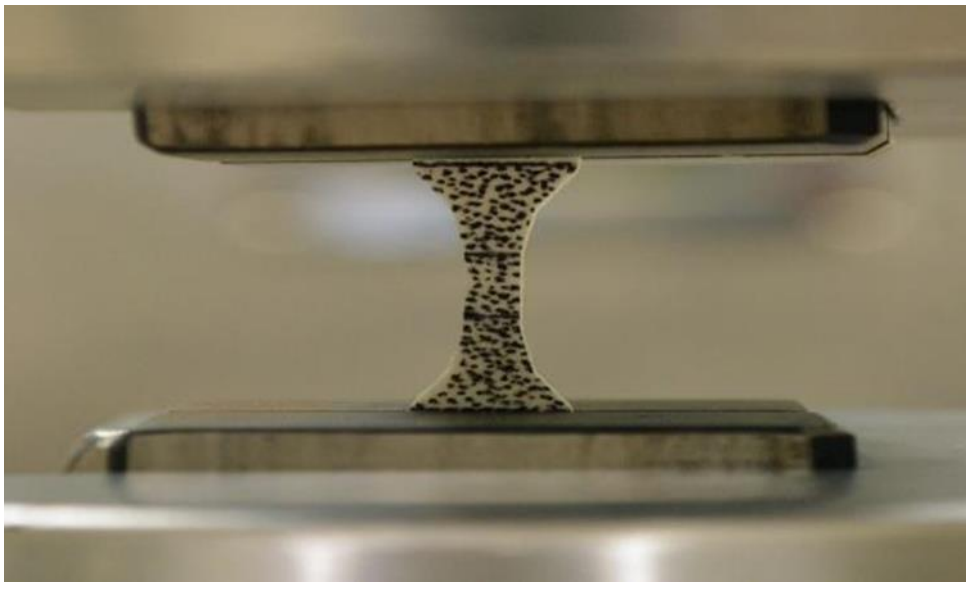

Figure 6.5: Experimental set-up for tensile testing

6.3 Results and Discussions

6.3.1 Quasi-static compression behavior of prism specimen

The stress vs stress curves of quasi static compressive tests on 3D printed prism specimens each orientations 0°, 30°, 45°, 60°, and 90° of 12.7 mm * 12.7 mm * 25.4 mm are shown in Figure 6.6 respectively.

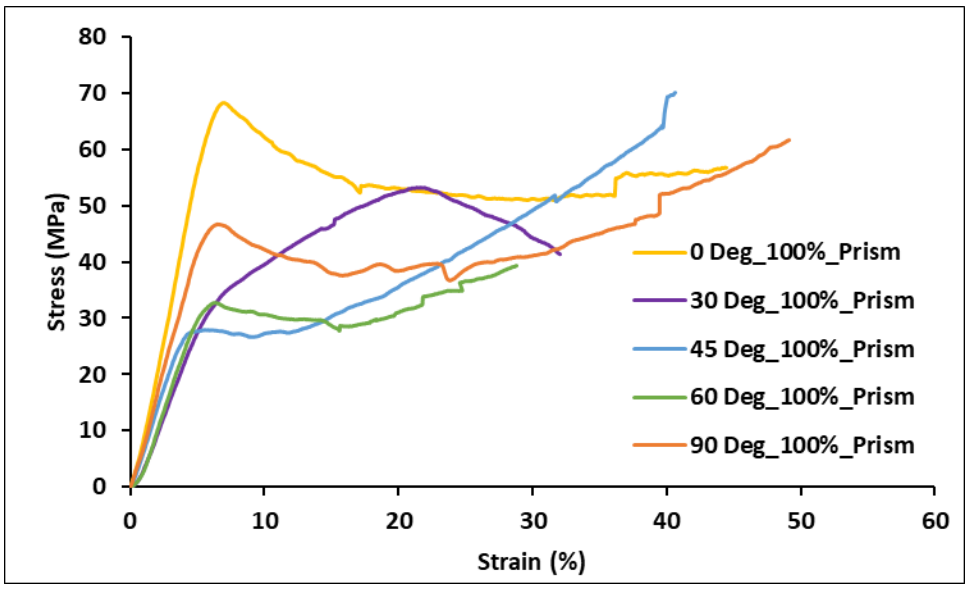

Figure 6.6: Average compressive experimental response for 3D printed specimens of 0º, 30º, 45º, 60º & 90º orientations

Table 6.2: Average value of crushing load, compressive strength and Young's modulus of 0º, 30º, 45º, 60º & 90º 3D printed prism specimens

Specimen orientation	Crushing Load (kN)	Compressive Strength (MPa)	Young's Modulus, E (MPa)
0^o	11.41	70.19	1112.6
30^o	8.92	53.97	624.23
45^o	4.57	28.39	713.25
60^o	5.57	33.79	679.30
90^o	7.49	46.17	1032.55

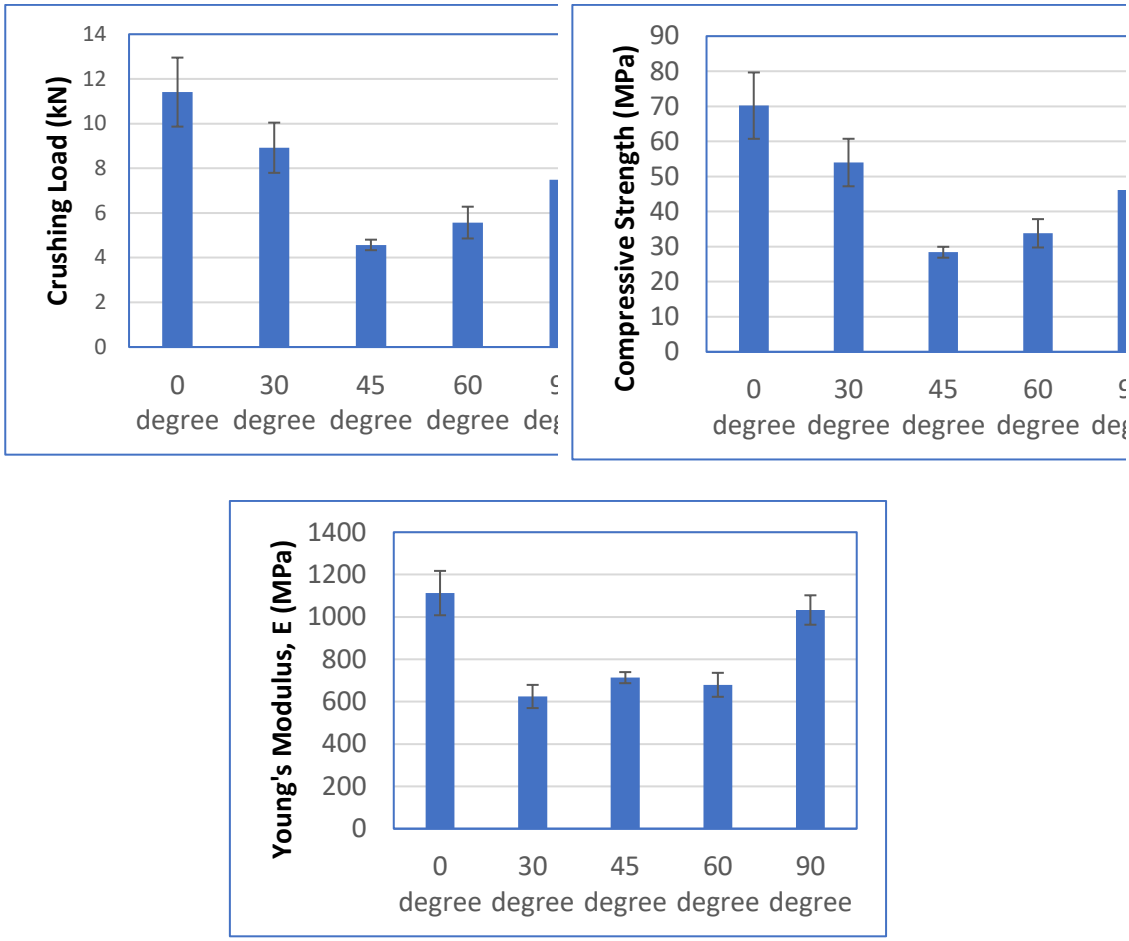

Figure 6.7: Average value of (a) crushing load, (b) compressive strength and (c) young's modulus of 0º, 30º, 45º, 60º & 90º 3D printed prism specimens and error bar shows the standard deviation

It is observed from the uniaxial compression test on prism specimen, that 0^o orientation specimen have higher compressive strength (70.19 MPa), and crushing load (11.41 kN) while 45^o orientation specimen have lower compressive strength (28.39 MPa), and crushing load (4.57 kN). 0^o orientation specimen have higher compressive modulus (1112.6 MPa) while 30^o orientation specimen have lower compressive modulus (624.23 MPa)

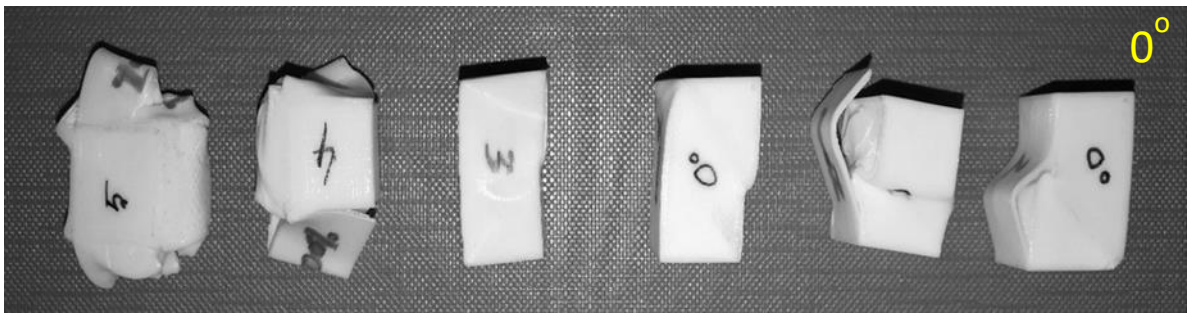

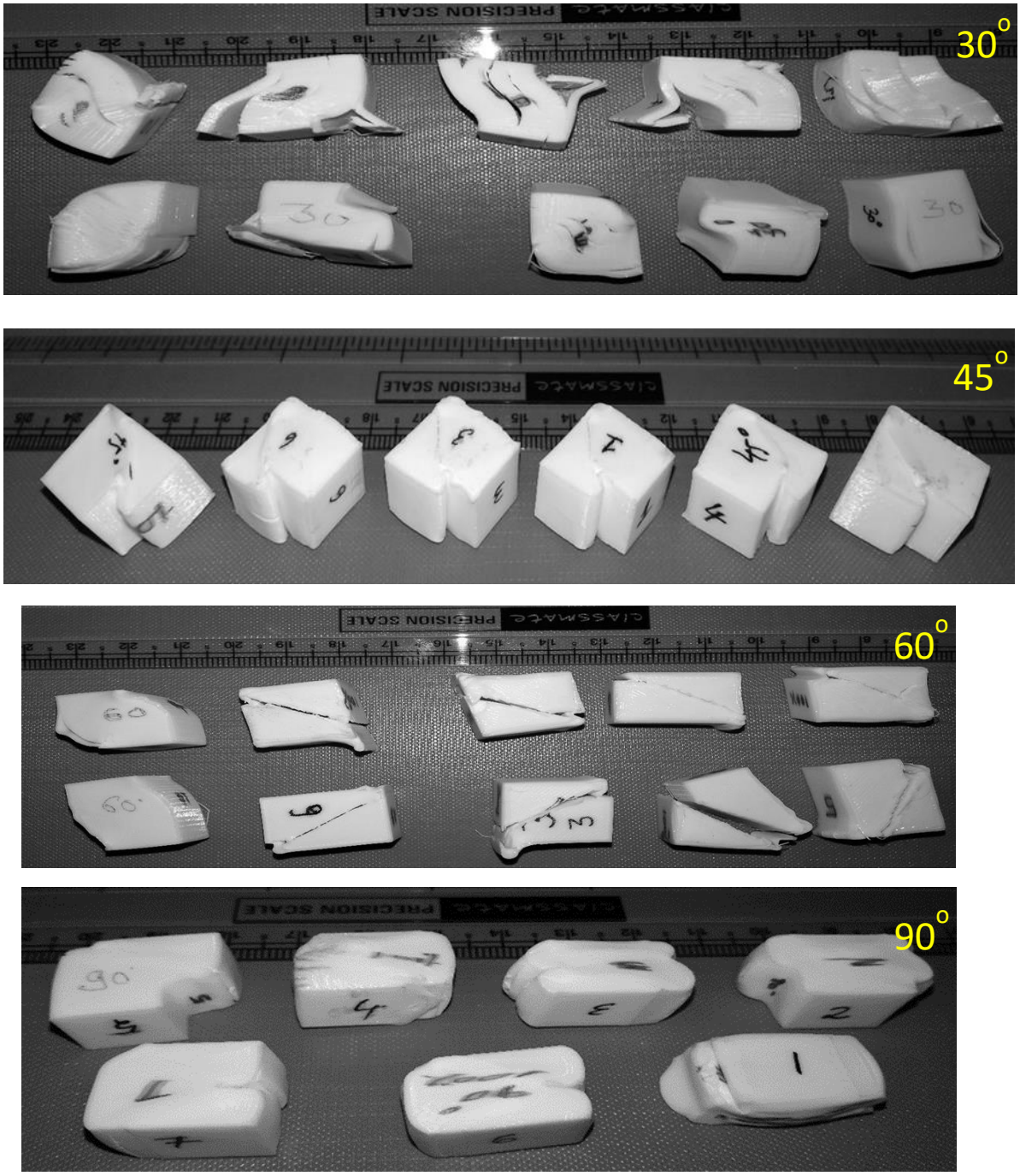

Figure 6.8: Compressive Specimens for 0^o, 30^o, 45^o, 60^o & 90^o after failure

Failure mode of compressive specimen can be clearly observed by looking at the final shape of specimen after testing it (Fig.6.8).

The 0^o specimens fail due to buckling of strand and weak bond between strands because stress is applied along each layer of specimen. The strength of 0^o specimen is very high because individual strands can take load and the effect of bonding can be minimized.

The 90^{o} orientation specimens are found to fail from excessive deformation. The 90^{o} specimen after testing can be seen in Fig.6.8. This specimen shows force which is directly perpendicular to the printed layers. This allows it to have high strength since there is no interaction between shear or buckling forces and the weak interlayer bonds.

For specimen with 45° orientation angle, strand is deposited at 45° to the loading direction and failure takes place along with strand deposition through strand-to-strand bonding (Fig.6.8) which is relatively weaker than the individual strand. 45° specimens fail in shear. At the time of testing of 45° specimen at initial stage, cracks propagate and then reorientation of fibre take place and then again it bears the load.

For specimen with 30° and 60^{o} orientation angles, the strands are deposited at 30° and 60^{o} to the loading direction and failure takes place along with strand deposition through strand-to-strand bonding (Fig.6.8) which is relatively weaker than the individual strand. 30^{o} and 60^{o} specimens fail due to buckling and shear.

6.3.2 Quasi-static tensile behavior of dogbone specimen

The stress vs stress curves of quasi static tensile tests on 3D printed dogbone specimens each orientations of 0°, 30°, 45°, 60°, and 90° are shown in Figure 6.9 respectively.

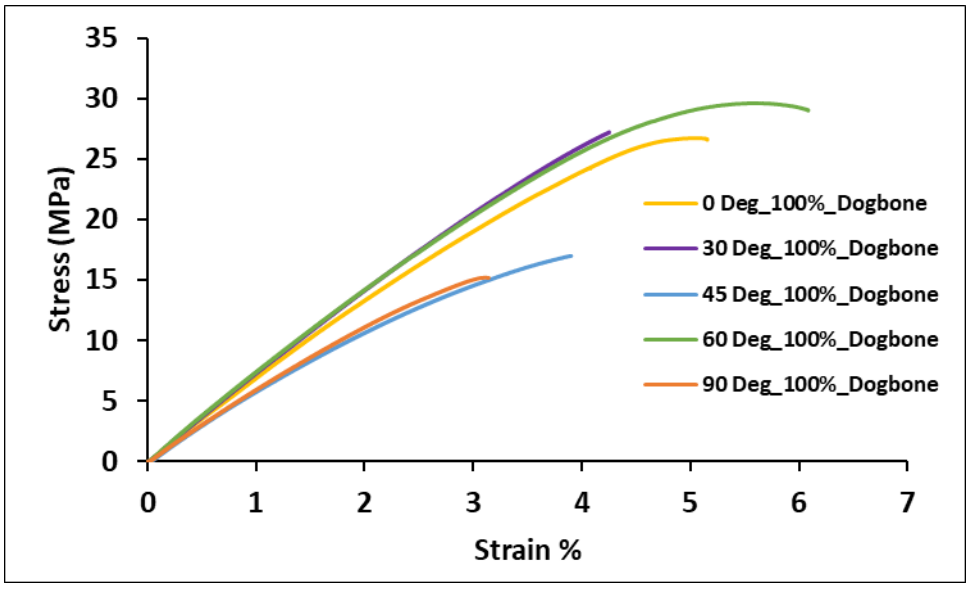

Figure 6.9: Average tensile experimental response for 3D printed specimens of 0^{o}, 30^{o}, 45^{o}, 60^{o} & 90^{o} orientations.

Table 6.3: Average value of ultimate tensile strength, strain @ failure, toughness and Young's modulus.

Specimen Type	Ultimate Tensile Strength (MPa)	Strain @ failure (%)	Toughness ($M.J.m^{-3}$)	Young's Modulus (MPa)
0^o	28.86	6.22	0.754	720.4
30^o	30.85	5.85	1.122	712.6
45^o	18.11	6.41	0.535	558.1
60^o	30.11	7.96	1.667	716
90^o	18.96	3.81	0.242	587.3

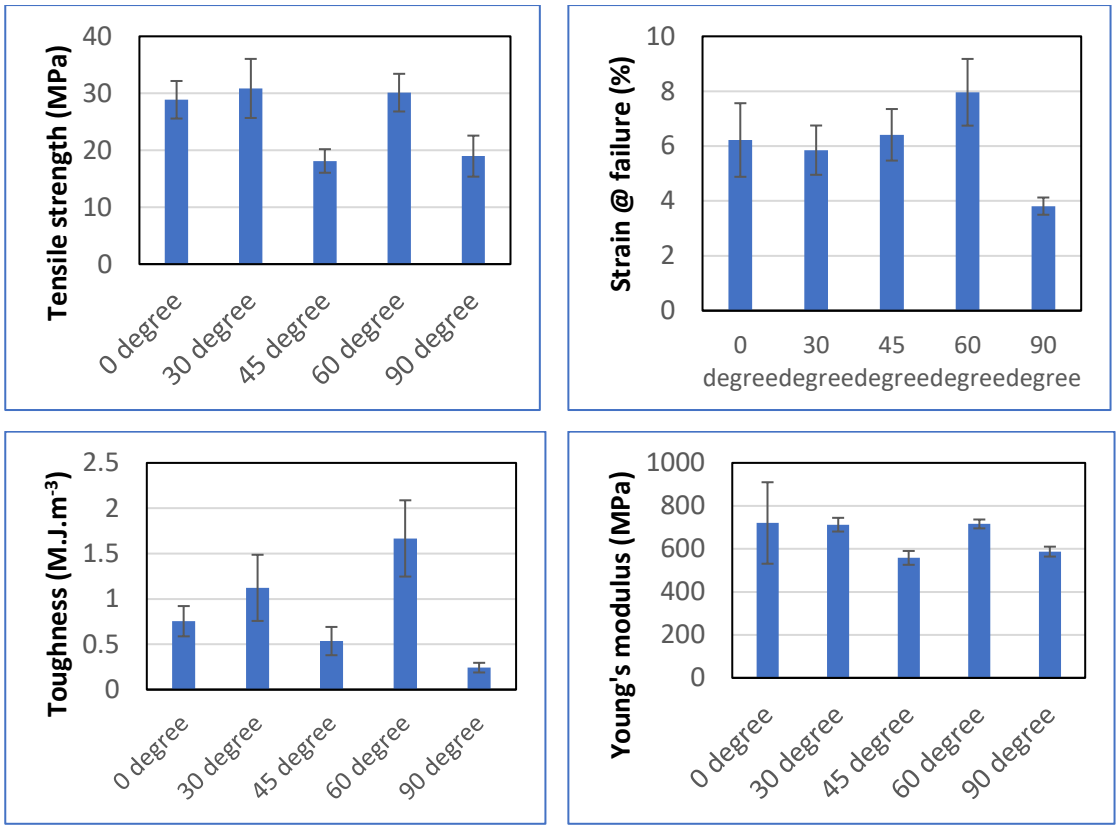

Figure 6.10: Results obtained from tensile test of dog-bone specimen and error bar shows the standard deviation

Observations from tensile test

It is observed from the uniaxial tensile test on dog-bone specimen of 0^o, 30^o and 60^o orientation that they have similar ultimate tensile strength (30 MPa). This is 70% and 62.71% greater than at 45^o and 90^o orientation angles respectively. 0^o, 30^o and 60^o orientation angles have similar Young's modulus (720 MPa) which is 29% and 22.66% greater than at 45^o and 90^o orientation angles respectively. The strain at failure (7.96%)

and toughness (1.667 $M.J.m^{-3}$) of 60^o orientation is greater compared to the other orientations (0^o, 30^o, 45^o, 60^o and 90^o).

From Fig.6.11 at 0° orientation angle, all the strands are deposited parallel to the loading direction. Due to the parallel deposition of strands, each individual strand takes the load and the effect of bonding between strands can be minimized. The failure of the specimen takes place due to individual pulling and necking of each individual strand as a function of tensile loading.

For specimens with 90° orientation angle, force is exerted perpendicular to the direction of strand deposition with the result that strand-to-strand bonding becomes the resistance mechanism. The strength in 90° layer depends on the bonding between adjacent strands, which is always weaker than the strength of strand. As the strength of the strand-to-strand bonding is lower than the strength of the individual strand, it results in bond failure at lower stresses and hence lower tensile strength.

For specimens with 30° orientation angle, strand is deposited at 30° to the loading direction and failure took place along with strand deposition through strand-to-strand bonding, which is relatively weaker than the individual strand.

For specimens with 60° orientation angle, strand is deposited 60° to the loading direction, and again failure occurred along with strand deposition. The failure took through the strand bonding, which is relatively weaker.

For specimens with 45° orientation angle, strand is deposited at 45° to loading direction and failure took place along strand deposition though bonding between adjacent strands. Bonding between strands showed relatively lower strength which results in poor strength.

From the tensile experiments, higher tensile strength has been obtained at 0° orientation angle, while lower strength has been observed at 90°orientation angle.

In unidirectional strand angle, failure takes place along with strand deposition through strand bonding except for 0° strand angle.

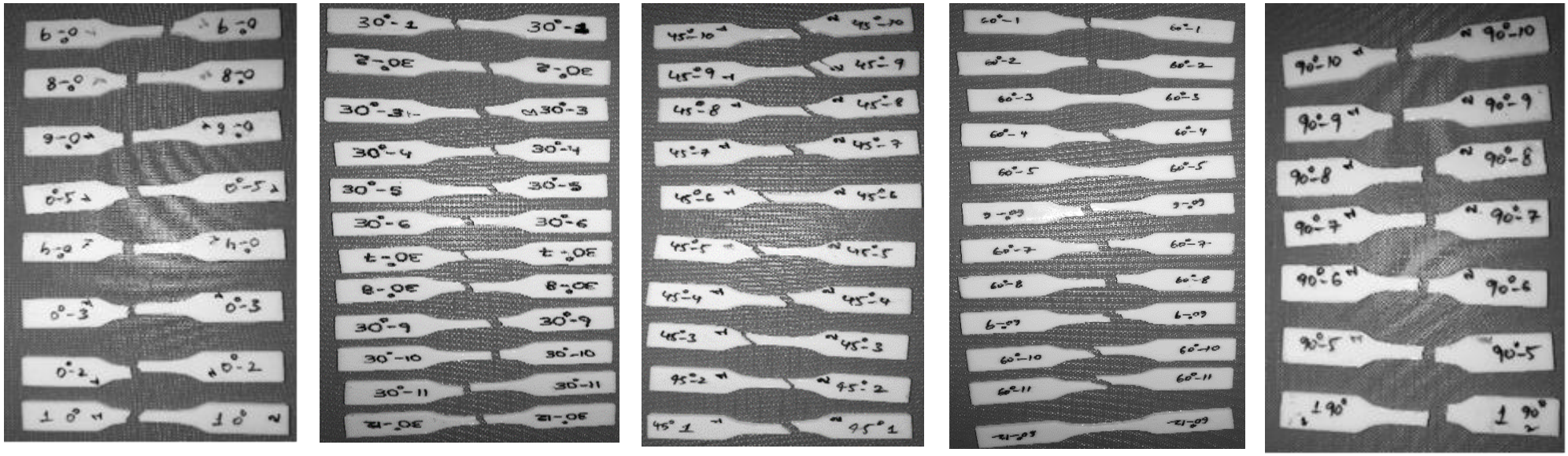

Figure 6.11: Tensile Specimens for 0^o, 30^o, 45^o, 60^o & 90^o after failure

6.3.3 Analytical modelling of failure criteria for 3D printed PLA

Various failure criteria applicable to composite materials are evaluated for applicability in predicting failure in 3D printed PLA material. The experimental data obtained from tensile and compressive experiments as detailed in section 6.3.1 and 6.3.2 is fitted to various failure models (Table 6.4) as detailed in Table 6.6 and shown in Fig. 6.12-6.15.

Table 6.4: Various failure criteria suitable for composites (Mascia and Simoni 2013)

Hoffman criterion	$\frac{\sigma_1^2}{f_{t1}.f_{c1}}+\frac{\sigma_2^2}{f_{t2}.f_{c2}}-\frac{\sigma_1\sigma_2}{f_{t1}.f_{c1}}+\frac{\tau_{12}^2}{f_{v4}^2}+\frac{f_{c1}-f_{t1}}{f_{t1}.f_{c1}}\sigma_1+\frac{f_{c2}-f_{t2}}{f_{t2}.f_{c2}}\sigma_2=1$
Tsai – Wu criterion	$\frac{\sigma_1^2}{f_{t1}.f_{c1}}+\frac{\sigma_2^2}{f_{t2}.f_{c2}}-\frac{\sigma_1\sigma_2}{\sqrt{\frac{1}{f_{t1}.f_{c1}}}\sqrt{\frac{1}{f_{t2}.f_{c2}}}}+\frac{\tau_{12}^2}{f_{v4}^2}+\frac{f_{c1}-f_{t1}}{f_{t1}.f_{c1}}\sigma_1+\frac{f_{c2}-f_{t2}}{f_{t2}.f_{c2}}\sigma_2=1$
Norris criterion	Norris criterion equations for each quadrant. Quadrant 1 ($\sigma_1\geq 0,\sigma_2\geq 0$) $\frac{\sigma_1^2}{f_{t1}^2}+\frac{\sigma_2^2}{f_{t2}^2}-\frac{\sigma_1.\sigma_2}{f_{t1}.f_{t2}}+\frac{\tau_{12}^2}{f_v^2}=1$ Quadrant 2 ($\sigma_1\leq 0,\sigma_2\geq 0$) $\frac{\sigma_1^2}{f_{c1}^2}+\frac{\sigma_2^2}{f_{t2}^2}-\frac{\sigma_1.\sigma_2}{f_{c1}.f_{t2}}+\frac{\tau_{12}^2}{f_v^2}=1$ Quadrant 3 ($\sigma_1\leq 0,\sigma_2\leq 0$) $\frac{\sigma_1^2}{f_{c1}^2}+\frac{\sigma_2^2}{f_{c2}^2}-\frac{\sigma_1.\sigma_2}{f_{c1}.f_{c2}}+\frac{\tau_{12}^2}{f_v^2}=1$ Quadrant 4 ($\sigma_1\geq 0,\sigma_2\leq 0$) $\frac{\sigma_1^2}{f_{t1}^2}+\frac{\sigma_2^2}{f_{c2}^2}-\frac{\sigma_1.\sigma_2}{f_{t1}.f_{c2}}+\frac{\tau_{12}^2}{f_v^2}=1$
Tsai – Hill criterion	Tsai - Hill criterion equations for each quadrant. Quadrant 1 ($\sigma_1\geq 0,\sigma_2\geq 0$) $\frac{\sigma_1^2}{f_{t1}^2}+\frac{\sigma_2^2}{f_{t2}^2}-\left(\frac{\sigma_1.\sigma_2}{f_{t1}^2}\right)+\frac{\tau_{12}^2}{f_{v4}^2}=1$ Quadrant 2 ($\sigma_1\leq 0,\sigma_2\geq 0$) $\frac{\sigma_1^2}{f_{c1}^2}+\frac{\sigma_2^2}{f_{t2}^2}-\left(\frac{\sigma_1.\sigma_2}{f_{c1}^2}\right)+\frac{\tau_{12}^2}{f_{v4}^2}=1$ Quadrant 3 ($\sigma_1\leq 0,\sigma_2\leq 0$) $\frac{\sigma_1^2}{f_{c1}^2}+\frac{\sigma_2^2}{f_{c2}^2}-\left(\frac{\sigma_1.\sigma_2}{f_{c1}^2}\right)+\frac{\tau_{12}^2}{f_{v4}^2}=1$ Quadrant 4 ($\sigma_1\geq 0,\sigma_2\leq 0$) $\frac{\sigma_1^2}{f_{t1}^2}+\frac{\sigma_2^2}{f_{c2}^2}-\left(\frac{\sigma_1.\sigma_2}{f_{t1}^2}\right)+\frac{\tau_{12}^2}{f_{v4}^2}=1$

Table 6.5 Values of mechanical properties of 3D printed PLA

Properties	Values (MPa)		
	Max	Mean	S.D.
f_{t_1}- Tensile strength along direction 1	33.164	28.86	3.3
f_{t_2}- Tensile strength along direction 2	24.48	20.81	2.64
f_{c_1}- Compressive strength along direction 1	71.14	66.97	6.61
f_{c_2}- Compressive strength along direction 2	54.812	53.80	0.68
f_{v_4}- Shear strength in 1–2 plane	12.493	10.05	2.07

Table 6.6: Calculations for failure criteria of 3D printed PLA

Hoffman criterion	$\frac{\sigma_1^2}{1932.759}+\frac{\sigma_2^2}{1119.879}-\frac{\sigma_1\sigma_2}{1932.759}+\frac{\tau_{12}^2}{101.122}+0.020\,\sigma_1+0.029\,\sigma_2=1$
Tsai – Wu criterion	$\frac{\sigma_1^2}{1932.759}+\frac{\sigma_2^2}{1119.879}-\frac{\sigma_1\sigma_2}{1502.832}+\frac{\tau_{12}^2}{101.122}+0.020\,\sigma_1+0.029\,\sigma_2=1$
Norris criterion	$\frac{\sigma_1^2}{832.842}+\frac{\sigma_2^2}{433.159}-\frac{\sigma_1\sigma_2}{600.6}+\frac{\tau_{12}^2}{101.122}=1$ $\frac{\sigma_1^2}{4485.316}+\frac{\sigma_2^2}{433.159}-\frac{\sigma_1\sigma_2}{1393.864}+\frac{\tau_{12}^2}{101.122}=1$ $\frac{\sigma_1^2}{4485.316}+\frac{\sigma_2^2}{2895.308}-\frac{\sigma_1\sigma_2}{3603.66}+\frac{\tau_{12}^2}{101.122}=1$ $\frac{\sigma_1^2}{832.842}+\frac{\sigma_2^2}{2895.308}-\frac{\sigma_1\sigma_2}{1552.847}+\frac{\tau_{12}^2}{101.122}=1$
Tsai – Hill criterion	$\frac{\sigma_1^2}{832.842}+\frac{\sigma_2^2}{433.159}-\frac{\sigma_1\sigma_2}{832.842}+\frac{\tau_{12}^2}{101.122}=1$ $\frac{\sigma_1^2}{4485.316}+\frac{\sigma_2^2}{433.159}-\frac{\sigma_1\sigma_2}{4485.316}+\frac{\tau_{12}^2}{101.122}=1$ $\frac{\sigma_1^2}{4485.316}+\frac{\sigma_2^2}{2895.3O8}-\frac{\sigma_1\sigma_2}{4484.316}+\frac{\tau_{12}^2}{101.122}=1$ $\frac{\sigma_1^2}{832.842}+\frac{\sigma_2^2}{2895.308}-\frac{\sigma_1\sigma_2}{832.842}+\frac{\tau_{12}^2}{101.122}=1$

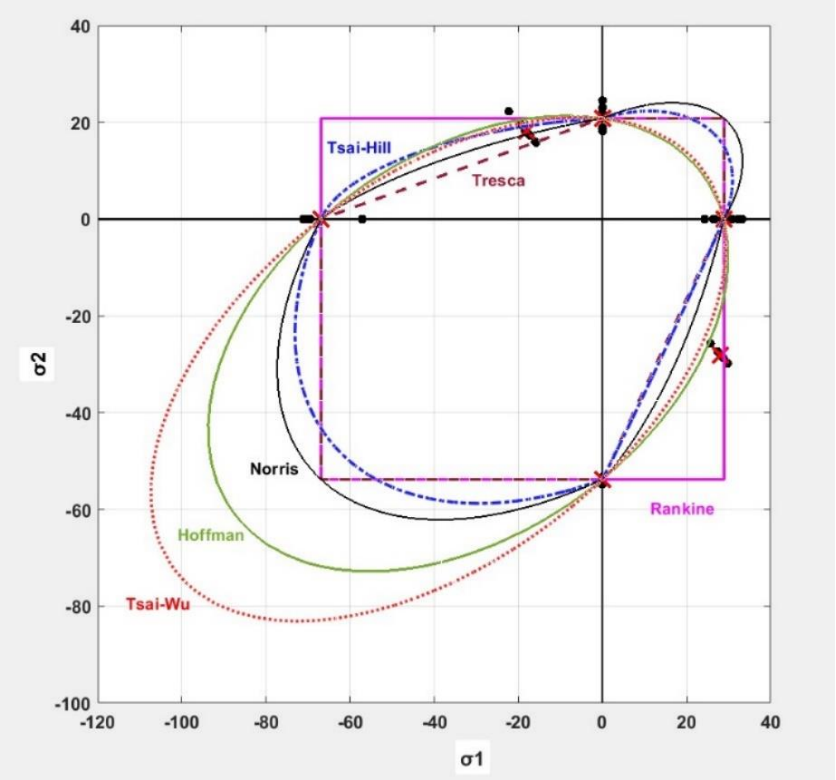

Figure 6.12: Average 2D failure criteria for 3D printed PLA ($\tau_{12} = 0$)

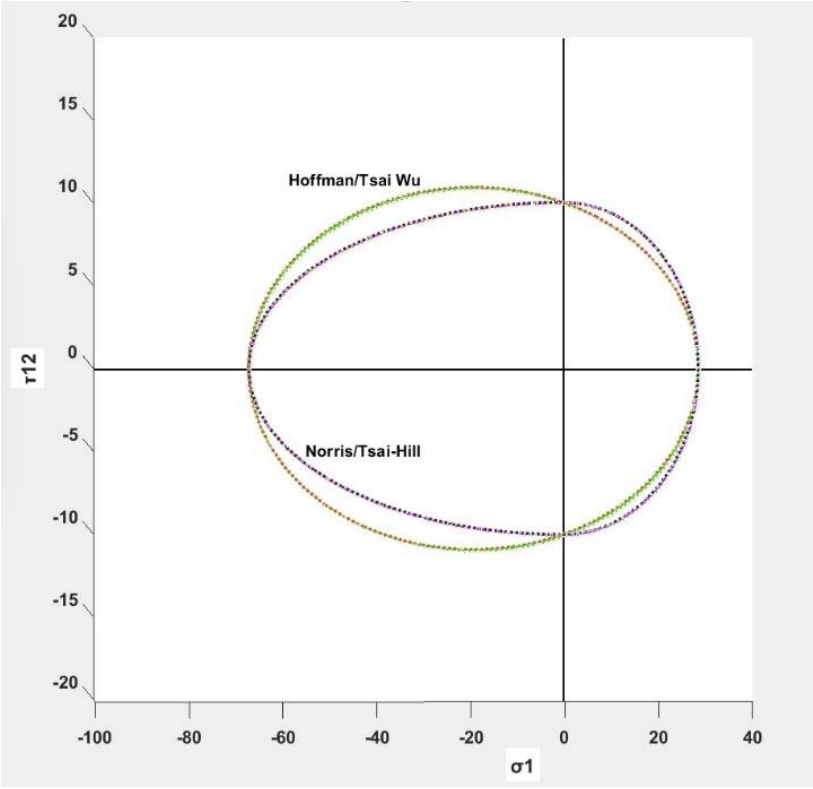

Figure 6.13: Average 2D failure criteria for 3D printed PLA ($\sigma_2 = 0$)

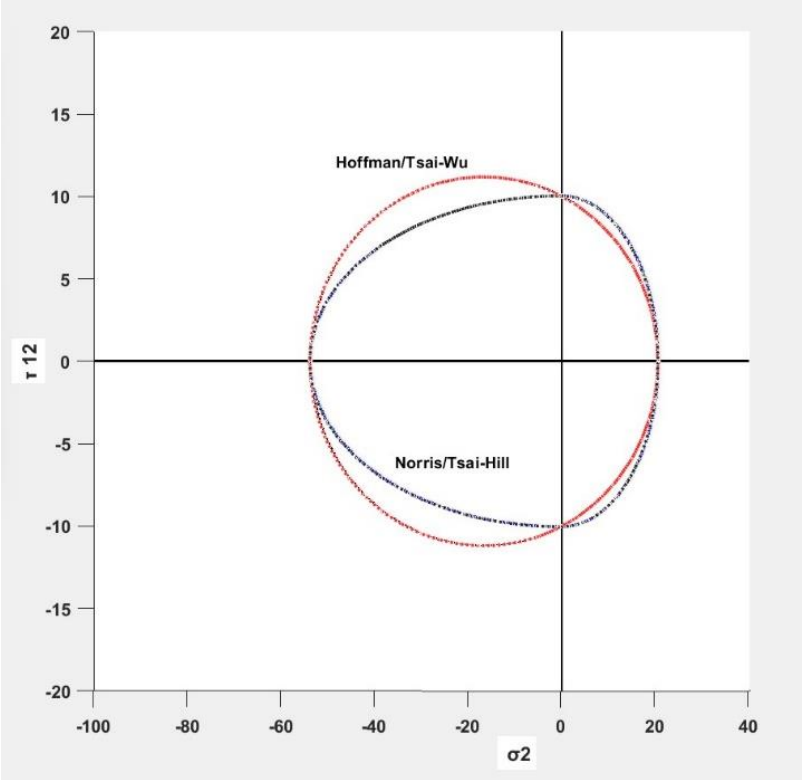

Figure 6.14: Average 2D failure criteria for 3D printed PLA ($\sigma_1 = 0$)

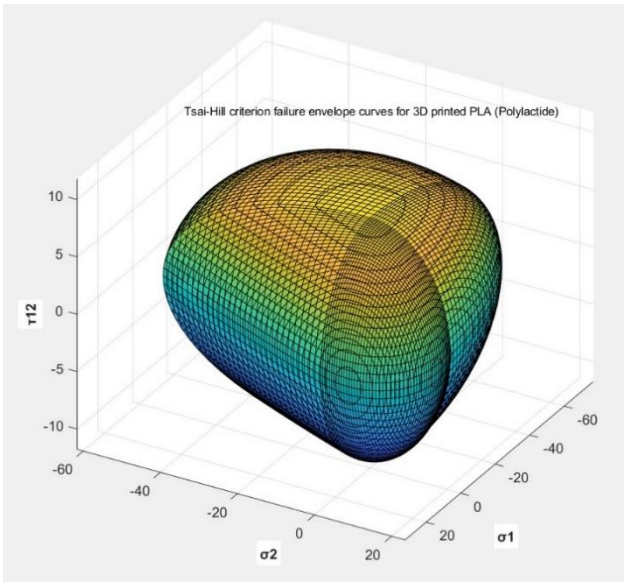

(a)

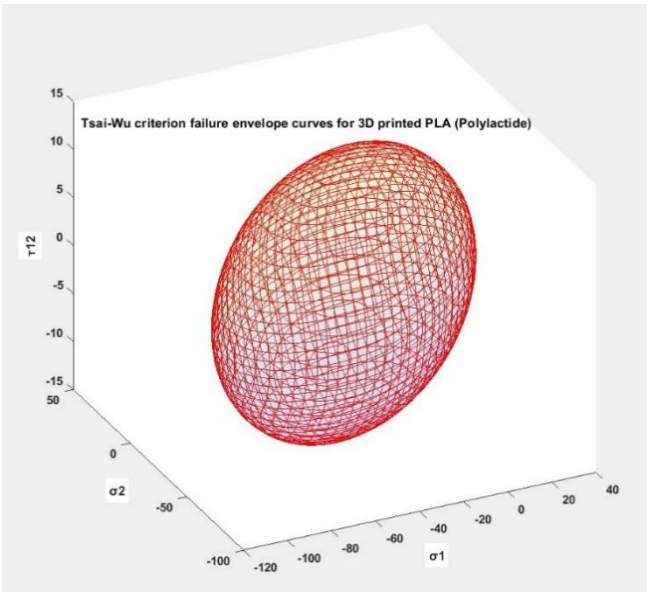

(b)

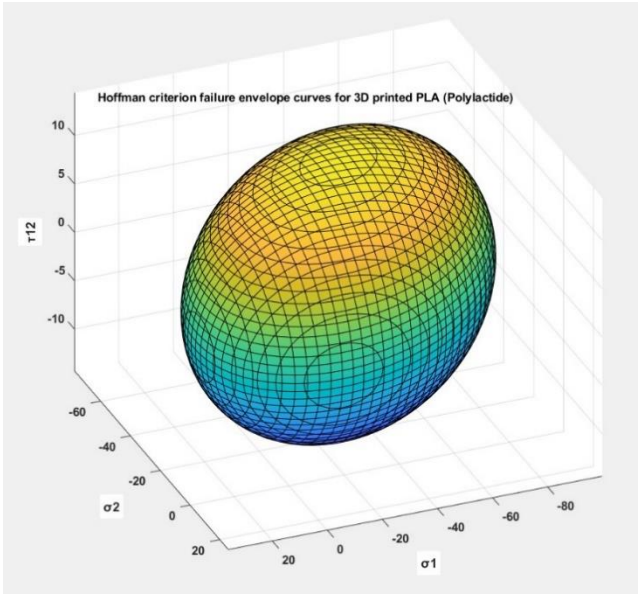

(c)

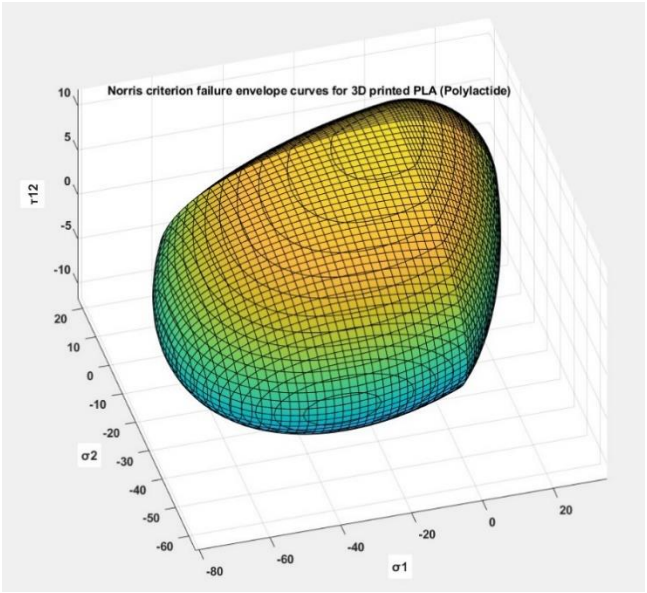

(d)

Figure 6.15: Average 3D failure surface for 3D printed PLA (a) Tsai-Hill (b) Tsai-Wu (c) Hoffman (d) Norris criterion

6.4 Discussion & Conclusions

Tsai-Wu predicts highest bi-axial compressive strength (Quadrant – III), Norris predicts highest bi-axial tensile strength (Quadrant -I). Also, Tsai – Wu and Hoffman showed identical predictions in I, II and IV Quadrants. Tsai – Hill overlaps with Hoffman in quadrant – II and with Tresca in quadrant IV. Average experimental strength value for quadrant IV coincides with Rankine and in quadrant II it coincides with Norris. It is found that among the various models considered in this study, the Norris criteria fits the experimental data most closely in majority of the quadrants and is recommended as most suitable for 3D Printed PLA from amongst the failure criteria considered in this study.

CHAPTER 7

DYNAMIC CHARACTERIZATION OF ADDITIVELY MANUFACTURED POLYLACTIC ACID (PLA)

7 Dynamic characterization of AM Polylactic acid (PLA) (Phase – IV)

This chapter presents the characterization of rate dependent compressive mechanical behaviour of 3D printed PLA printed at 0^o, 45^o & 90^o orientations. Quasi static compression tests are conducted on specimens with 100% infill, which enables quantification of the effect of print orientation on strength properties. High strain rate (SHPB) tests are conducted at ambient temperature to characterize dynamic response. A simple empirical flow stress model is proposed in this study, which accounts for the effects of print orientation, porosity and strain softening behaviour in PLA.

7.1 Materials and specimen fabrication

The material tested in this study is polylactic acid (PLA), which is used to produce samples in an Ultimaker^{2+} 3D-printer, by Fused Deposition Modelling (FDM). PLA disk specimens suitable for SHPB testing, are produced with the FDM technique, in three orientations (0^o, 45^o and 90^o) with respect to the axis of compressive loading, at 100% infill ratio. The print infill orientations for each of the three specimen types are shown in Fig.7.1 (a-c). For 3D printing, CAD models of disk specimens are created using CREO software, which is exported in stereolithography (STL) format, into the 3D printer. CURA software automatically created the G-code used to print each specimen type (Fig.7.1). Three specimen types each of print orientation are printed at 100% infill density at ambient room temperature. The print settings are detailed in Table 7.1.

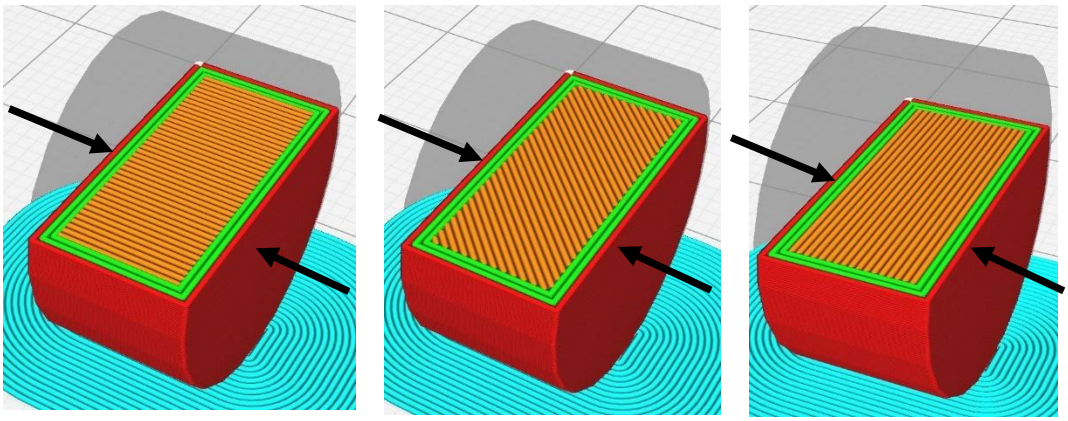

(a) 0º (b) 45º (c) 90º

Figure 7.1 (a-c): FDM model of 0º, 45º and 90º cylindrical specimens.

In general, for high strain rate testing, disk shaped specimens with a diameter of 80% of SHPB bar diameter and having an aspect ratio of 2:1 (diameter = 16 mm and thickness = 8 mm) are used, as shown in Fig.7.2.

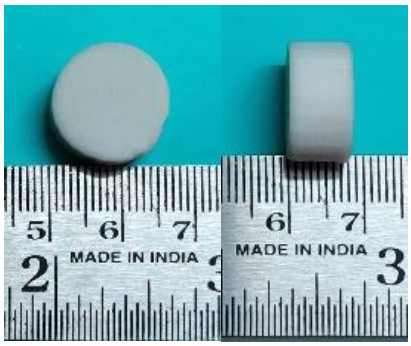

Figure 7.2: FDM disk specimen of diameter = 16 mm and thickness = 8 mm

Table 7.1: FDM process settings for the Ultimaker2+ printer

Parameter	**Setting**
Air gap (mm)	0.0
Layer height (mm)	0.1
Infill distance (mm)	0.35
Nozzle size (mm)	0.4
Filament color	White
Infill density (%)	100
Top/Bottom thickness (mm)	1
Wall thickness (mm)	0.1
Build plate temperature (°C)	60
Printing temperature (°C)	200
Print speed (mm/s)	50
Travel speed (mm/s)	120

7.2 Quasi-static Compressive Testing

The dimensions of all specimens are measured to the nearest 0.01 mm at several points and mean value is recorded. The compression testing of cylindrical specimens is conducted in a universal testing machine (UTM) with a maximum capacity of 100 kN. All specimens are tested under compression at room temperature with a 10 kN load cell and a displacement rate of 1 mm/min until failure of the specimen.

7.3 High Strain Rate Response Characterization

The Split Hopkinson Pressure Bar (SHPB) is a device for experimentally determining the mechanical response of materials at high strain rates ranging from 10 s^{-1} to 10^4 s^{-1}. The material behaviour such as yield stress and ultimate strength, changes with the strain rates, depending on the viscoelastic nature of the material.

The SHPB apparatus consists of a striker, an incident (input) and a transmission (output) bar (Fig.7.3). The instrumentation system comprises of strain gauges, Wheatstone bridge circuit, strain gauge, amplifier, oscilloscope, and velocity sensor, which enable measurement of various strain pulses. The sample is sandwiched between two bars (Fig.7.4). When the striker impacts the incident bar, a compressive stress pulse travels through the bar. When the wave propagates into the specimen, a portion of the wave is reflected, and the remainder is transmitted. These wave trains are detected and post-processed to obtain the stress-strain relationship for the material sandwiched between the rods.

For establishing the dynamic stress-strain relationship of material tested in SHPB, several assumptions are made such as- the incident and transmitted bars should always remain elastic, stress wave propagation in the bar is 1D, the specimen undergoes homogeneous and isotropic deformation across a uniform cross section.

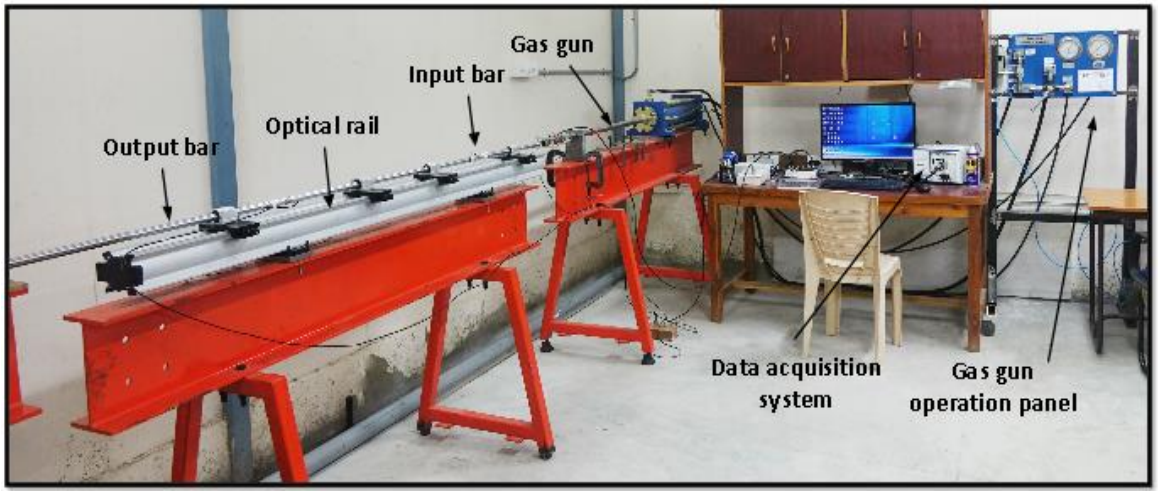

Figure 7.0.3: SHPB testing equipment at IIT Hyderabad

By appropriately integrating the time history of the three waves, one can predict the stress-strain response of the sample material. The dynamic stress and strain (Eqn.7.1 & 7.2) can be acquired from the incident, reflected and transmitted strain pulse as shown below (Hosur et al. 2001):

$$\sigma_s = E\frac{A}{A_S}\varepsilon_t = K_1\varepsilon_t \tag{7.1}$$

$$\varepsilon_s = \frac{-2C_0}{L}\varepsilon_r = K_2\varepsilon_r \tag{7.2}$$

Where σ_s & ε_s is the stress, strain in the specimen and $\varepsilon_i, \varepsilon_r$ & ε_t are strains in the incident, reflected and transmitted bar respectively (Fig.7.4). K_1 and K_2 are the stress and strain rate multiplying factors.

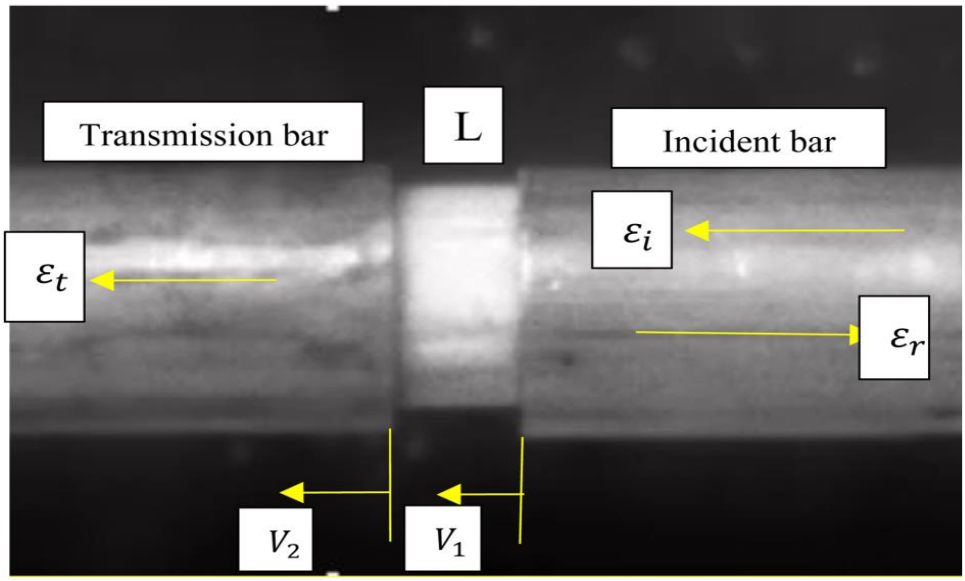

Figure 7.4: Sample sandwiched between transmitted and incident bar.

7.4 Results and Discussion

7.4.1 Quasi-static compression test

Quasi-static compressive specimens are tested at a strain rate of 1 mm/min under displacement control. Results of (average of three specimens) quasi-static compression test on 3D Printed PLA cylindrical specimens with orientations of 0º, 45º and 90º are given in Table 7.2 respectively. The average stress- strain response of three samples for each type of specimen is shown in Fig.7.5.

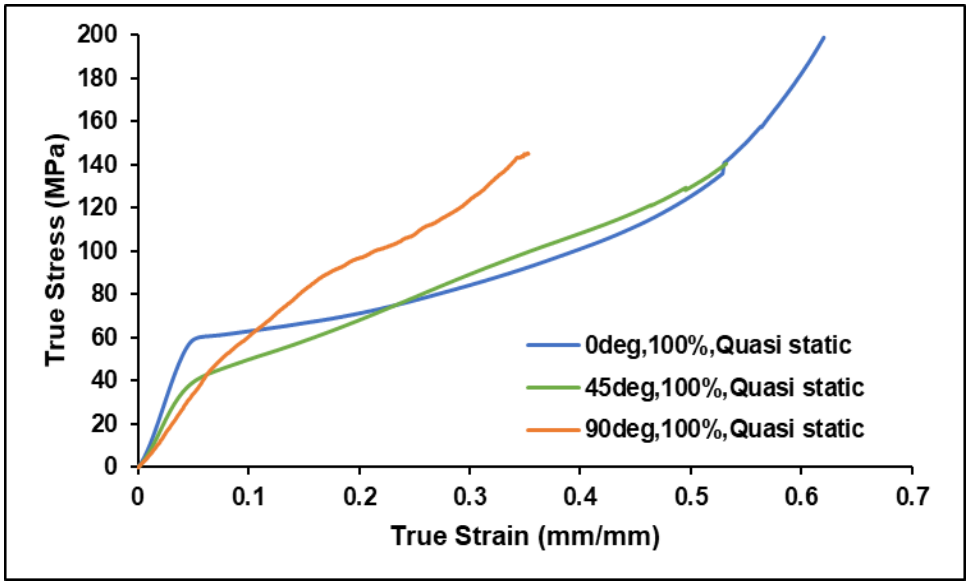

Figure 7.5: Average quasi-static compressive response for 3D printed for 0^o, $45^o$and 90^o orientations.

Table 7.2: Average value of crushing load, compressive strength and Young's modulus of 0^o, 45^o and 90^o 3D printed disk specimen.

Orientation	Crushing load (kN)		Compressive strength (MPa)		Young's modulus, E (MPa)		Toughness (M.J.m-3)	
	Avg	Stdev	Avg	Stdev	Avg	Var	Avg	Stdev
0^o	13	3.146	67	16.288	1303	262.337	53	15.302
45^o	8	0.589	42	3.083	700	55.227	40	4.861
90^o	11	0.3	54	1.49	650	57.867	29	0.588

It is seen from the uniaxial compression tests on disk specimens (Table 7.2), that 0º orientation specimens had higher compressive strength (67 MPa), and crushing load (13 kN) compared to 90º orientation specimens (compressive strength - 54 MPa, crushing

load - 11 kN), which in turn showed higher compressive strength, compared to 45° orientation specimens (compressive strength - 42 MPa, crushing load - 8 kN). It is observed from the quasi-static testing (Fig.7.6 - a, b) that 0° specimens demonstrated 60% and 24% higher compressive strength compared to 45° and 90° specimens respectively.

The 0° orientation specimens exhibited higher Young's modulus (1303 MPa) compared to both 45° orientation specimens (700 MPa) and 90° orientation specimens (650 MPa), which showed similar values. The Young's Modulus of 0° specimens is observed to be 86% and 100% higher than 45° and 90° specimens respectively (Fig.7.6 - c).

The 0° orientation specimens exhibited higher toughness (53 $M.J.m^{-3}$) compared to 90° orientation specimens (29 $M.J.m^{-3}$), and 45° orientation specimens (40 $M.J.m^{-3}$) (Fig. 6- d). The toughness of 0° specimens is observed to be 32.5% and 82.7% higher than that of 45° and 90° specimens respectively.

Experiments showed that 0° orientation specimens exhibited higher standard deviation compared to 90° orientation specimens and 45° orientation specimens for all the mechanical properties considered in this study (Table 7.2). This may be an indicator that failure mechanism in 0° orientation specimens depends on factors which are more sensitive to manufacturing and testing conditions than 90° and 45° orientation specimens.

Thus, the overall effect of orientation on the mechanical properties and energy absorption capability of the PLA material is significant.

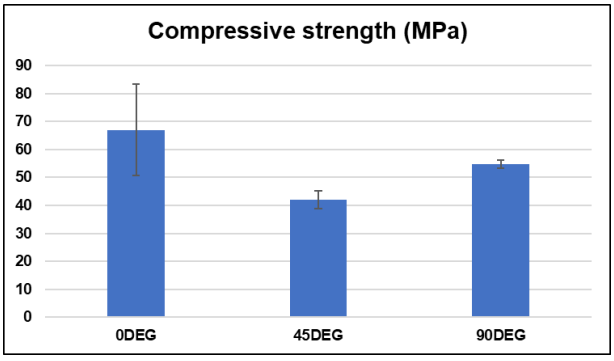

(a)

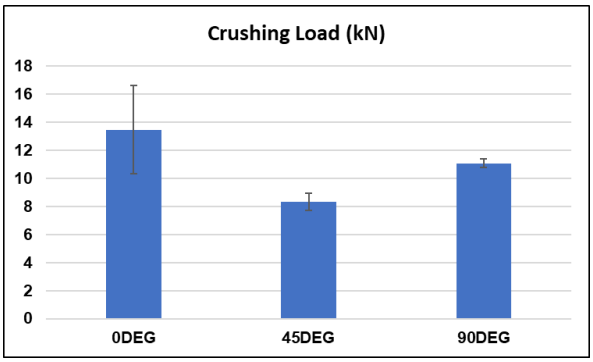

(b)

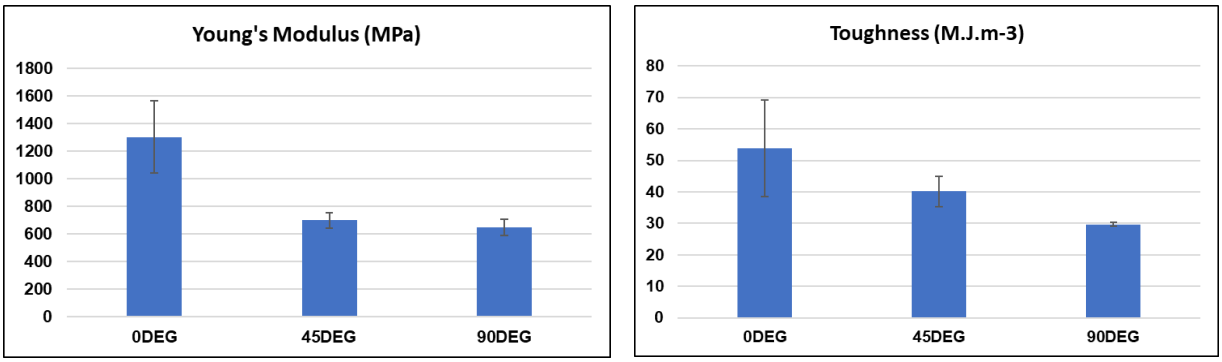

(c) (d)

Figure 7.6: Average value of quasi static (a) compressive strength crushing load, (b) crushing load, (c) Young's modulus and (d) toughness for 0º, 45º and 90º 3D printed disk specimens.

7.5 High strain rate response

Three samples each of specimen orientation (0º, 45º and 90º) are tested for three different strain rates. The average results of high strain rate compression SHPB test on 3D Printed PLA disk specimens with print orientations of 0º, 45º and 90º are presented in Table 7.3. The strain rates of dynamic compressive test ranged between 200 s^{-1} to 1800 s^{-1} for different print orientations. The average stress – strain curves for all specimens computed from Eqns. 7.1 & 7.2, are shown in Fig.7.7.

It is seen from SHPB tests that there is significant effect of orientation on the peak strength (Fig.7.7). Within orientations, the largest variation in peak stress is seen in the specimens with 0º orientation and least variation is observed in the peak stress of specimens with 45º orientation. The maximum compressive strength of 123 MPa is achieved in 0º orientation at a strain rate of 1106/s and the least compressive strength of 56 MPa is achieved in 45º orientation at a strain rate of 626/s.

Table 7.3: Average high strain rate data for 0º, 45º and 90º 3D printed disk specimens.

Orientation	Diameter (mm)	Thickness (mm)	Velocity of striker bar (m/s)	Mean strain rate (s^{-1})	Peak stress (MPa)	Strain corresponding to peak stress (MPa)
0º	15.92	8.08	9.81	200.00	105.61	0.04
	15.92	8.08	14.93	771.33	118.56	0.05
	15.93	8.08	19.46	1106.53	123.10	0.07
45º	15.87	8.03	9.63	626.61	55.95	0.04
	15.87	8.02	15.37	1334.36	59.25	0.04
	15.90	8.06	18.88	1749.47	63.66	0.05
90º	16.10	8.09	9.36	200.00	90.82	0.07
	15.75	7.96	15.25	1222.1	64.41	0.05
	16.23	8.06	19.11	1127.9	117.70	0.09

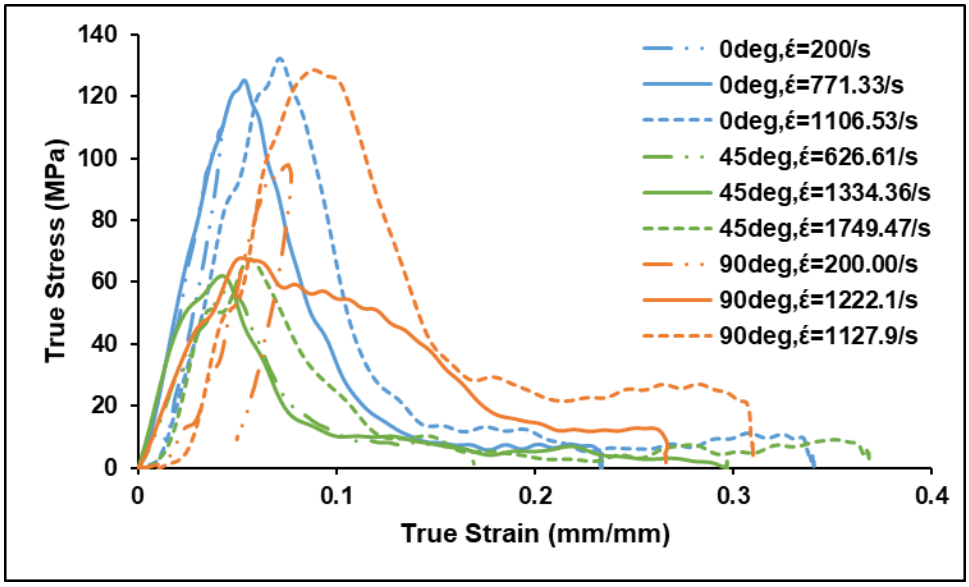

Figure 7.7: Average high strain rate experimental response for 3D printed specimens of 0º, 45ºand 90º orientations

At low strain rates of loading (~200/s), rate dependent increase on the strength of the material is observed (Fig.7.7). However, at low rates, the loading is not sufficient to reach the failure stress of the specimen and hence elastic unloading is observed in 0º and 90º

orientations. This is because the striker is not sufficiently long, causing the applied total strain to be low.

At moderate strain rates (~600/s to 1300/s) the strength increase due to rate effects is significantly apparent for all print orientations (0^o, 45^o and 90^o). Softening behaviour indicated failure in the material. This behaviour is distinct from the compressive behaviour observed in the quasi-static loading regime (10^{-3}/s). The material showed transition from typical polymer or foam like behaviour with a plateau and subsequent densification under quasi-static loading to a quasi-brittle behaviour with post-peak softening under high strain rate loading (Fig. 7.5 & 7.7). This may be due to complex interactions between the effects of porous mesoscale structure, shear failure at interface of the fused filaments (as indicated by the relatively lower compressive strength response of the 45^o oriented PLA), as well as eventual localized buckling failure of filaments.

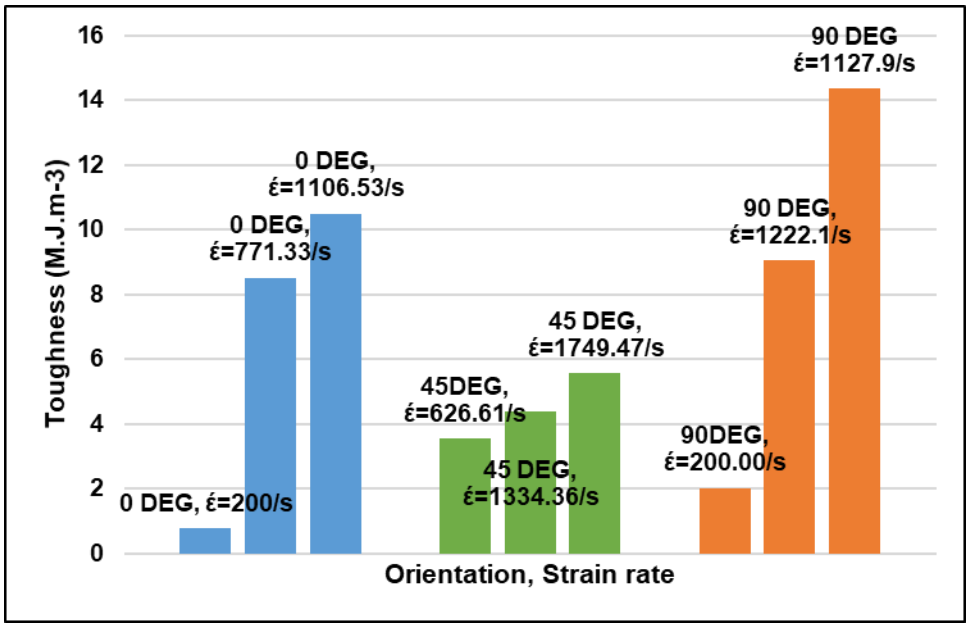

Figure 7.8: Average value high strain rate response of toughness for 0^o, 45^o and 90^o 3D printed disk specimens.

Fig.7.8 shows the average toughness vs strain rates for different orientations at various strain rates for 3D printed PLA. The raster/print orientation had significant effects on static as well as high strain rate responses. In the case of high strain rate response, a higher peak stress and lower strain at breaking failure is seen, compared to the corresponding quasi-static response. Therefore, high strain material response exhibited lower toughness compared to the corresponding static response. In general, for increasing strain rate, corresponding increase in toughness occurs at 0^o, 45^o & 90^o orientations.

7.6 Modified Johnson-Cook Model for 3D printed PLA disk specimens

To describe the flow stress (strength) of 3D printed PLA under dynamic loading, an appropriate constitutive model is required. Several constitutive models have been presented in the literature to characterize flow stresses, and these models may be generally classified as empirical, physical, and artificial neural network based. To characterize the flow response of various materials, empirical (e.g., Johnson–Cook model) and physically-based (e.g., Mechanical- threshold Stress model) constitutive equations are used (Lin and Chen 2010a). The Johnson–Cook (JC) model is an empirical model that has been successfully applied to describe and forecast material flow behaviour of a wide range of materials for various deformation ranges, strain rates, and temperatures (Tan et al. 2015).

The Johnson-Cook (JC) model is assumed to characterize the inelastic behaviour of the studied polymer (PLA). This material model is well suited for modelling the response of viscoplastic materials at high strain rate loading. It is commonly employed in adiabatic transient dynamic analysis. To predict the flow behaviour of materials, it is used as it is simple in form and little effort is needed to estimate the material constants. The JC model considers isotropic hardening in which the flow stress takes the following form (Dorogoy and Rittel 2009) :

$$\sigma = (A + B(\varepsilon^p)^n)\left(1 + Cln\left(\frac{\dot{\varepsilon}^p}{\dot{\varepsilon}_0}\right)\right)(1 - \hat{T}^m) \tag{7.3}$$

In the above equation, ε^p is the equivalent plastic strain & *A, B, C, n* and *m* are material parameters to be specified. "*ln*" represents natural logarithm. In equation (7.3), *T* is a dimensionless parameter representing the current temperature, T_m & T_r being the melting temperature and the reference temperature respectively and *A* represents yield stress σ_Y at temperatures under T_r. *C* and $\dot{\varepsilon}_0$ are measured generally at or below the reference temperature. Reference strain rate $\dot{\varepsilon}_0 = 1$.

The value of A is determined from the quasi-static yield stress at reference strain rate using experimental quasi-static stress-strain data. The JC parameters *B, n* and *C* are computed using GRG nonlinear (Excel®) solver for curve fitting (Table 7.4).

Table 7.4: JC parameters determined for various orientations of 3D printed PLA.

Print orientation	*A* (MPa)	*B* (MPa)	*n*	*C*
0º	67	-78.392	0.091	0.669
45º	42.01	-55.670	0.176	0.170
90º	54.77	-65.293	0.161	0.585

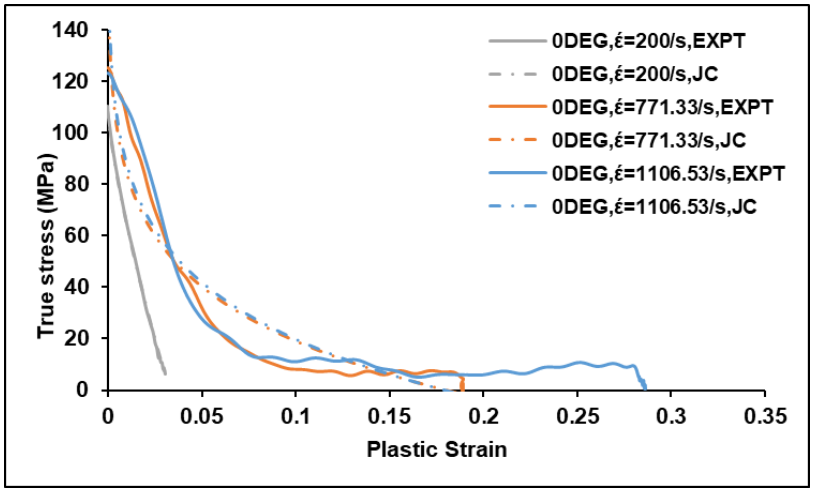

(a)

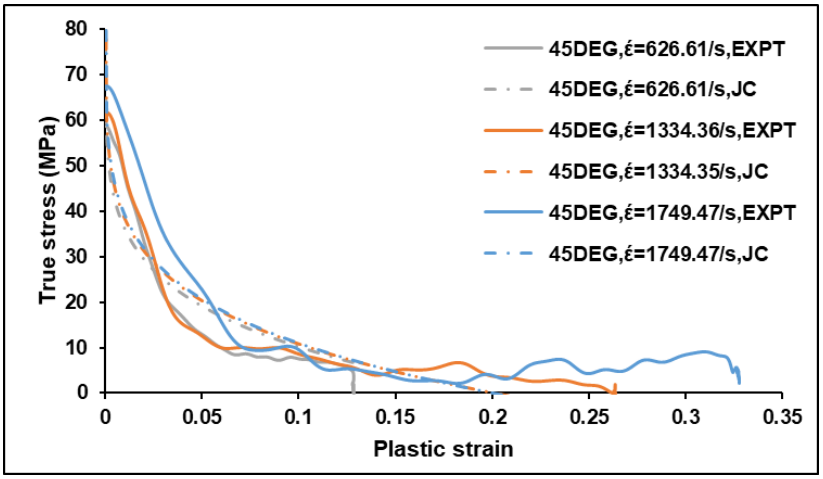

(b)

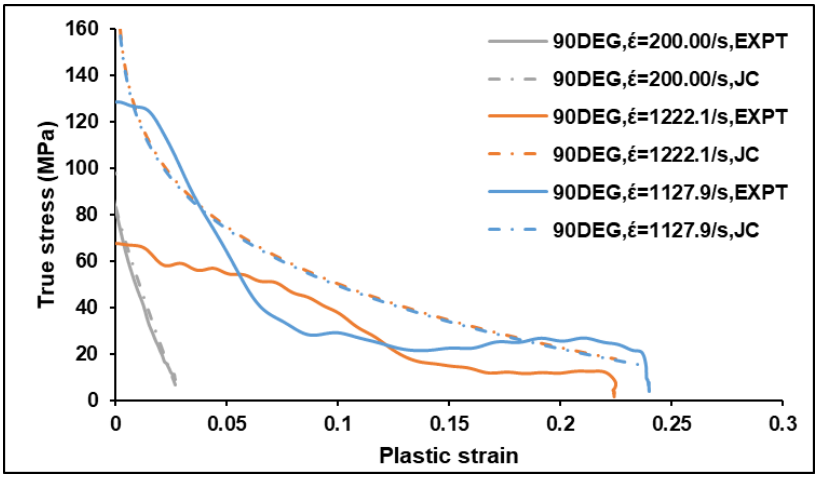

(c)

Figure 7.9: (a), (b) & (c) Compression plastic true stress-strain curves at various strain rates between experiment and JC curve fit data.

The strain softening quasi-brittle behaviour in the high strain rate loading regime is adequately captured by fitting the JC model to experimental data obtained for various orientations (Fig.7.9 - a,b,c).

Several effects are required to be combined within a porosity-based strength evolution (flow stress) model, for additively manufactured PLA material, in order to capture the observed strain softening and rate dependent response:

i. Size of filament (**s**): Scale effects, porosity and the reliability of the filaments depend on the diameter and length of the filaments (Priyanka et al. 2021).
ii. Print orientation (***θ***) – orientation with respect to loading axis
iii. Print density (***ρ***)- Overlap between filaments (Priyanka et al. 2021).
iv. Strain rate (***ε̇***) dependence
v. Temperature dependence -Ambient temperature, manufacturing temperatures

Li Li and Michel Aubertin (Li Li and Aubertin 2003) proposed an equation for determining the relation between strength and porosity (Fig. 7.10) which incorporates a generalized form of power law as well as the Ryshkewitch & Duckworth (1953) (Ryshkewitch, n.d.) law in it:

$$\sigma_{tn} = \sigma_0 \left(1 - sin\left(\frac{\pi}{2}\frac{n}{n_{ct}}\right)^{x_1}\right) \tag{7.4}$$

Where, 'σ_{tn}' is the material's uniaxial tensile strength with a porosity 'n' and 'n_{ct}' is critical porosity (max. porosity), where $x = 4$ for 0^o.

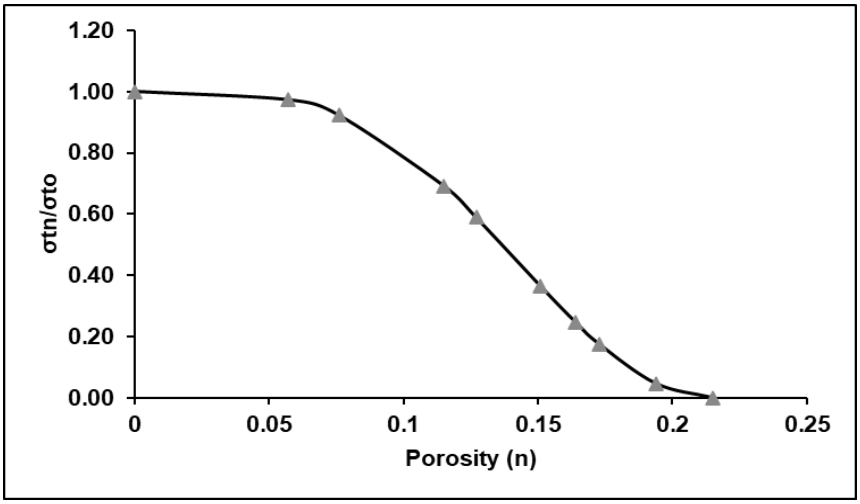

Figure 7.10: Effect of porosity on strength.

For prediction of the effect of orientation on strength, a simple quadratic relationship is proposed, based on curve-fitting to the experimental data obtained from static compressive testing detailed previously in Fig.7.6, this may be adequate for predicting compressive strength at various print orientations (Fig. 7.11):

$$\sigma_{or} = (\sigma_0 + ax + bx^2) \tag{7.5}$$

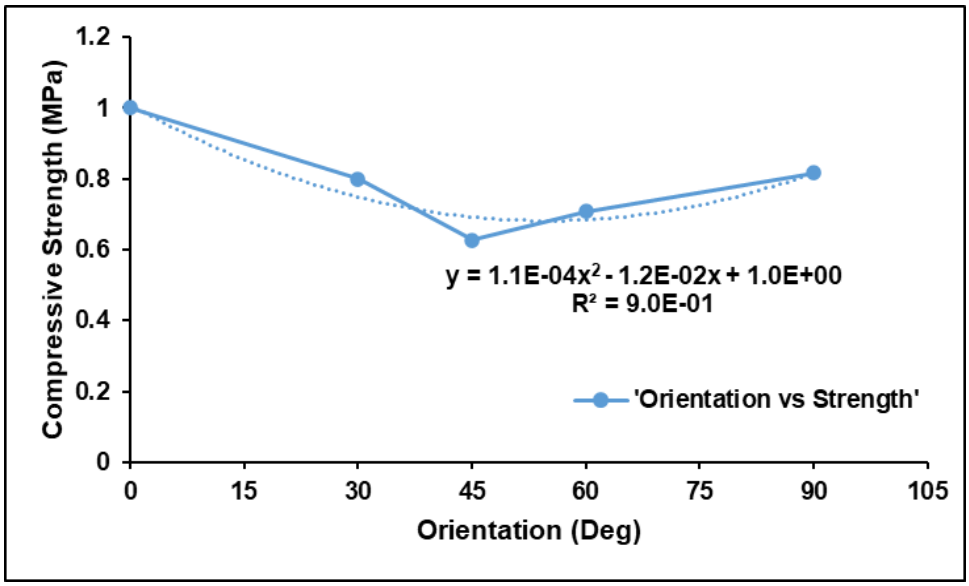

Figure 7.11: Effect of print orientation on the compressive strength of PLA disk specimens

While print orientation and porosity might be correlated to a certain extent in 3D printed materials, their effects are treated independently in the proposed model (Eqns. 7.4,7.5 & Fig. 7.10,7.11) prior to combination (Fig. 7.12). The effects of temperature,

filament diameter and length on high strain rate response are not included in the present study.

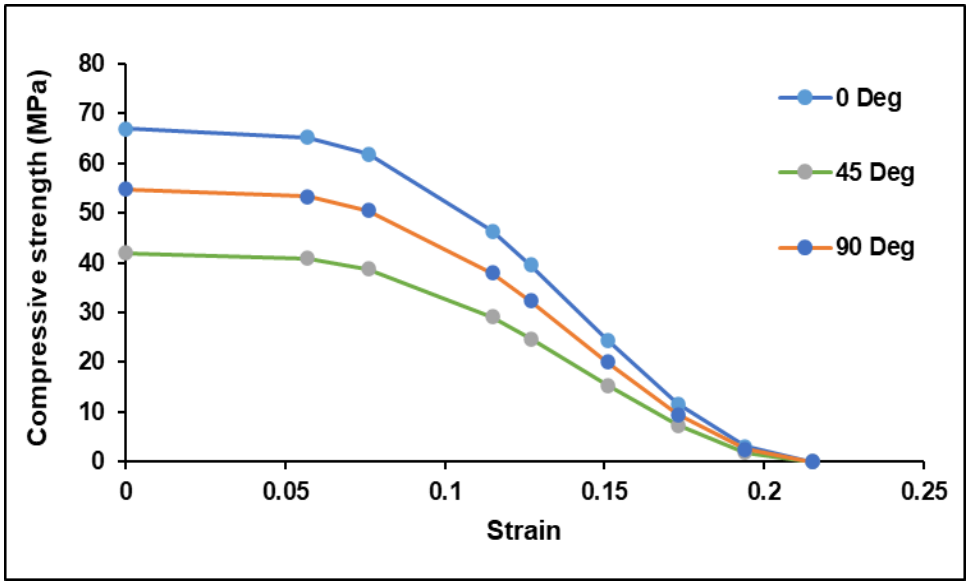

Figure 7.12: Combined effect of print orientation and porosity on the static compressive strength

Hence, a simple modification of the Johnson-cook model is proposed, which accounts for the aforementioned factors, i.e., print orientation and porosity (Fig. 7.12) as well as strain rate effects (Eqn. 3) in additively manufactured materials:

$$\sigma = (\sigma_0 + ax + bx^2)\,(1 - sin(\frac{\pi}{2}\frac{n}{n_{ct}})^x)(A + B(\varepsilon^p)^n)\left(1 + C\,ln\left(\frac{\dot{\varepsilon}^p}{\dot{\varepsilon}_0}\right)\right)(1 - \hat{T}^m) \qquad (7.7)$$

In the above modified JC equation, the effects of print orientation and porosity are included as pre-multiplicative factors (Eqn. 7.7). The values of these two factors, which may correspond to various unique print orientations and porosities, are multiplied with baseline JC equation corresponding to 0^o print orientation (orientation factor = 1.0) and 100% infill density (porosity factor = 1.0) of the additively manufactured material. This simple relationship enables response prediction for various print orientations, based on the modification of 0^o (baseline) response data.

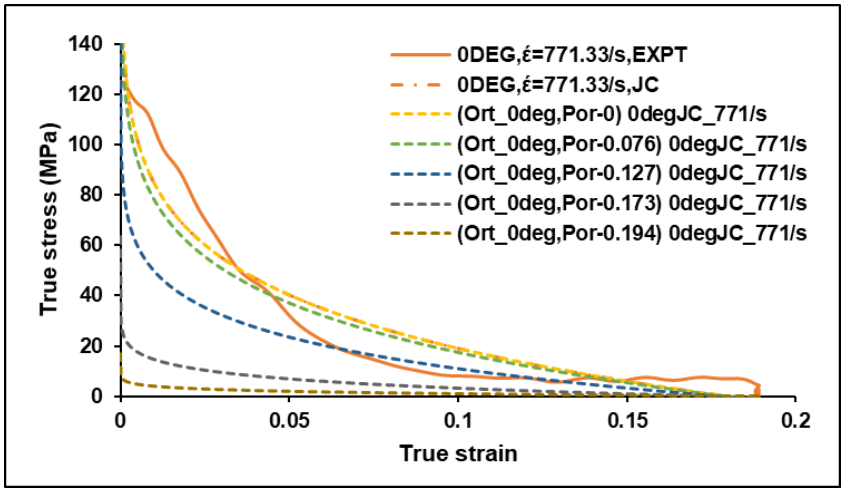
True stress (MPa)
True strain
0DEG,ε=771.33/s,EXPT
0DEG,ε=771.33/s,JC
(Ort_0deg,Por-0) 0degJC_771/s
(Ort_0deg,Por-0.076) 0degJC_771/s
(Ort_0deg,Por-0.127) 0degJC_771/s
(Ort_0deg,Por-0.173) 0degJC_771/s
(Ort_0deg,Por-0.194) 0degJC_771/s

(a)

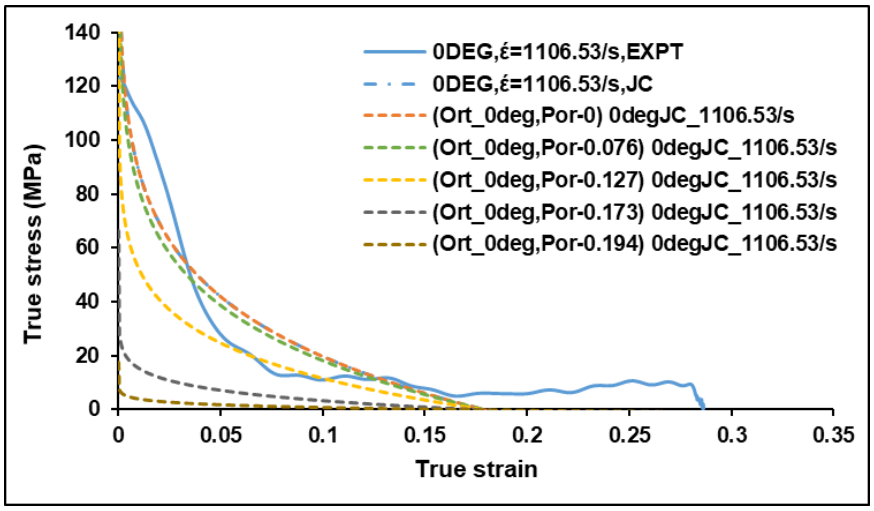
True stress (MPa)
True strain
0DEG,ε=1106.53/s,EXPT
0DEG,ε=1106.53/s,JC
(Ort_0deg,Por-0) 0degJC_1106.53/s
(Ort_0deg,Por-0.076) 0degJC_1106.53/s
(Ort_0deg,Por-0.127) 0degJC_1106.53/s
(Ort_0deg,Por-0.173) 0degJC_1106.53/s
(Ort_0deg,Por-0.194) 0degJC_1106.53/s

(b)

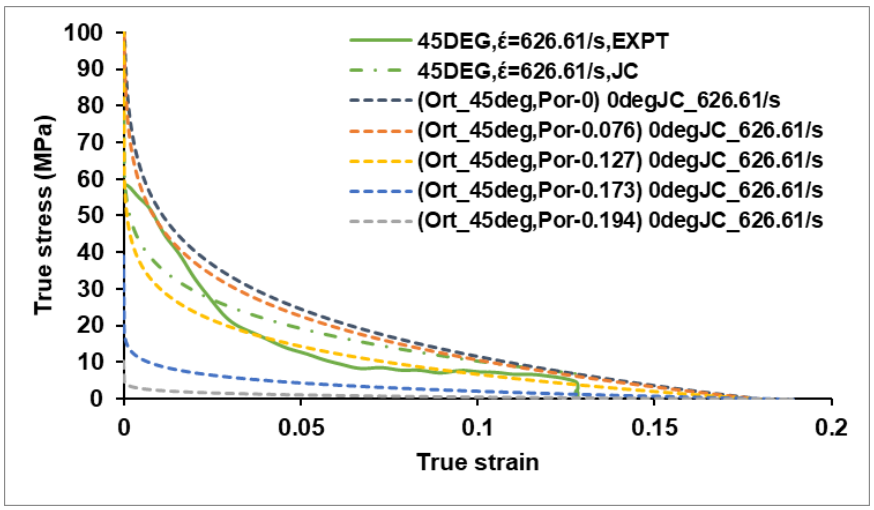
True stress (MPa)
True strain
45DEG,ε=626.61/s,EXPT
45DEG,ε=626.61/s,JC
(Ort_45deg,Por-0) 0degJC_626.61/s
(Ort_45deg,Por-0.076) 0degJC_626.61/s
(Ort_45deg,Por-0.127) 0degJC_626.61/s
(Ort_45deg,Por-0.173) 0degJC_626.61/s
(Ort_45deg,Por-0.194) 0degJC_626.61/s

(c)

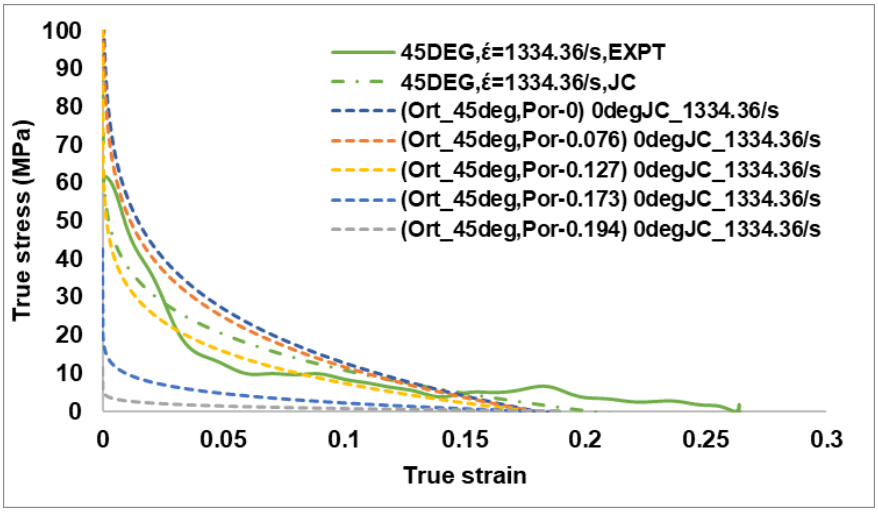
True stress (MPa)
True strain
45DEG,ε=1334.36/s,EXPT
45DEG,ε=1334.36/s,JC
(Ort_45deg,Por-0) 0degJC_1334.36/s
(Ort_45deg,Por-0.076) 0degJC_1334.36/s
(Ort_45deg,Por-0.127) 0degJC_1334.36/s
(Ort_45deg,Por-0.173) 0degJC_1334.36/s
(Ort_45deg,Por-0.194) 0degJC_1334.36/s

(d)

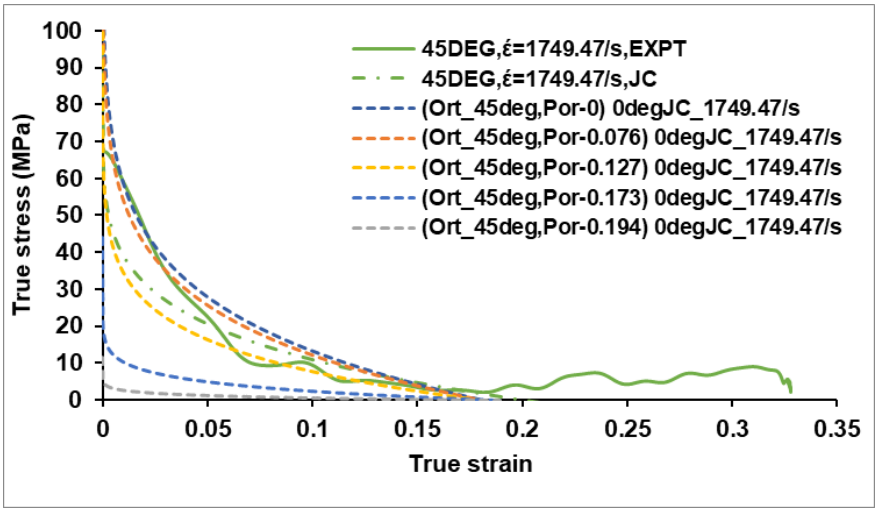
True stress (MPa)
True strain
45DEG,ε=1749.47/s,EXPT
45DEG,ε=1749.47/s,JC
(Ort_45deg,Por-0) 0degJC_1749.47/s
(Ort_45deg,Por-0.076) 0degJC_1749.47/s
(Ort_45deg,Por-0.127) 0degJC_1749.47/s
(Ort_45deg,Por-0.173) 0degJC_1749.47/s
(Ort_45deg,Por-0.194) 0degJC_1749.47/s

(e)

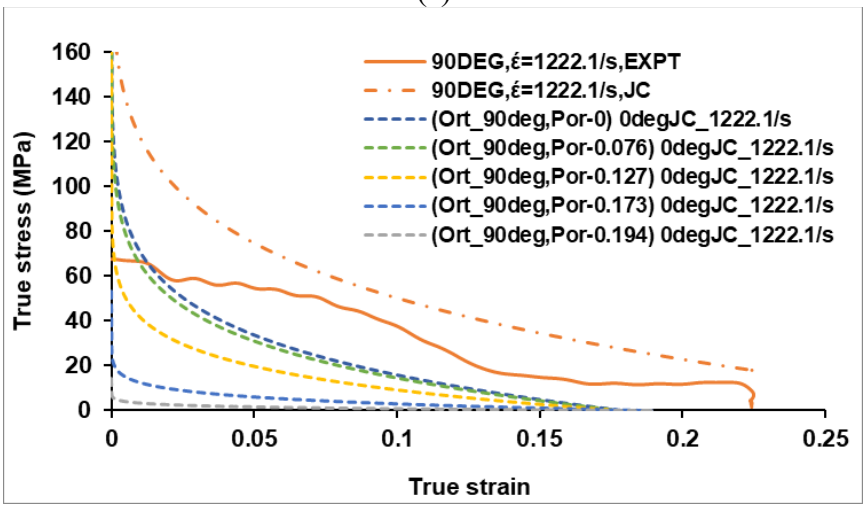
True stress (MPa)
True strain
90DEG,ε=1222.1/s,EXPT
90DEG,ε=1222.1/s,JC
(Ort_90deg,Por-0) 0degJC_1222.1/s
(Ort_90deg,Por-0.076) 0degJC_1222.1/s
(Ort_90deg,Por-0.127) 0degJC_1222.1/s
(Ort_90deg,Por-0.173) 0degJC_1222.1/s
(Ort_90deg,Por-0.194) 0degJC_1222.1/s

(f)

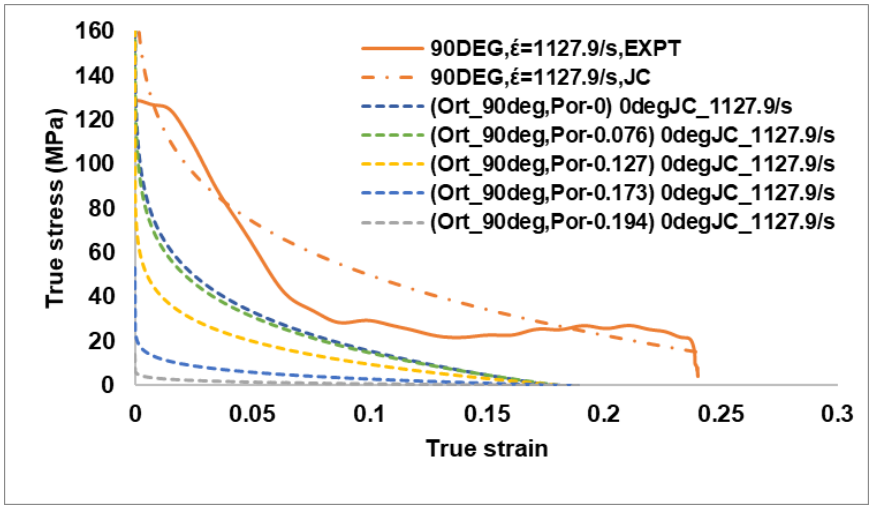

(g)

Figure 7.13 (a-g): Combined effect of print orientation and porosity on the high strain rate response.

The JC model, with baseline parameters determined from SHPB experiments for the PLA material printed at 0^o orientation and 100% infill, is multiplied by the strength modification factors which account for orientation and porosity, as detailed in equation 7. Figures 7.13 (a-g) shows comparison between- i) SHPB experimental data for each orientation, ii) prediction by JC model fitted to experimental data of each orientation and iii) predictions for various porosities by modified JC model (baseline 0^o orientation and 100% infill JC model, which is multiplied by factors for orientation and infill density).

The results indicate that for 100% infill, the experimental responses for 45^o orientation and 90^o orientation lie between the corresponding JC models fitted to experiments and modified JC models. In case of 45^o orientation, the JC model corresponding to experimental data of 45^o orientation is lower bound and the modified JC model is upper bound for various strain rates. In the case of 90^o orientation, the JC model corresponding to experimental data of 90^o orientation is upper bound and the modified JC model is lower bound.

The dynamic strength increase factors for various print orientations of PLA are extracted from SHPB experimental results detailed in Figure 14. For strain rates of the order of 10^2-10^3/sec, strength increase factors of: 2.0-2.15 for 0^o orientation; 1.3 to 1.5 for 45^o orientation; and 1.4 - 2.5 for 90^o orientation, are indicated. A greater sensitivity to strain rate is observed in the case of 90^o orientations as compared to 0^o and 45^o orientations.

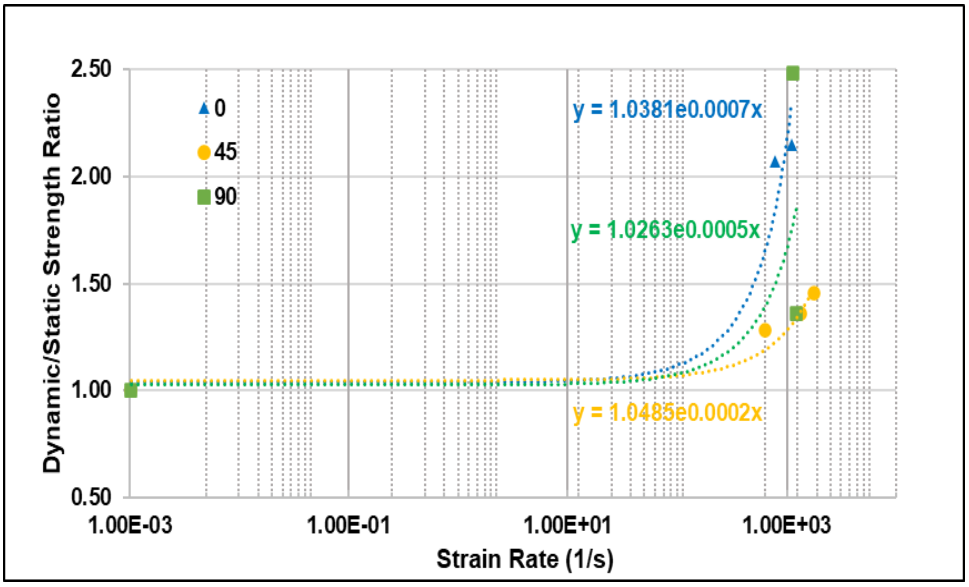

Figure 7.14: Dynamic strength increase factors for various print orientations of PLA.

7.7 Conclusion

High strain rate response of 3D printed PLA has been characterized for 0º, 45º and 90º print orientations and is found to be significantly more brittle compared to the corresponding quasi-static response. The mechanical response of PLA is observed in the transition from typical polymer/foam type hardening and densification behaviour in the quasi-static loading regime to quasi-brittle and strain softening behaviour in the high strain rate loading regime. In this study, the dynamic increase factors for various orientations of PLA are reported and strain rate sensitivity is quantified. A simple modification of the JC model is proposed for predicting the strain rate based on flow stress of 3D printed PLA, which includes the decoupled effects of strain softening, print orientation and porosity. The model under predicts the strength for 45º orientation and over predicts the same for 90º oriented PLA. While the relatively low strength PLA is used as a model material in this study, the methodology developed in this study can be adopted for high strain rate response characterization of other viscoelastic/viscoplastic AM materials with superior engineering properties suitable for aerospace, automotive and defence applications.

CHAPTER 8

Dynamic Mechanical Analysis of Additively Manufactured Polylactide (PLA)

8 Dynamic mechanical analysis of AM Polylactic acid (PLA) (Phase – V)

To characterize the dynamic mechanical analysis of 3D printed PLA at 0^o, 30^o, 45^o and 90^o orientations is to determine viscoelastic properties such as elastic (storage) modulus, loss (viscous) modulus and tan delta as a function of frequency, temperature are significant transitions in visco-elastic behaviour.

8.1 DMA test on 3D Printed PLA Rectangular specimens

The dynamic mechanical analysis (DMA) is conducted for 3D printed PLA specimens, produced in different orientations (i.e., 0°, 30^o, 45° and 90°) with the FDM technique implemented on an Ultimaker^{2+} 3D printer. The reference standard for the determination of the dynamic mechanical properties of plastic materials is "ASTM D5023-07 Standard Test Method Plastics: Dynamics Mechanical Properties: In Flexure (Three-Point Bending)" ("Designation: D5023 − 07 StandardTest Method for Plastics: Dynamic Mechanical Properties: In Flexure (Three-Point Bending) 1," n.d.).

The purpose of DMA is to determine the viscoelastic properties such as elastic (storage) modulus, loss (viscous) modulus, and tan delta as a function of frequency and temperature, which are indicative of significant transitions in the thermomechanical behaviour of polymers. The principle of time-temperature equivalence; i.e, the mechanical response at low temperature is equivalent to a response at short times and the response at high temperature is equivalent to response at long times Ferry (1980). As the frequency is increased, the time allowed for molecular motion in a given cycle decreases. Thus, the frequency may be regarded as inverse time, consistent with the units of the frequency. Rather than performing a DMA scan in temperature at a constant frequency, a DMA scan can be performed in frequency at a constant temperature.

A rectangular specimen suitable for the flexural mode of testing has been chosen for the study of visco-elastic behaviour.

8.1.1 Materials and specimen fabrication

In this study, poly-lactic acid (PLA) is used to produce samples in an Ultimaker^{2+} 3D printer. The specimens and dimensions for specimen types are shown in Fig.8.1. The rectangular specimen is first created in Creo, exported in stereolithography (STL) format, and then imported into each 3D printer's respective slicer (Cura) software to create the G-code used to print each specimen type.

The layer height, extrusion width, air gap (the space between the bead of material), printing temperature (the temperature of the air around the part and the bed temperature), build plate temperature, nozzle size (width of the hole through which the material is extruded), and colour, print speed, and infill density are all held to constant values. The entire list of constant or default values used during this study is shown in Table 8.1. Like tensile specimens, for investigation of properties of prism specimens, the orientation selected are 0°, 30^o, 45° and 90°. The specimens are printed in the 0°, 30^o, 45° and 90° directions as shown in Fig.8.1. Four identical specimens are printed for each orientation and the results for all four tests are averaged to find the properties in each direction.

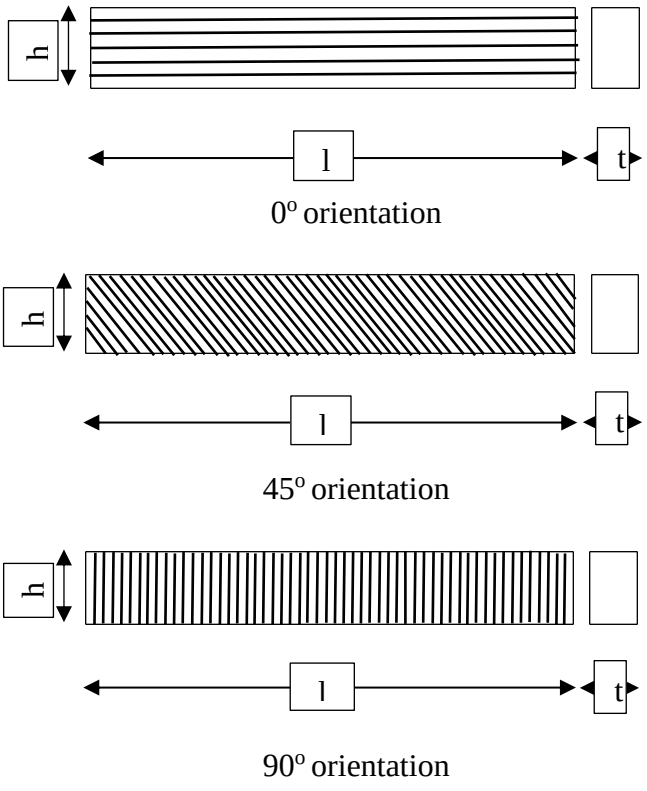

Figure 8.1: Schematic representation of the ASTM D5023-07 rectangular specimen geometry with relevant dimensions in mm. Rectangular specimen for DMA testing with dimensions and orientations.

Table 8.1: Constant 3D-printing process settings for the Ultimaker^{2+} printer

Parameter	Ultimaker^{2+} PLA value
Air gap (mm)	0.0
Layer height (mm)	0.1
Extrusion width (mm)	0.35
Nozzle size (mm)	0.4
Filament color	White
Infill Density (%)	100
Wall thickness (mm)	0.1
Printing Temperature (°C)	200
Build plate temperature (°C)	60
Print speed (mm/s)	50

8.1.2 Testing machine and experimental set-up

The Dynamic mechanical properties of rectangular samples are 64mm x13mm x 3mm tested under 3-point bending mode (Fig.8.2) in the Metravib, DMA25 equipment (Table 8.2). Before starting the experiment, the dimensions of each specimen are measured to the nearest 0.01 mm at several points along its length using a digital vernier caliper and the mean value is recorded. Two types of tests are conducted on the specimens- i) Varying temperature and frequencies, ii) Varying frequency. Test one is temperature scanning with multi–frequency (1Hz, 3Hz, and 5Hz), and test two is conducted at ambient temperature with a frequency range from 1-200 Hz. Both tests are performed under a static force of 3N and a dynamic force of 1N (optimized by trial and error method).

The frequency, temperature, corresponding tan delta, storage modulus and loss modulus are acquired, computed and stored automatically. The DMA results obtained from the experiments are shown in Fig. 8.3 in the next section.

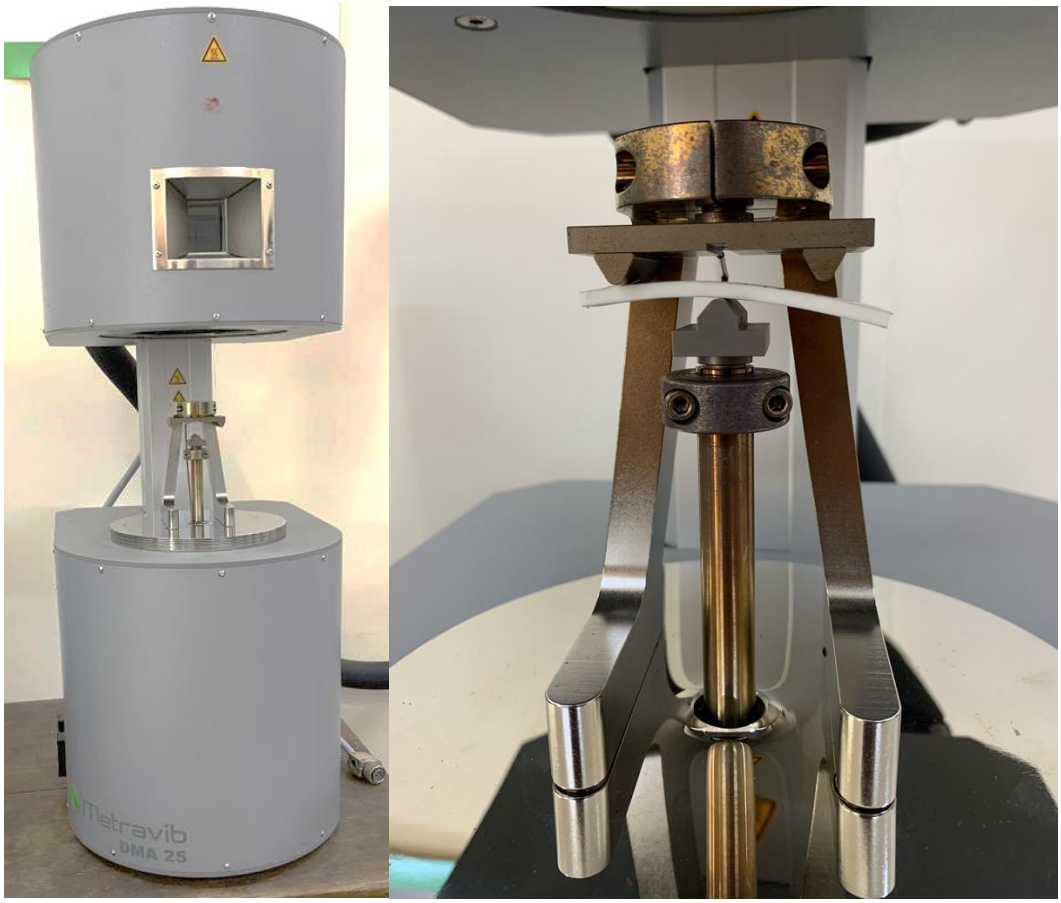

Figure 8.2: Experimental set-up for DMA testing

Table 8.2: Specifications of DMA equipment Metravib, DMA25

		DMA 25
Temperature		-150/500 ^{O}C
Frequency		DC-200Hz
Dynamic	Peak Force	25N
	Peak Displacement	3 mm
Static	Force	25N
	Displacement	6 mm

8.2 Dynamic Mechanical Properties: In Flexure (Three-Point Bending)

Dynamic mechanical analysis is crucial for determining the dynamic parameters of polymers under cyclic external forces. Dynamic parameters such as storage modulus E', loss modulus E" and loss factor tanδ are temperature dependent and have the following relationship:

$$\tan\delta = \frac{E''}{E'} \quad \textbf{(8.1)}$$

The storage modulus E' refers to the elastic behaviour which relates to solid-like nature of PLA, and loss modulus E" to the viscous behaviour which relates to liquid-like behaviour. The elastic moduli, loss moduli, and tan delta of the PLA material are measured. The specimen rests on one support which has dynamic action and is loaded at two points at *l*/3 distance on either side of the specimen. The upper part of the fixture is in static action.

8.3 Results and Discussion

Test 1: *Temperature scanning with multi-frequency*

A 0^o-oriented 3D printed PLA specimen is considered for analyzing the behavior of polymer subjected to temperature screening with multi-frequency (1Hz, 3Hz, and 5Hz). From Fig.8.3, it is observed that the glass transition stage of PLA is at 62 ^oC. The storage modulus (E') decreases with increase in frequency. Two identical specimens are printed for each orientation and the results for all ten tests averaged to find the properties in each direction.

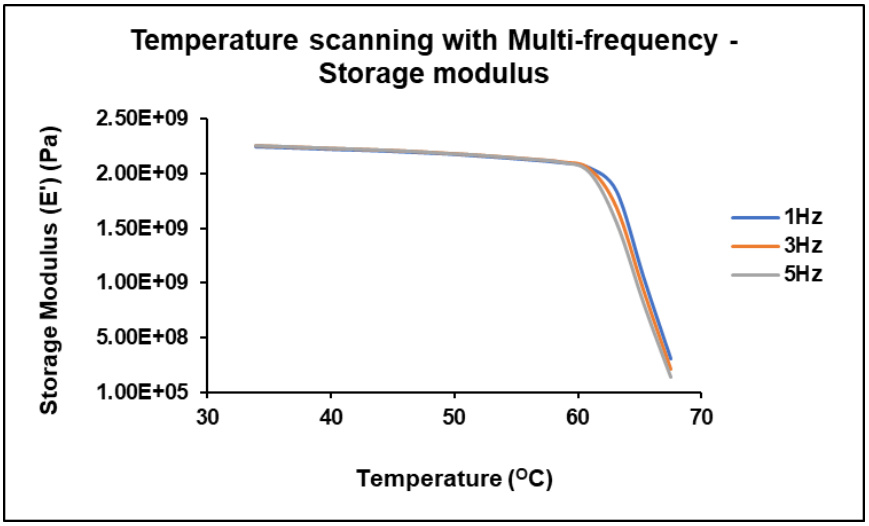

(a)

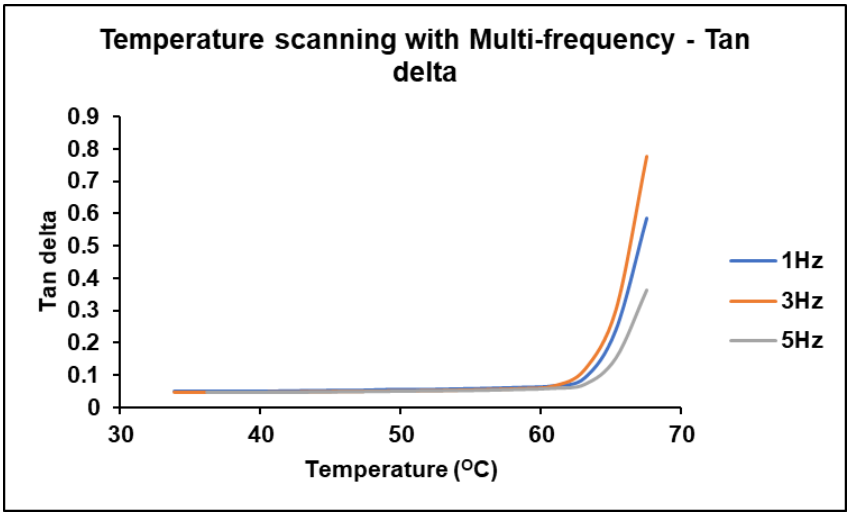

(b)

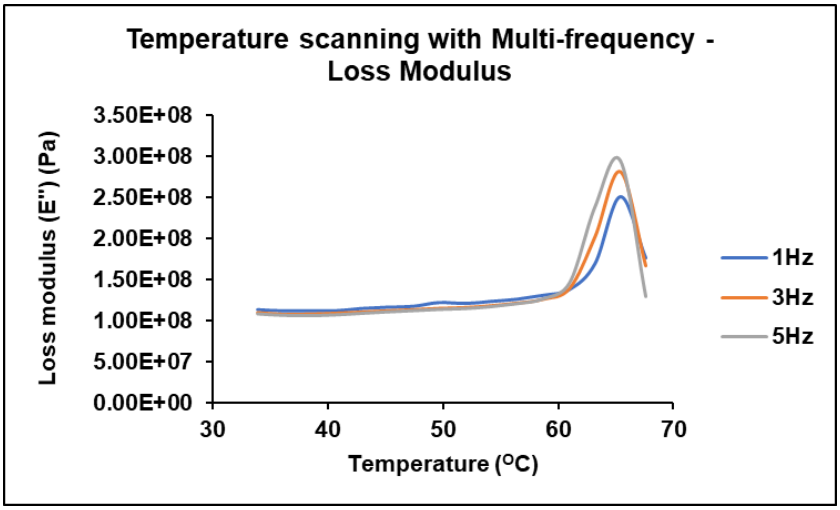

(c)

Figure 8.3: Temperature scanning vs (a) storage modulus, (b) tan delta, (c) loss modulus of 3D printed PLA for 0° orientations.

Test 2: *Frequency scanning with ambient temperature*

The frequency vs tan delta, storage modulus, and loss modulus results of DMA test on 3D printed rectangular specimens of each 64 mm x 13 mm x 3 mm are respectively shown in Fig. 8.4. Four identical specimens are printed for each orientation and the results for all ten tests averaged to find the properties in each direction.

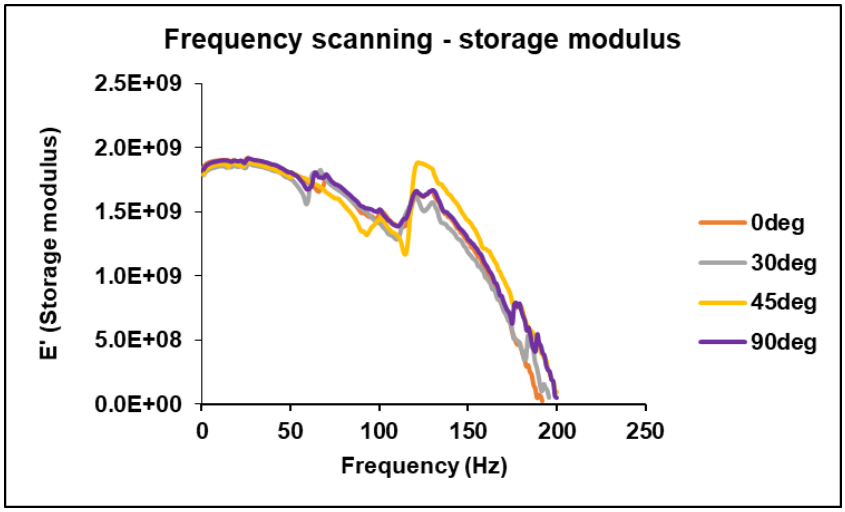

(a)

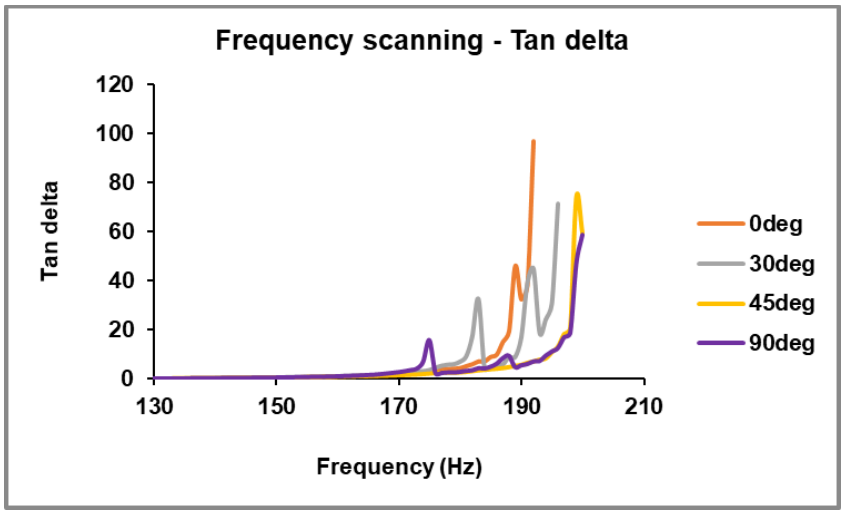

(b)

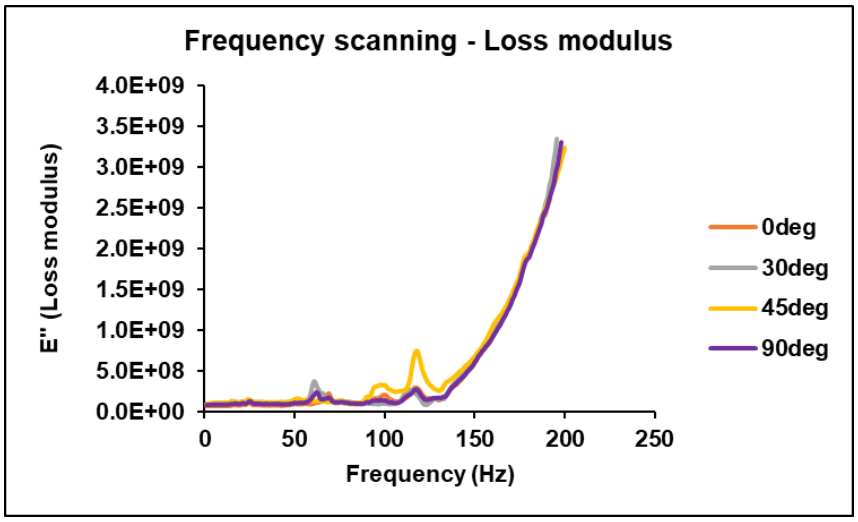

(c)

Figure 8.4: Frequency vs (a) storage modulus, (b) tan delta, (c) loss modulus of 3D printed PLA for 0°, 30º, 45°, and 90° orientations.

Test 2 shows that storage modulus decreases with increasing frequency when the temperature is ambient (Fig. 8.4a). This trend is consistent with the observations in Test-1.

8.4 Discussion & Conclusions:

Several DMA studies, have been conducted by researchers mostly in temperature scanning mode, on solid (cast) ABS and PLA specimens. The results of these studies indicate that solid (cast) ABS and PLA follow the typical trends established for most polymers. In general, the storage modulus (E') of polymers typically increases with frequency (Pramanik and Mantena 2011; Coppola et al. 2018).

However, to the author's knowledge, there is a dearth of published literature on DMA testing of 3D printed materials. DMA testing of 3D printed ABS and PLA with temperature scanning was conducted (Pramanik and Mantena 2011; Coppola et al. 2018). Their study confirmed that 3D-printed ABS behaves similar to solid (cast) polymer specimens.

In this study, the storage modulus (E') for 3D printed PLA specimens of various print orientations, is tested in the range of 0.4 GPa to 2.2 GPa for the frequency interval of 1Hz – 200Hz. It is observed that with the increase in frequency, storage modulus (E') of PLA tends to decrease and the loss modulus (E'') increases, *which is contrary to behavior typically seen in solid (cast) polymers* (Fig. 8.4a). The same trend is also observed in the independently conducted temperature scanning (ambient to 70^{o}C) with varying frequencies (1Hz, 3Hz, and 5Hz), wherein the higher frequency (5Hz) indicates lower modulus (Fig. 8.3a). However, the overall trend of variation of E' with respect to temperature is observed to be the same as typically seen in the literature.

An independent study on UHMWPE polymer using the same equipment and procedures shows the trends consistent with established literature (Fig 8.5a). This lends confidence on the equipment and testing procedure.

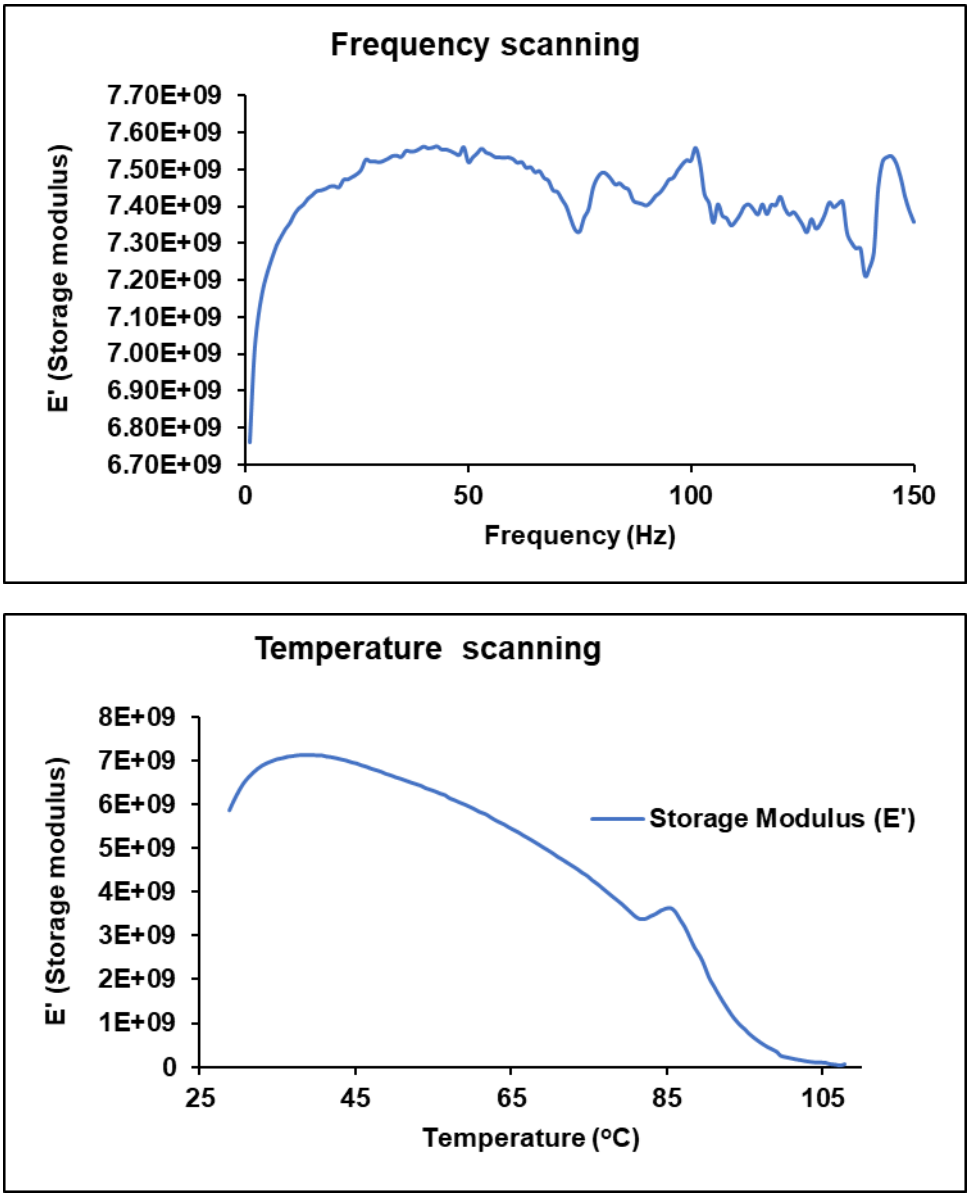

Figure 0.1: UHMWPE: Storage modulus vs (a) Frequency scanning (b) Temperature scanning

It is hypothesized that the reverse trend observed at higher frequencies in the E' vs frequency scan might be due to mesoscale effects such as porosity, and flow of material at interfaces between strands, leading to reduction of internal shear resistance, which, in solid specimens usually occurs at low frequencies. Although further detailed study of this phenomena is warranted, it is beyond the scope of the current work.

Future work:

1. The data obtained from reliability study of filaments can be further used for analytical and numerical material constitutive modelling of 3D printed Poly lactic Acid (PLA) parts which can then be directly related to any structural shape with various deposition orientations and layups.
2. Ab-initio modelling of failure criteria from high fidelity micro and meso structure based representative volume elements (RVE) using XFEM. This model simulates fracture at the overlapping interfaces between the individual strands. The material damage is simulated using the damage plasticity option along with X-FEM based displacement-initiated fracture. This will enable prediction of stiffness and strength of 3D printed parts as a function of porosity based on micromechanics and RVE based material constitutive model for 3D printed PLA materials subjected to quasi-static tensile loading.
3. The effects of temperature, filament diameter and length on high strain rate response can be studied.
4. Conduct DMA for solid cast and 3D printed PLA specimens, produced in different orientations (i.e., 0°, 30o, 45° and 90°). The principle of time-temperature equivalence can be applied to analyze high strain rate behavior. Develop visco-elastic lumped parameter models that can explain the anomalous mechanical response at high frequencies.

Publications:

Journal Papers

1) **GTL Priyanka,** Kamlesh Kumar, V.GuruPrathap Reddy, T.Tadepalli, Mechanical Reliability of Extruded PLA Filaments, Materialia, Vol. 16, May 2021, 101075. https://doi.org/10.1016/j.mtla.2021.101075 (Scopus Indexed).
2) **GTL Priyanka,** Saideep Chilukuri, T.Tadepalli, Dynamic Characterization of Additively Manufactured Polylactide (PLA)**,** *Proceedings of the Institution of Mechanical Engineers, Part L: Journal of Materials: Design and Applications, 236*(5), 963–976. (I.F:2.311) https://doi.org/10.1177%2F14644207211065149 (SCIE, SCOPUS Indexed).

Conference Papers:

1) **G.T.L Priyanka**, Navaneet N. Kabra, and Dr. T.P.Tezeswi, ***Mechanical Characterization Of 3D Printed PLA Strands***, International Conference on Recent Advances in Materials, Mechanical and Civil Engineering (ICRAMMCE-2017)
2) **G.T.L Priyanka**, K.Kumar and T.P.Tezeswi, ***3D Printing Issues & Challenges: A Review***, International Conference on Advanced Functional Materials and Devices, 2019 .

References:

Ahn, Sung Hoon, Michael Montero, Dan Odell, Shad Roundy, and Paul K. Wright. 2002. *Anisotropic Material Properties of Fused Deposition Modeling ABS*. *Rapid Prototyping Journal*. Vol. 8. https://doi.org/10.1108/13552540210441166.

Altıparmak, Sadettin Cem, and Bowen Xiao. 2021. "A Market Assessment of Additive Manufacturing Potential for the Aerospace Industry." *Journal of Manufacturing Processes* 68 (May): 728–38. https://doi.org/10.1016/j.jmapro.2021.05.072.

Arunprasath, K., M. Vijayakumar, M. Ramarao, T. G. Arul, S. Peniel Pauldoss, M. Selwin, B. Radhakrishnan, and V. Manikandan. 2021. "Dynamic Mechanical Analysis Performance of Pure 3D Printed Polylactic Acid (PLA) and Acrylonitrile Butadiene Styrene (ABS)." In *Materials Today: Proceedings*, 50:1559–62. Elsevier Ltd. https://doi.org/10.1016/j.matpr.2021.09.113.

ASTM D695. 2010. "Standard Test Method for Compressive Properties of Rigid Plastics." *ASTM International* i: 1–8. https://doi.org/10.1520/D0695-15.2.

Ayrilmis, Nadir. 2018a. "Effect of Layer Thickness on Surface Properties of 3D Printed Materials Produced from Wood Flour/PLA Filament." *Polymer Testing* 71 (July): 163–66. https://doi.org/10.1016/j.polymertesting.2018.09.009.

———. 2018b. "Effect of Layer Thickness on Surface Properties of 3D Printed Materials Produced from Wood Flour/PLA Filament." *Polymer Testing* 71 (July): 163–66. https://doi.org/10.1016/j.polymertesting.2018.09.009.

Barbero, E, J Fernández-Sáez, and C Navarro. n.d. "Statistical Analysis of the Mechanical Properties of Composite Materials."

Beheshtizadeh, Nima, Nasrin Lotfibakhshaiesh, Zahra Pazhouhnia, Mahdieh Hoseinpour, and Masoud Nafari. 2020. "A Review of 3D Bio-Printing for Bone and Skin Tissue Engineering: A Commercial Approach." *Journal of Materials Science*. Springer. https://doi.org/10.1007/s10853-019-04259-0.

Bellehumeur, Céline, Longmei Li, Qian Sun, and Peihua Gu. 2004. "Modeling of Bond Formation between Polymer Filaments in the Fused Deposition Modeling Process." *Journal of Manufacturing Processes* 6 (2): 170–78. https://doi.org/10.1016/S1526-6125(04)70071-7.

Blok, L. G., M. L. Longana, H. Yu, and B. K.S. Woods. 2018. "An Investigation into 3D Printing of Fibre Reinforced Thermoplastic Composites." *Additive Manufacturing* 22 (August): 176–86. https://doi.org/10.1016/j.addma.2018.04.039.

Brischetto, Salvatore, Carlo Ferro, Paolo Maggiore, and Roberto Torre. 2017. "Compression Tests of ABS Specimens for UAV Components Produced via the FDM Technique." *Technologies* 5 (2): 20. https://doi.org/10.3390/technologies5020020.

Butadiene Styrene, Acrylonitrile. 2007. "CONSTITUTIVE MODELING OF FUSED DEPOSITION MODELING."

Cabrero, J. M., C. Blanco, K. G. Gebremedhin, and A. Martin-Meizoso. 2012. "Assessment of Phenomenological Failure Criteria for Wood." *European Journal of Wood and Wood Products* 70 (6): 871–82. https://doi.org/10.1007/s00107-012-0638-3.

Campbell, Ian, and Ian Gibson. 2012. "Version of the Item Published as : Available from Deakin Research Online : Additive Manufacturing : Rapid Prototyping Comes of Age."

Cantrell, Jason T., Sean Rohde, David Damiani, Rishi Gurnani, Luke DiSandro, Josh Anton, Andie Young, et al. 2017. "Experimental Characterization of the Mechanical Properties of 3D-Printed ABS and Polycarbonate Parts." *Rapid Prototyping Journal* 23 (4): 811–24. https://doi.org/10.1108/RPJ-03-2016-0042.

Chacón, J. M., M. A. Caminero, E. García-Plaza, and P. J. Núñez. 2017. "Additive Manufacturing of PLA Structures Using Fused Deposition Modelling: Effect of Process Parameters on Mechanical Properties and Their Optimal Selection." *Materials and Design* 124: 143–57. https://doi.org/10.1016/j.matdes.2017.03.065.

Clark, Billy, Zhenhuan Zhang, Gordon Christopher, and Michelle L. Pantoya. 2017. "3D Processing and Characterization of Acrylonitrile Butadiene Styrene (ABS) Energetic Thin Films." *Journal of Materials Science* 52 (2): 993–1004. https://doi.org/10.1007/s10853-016-0395-5.

Coppola, Bartolomeo, Nicola Cappetti, Luciano di Maio, Paola Scarfato, and Loredana Incarnato. 2018. "3D Printing of PLA/Clay Nanocomposites: Influence of Printing Temperature on Printed Samples Properties." *Materials* 11 (10). https://doi.org/10.3390/ma11101947.

"Copyright_1992_Porous-Media." n.d.

Cramer, Marcus, and Igor Sevostianov. 2009. "Effect of Pore Distribution on Elastic Stiffness and Fracture Toughness of Porous Materials." *International Journal of Fracture* 160 (2): 189–96. https://doi.org/10.1007/s10704-009-9416-6.

"Designation: D5023 − 07 StandardTest Method for Plastics: Dynamic Mechanical Properties: In Flexure (Three-Point Bending) 1." n.d. https://doi.org/10.1520/D5023-07.

Dizon, John Ryan C., Alejandro H. Espera, Qiyi Chen, and Rigoberto C. Advincula. 2018a. "Mechanical Characterization of 3D-Printed Polymers." *Additive Manufacturing* 20: 44–67. https://doi.org/10.1016/j.addma.2017.12.002.

———. 2018b. "Mechanical Characterization of 3D-Printed Polymers." *Additive Manufacturing* 20: 44–67. https://doi.org/10.1016/j.addma.2017.12.002.

Dorogoy, A., and D. Rittel. 2009. "Determination of the Johnson-Cook Material Parameters Using the SCS Specimen." *Experimental Mechanics* 49 (6): 881–85. https://doi.org/10.1007/s11340-008-9201-x.

Du, Baojiang, Changqin Ji, Ping Chen, Jingmin Guo, Anbo Sun, and Xiong Wei. 2012a. "Study of Tensile Strength Distribution Based on Composite Materials: For

Aeronautical Engineering." *Modern Applied Science* 6 (5): 21–26. https://doi.org/10.5539/mas.v6n5p21.

———. 2012b. "Study of Tensile Strength Distribution Based on Composite Materials: For Aeronautical Engineering." *Modern Applied Science* 6 (5): 21–26. https://doi.org/10.5539/mas.v6n5p21.

Farbman, Daniel, and Chris McCoy. 2016. "Materials Testing of 3D Printed ABS and PLA Samples to Guide Mechanical Design." In *ASME 2016 11th International Manufacturing Science and Engineering Conference, MSEC 2016*. Vol. 2. American Society of Mechanical Engineers. https://doi.org/10.1115/MSEC2016-8668.

Ghosh, Amitava. n.d. "A FORTRAN Program for ®tting Weibull Distribution and Generating Samples." http://www.iamg.org/CGEditor/.

Gibson, Ian, Thomas Kvan, and Ling Wai Ming. 2002. "Rapid Prototyping for Architectural Models." *Rapid Prototyping Journal* 8 (2): 91–99. https://doi.org/10.1108/13552540210420961.

Gomes, F., J. Xavier, and H. Koerber. 2019. "High Strain Rate Compressive Behaviour of Wood on the Transverse Plane." In *Procedia Structural Integrity*, 17:900–905. Elsevier B.V. https://doi.org/10.1016/j.prostr.2019.08.120.

Gross, Richard A., and Bhanu Kalra. 2002. "Biodegradable Polymers for the Environment." *Science* 297 (5582): 803–7. https://doi.org/10.1126/science.297.5582.803.

Hoskins, T. J., K. D. Dearn, and S. N. Kukureka. 2018. "Mechanical Performance of PEEK Produced by Additive Manufacturing." *Polymer Testing* 70 (August): 511–19. https://doi.org/10.1016/j.polymertesting.2018.08.008.

Hosur, M. v., J. Alexander, U. K. Vaidya, and S. Jeelani. 2001. "High Strain Rate Compression Response of Carbon/Epoxy Laminate Composites." *Composite Structures* 52 (3–4): 405–17. https://doi.org/10.1016/S0263-8223(01)00031-9.

Ilankeeran, Prasanna Kumar, Preetamkumar M. Mohite, and Sudhir Kamle. 2012. "Axial Tensile Testing of Single Fibres." *Modern Mechanical Engineering* 02 (04): 151–56. https://doi.org/10.4236/mme.2012.24020.

ISO 17296-2. 2015. "INTERNATIONAL STANDARD Additive Manufacturing — General Principles —" 2015.

Jašo, Vladislav, Gregory Glenn, Artur Klamczynski, and Zoran S. Petrović. 2015. "Biodegradability Study of Polylactic Acid/ Thermoplastic Polyurethane Blends." *Polymer Testing* 47: 1–3. https://doi.org/10.1016/j.polymertesting.2015.07.011.

Joffe, R., J. Andersons, and E. Sparniņš. 2009. "Applicability of Weibull Strength Distribution for Cellulose Fibers with Highly Non-Linear Behaviour." *ICCM International Conferences on Composite Materials*, no. December 2013.

Joffe, R, J Andersons, and E Spārniņš. n.d. "APPLICABILITY OF WEIBULL STRENGTH DISTRIBUTION FOR CELLULOSE FIBERS WITH HIGHLY NON-LINEAR BEHAVIOUR."

Kim, Heechang, Eunju Park, Suhyun Kim, Bumsoo Park, Namhun Kim, and Seungchul Lee. 2017. “Experimental Study on Mechanical Properties of Single- and Dual-Material 3D Printed Products.” In *Procedia Manufacturing*, 10:887–97. Elsevier B.V. https://doi.org/10.1016/j.promfg.2017.07.076.

Kumar, Ashish, T. Venkatappa Rao, S. Ray Chowdhury, and S. V.S. Ramana Reddy. 2017. “Compatibility Confirmation and Refinement of Thermal and Mechanical Properties of Poly (Lactic Acid)/Poly (Ethylene-Co-Glycidyl Methacrylate) Blend Reinforced by Hexagonal Boron Nitride.” *Reactive and Functional Polymers* 117 (August): 1–9. https://doi.org/10.1016/j.reactfunctpolym.2017.05.005.

Kuznetsov, Vladimir E., Alexey N. Solonin, Oleg D. Urzhumtsev, Richard Schilling, and Azamat G. Tavitov. 2018. “Strength of PLA Components Fabricated with Fused Deposition Technology Using a Desktop 3D Printer as a Function of Geometrical Parameters of the Process.” *Polymers* 10 (3). https://doi.org/10.3390/polym10030313.

Letcher, Todd, and Megan Waytashek. 2014. “Material Property Testing of 3D-Printed Specimen in Pla on an Entry-Level 3D Printer.” In *ASME International Mechanical Engineering Congress and Exposition, Proceedings (IMECE)*. Vol. 2A. American Society of Mechanical Engineers (ASME). https://doi.org/10.1115/IMECE2014-39379.

Li, L., Q. Sun, C. Bellehumeur, and P. Gu. 2002. “Composite Modeling and Analysis for Fabrication of FDM Prototypes with Locally Controlled Properties.” *Journal of Manufacturing Processes* 4 (2): 129–41. https://doi.org/10.1016/S1526-6125(02)70139-4.

Li, Li, and Michel Aubertin. 2003. “A General Relationship between Porosity and Uniaxial Strength of Engineering Materials.” *Canadian Journal of Civil Engineering* 30 (4): 644–58. https://doi.org/10.1139/l03-012.

Li, Xin, Ying Yan, Licheng Guo, and Chenghai Xu. 2016. “Effect of Strain Rate on the Mechanical Properties of Carbon/Epoxy Composites under Quasi-Static and Dynamic Loadings.” *Polymer Testing* 52 (July): 254–64. https://doi.org/10.1016/j.polymertesting.2016.05.002.

Lin, Y. C., and Xiao Min Chen. 2010a. “A Combined Johnson-Cook and Zerilli-Armstrong Model for Hot Compressed Typical High-Strength Alloy Steel.” *Computational Materials Science* 49 (3): 628–33. https://doi.org/10.1016/j.commatsci.2010.06.004.

———. 2010b. “A Combined Johnson-Cook and Zerilli-Armstrong Model for Hot Compressed Typical High-Strength Alloy Steel.” *Computational Materials Science* 49 (3): 628–33. https://doi.org/10.1016/j.commatsci.2010.06.004.

Mascia, Nilson T., and Renan A. Simoni. 2013. “Analysis of Failure Criteria Applied to Wood.” *Engineering Failure Analysis* 35 (December): 703–12. https://doi.org/10.1016/j.engfailanal.2013.07.001.

Mehta, Singh, Priam Pillai, and Lalit Singh Mehta. 2017. “466 Lalit Compression Testing of PLA in 3D Printing.”

Ngo, Tuan D, Alireza Kashani, Gabriele Imbalzano, Kate T Q Nguyen, and David Hui. 2018. “Additive Manufacturing (3D Printing): A Review of Materials , Methods , Applications and Challenges.” *Composites Part B* 143 (December 2017): 172–96. https://doi.org/10.1016/j.compositesb.2018.02.012.

Nur Koç, Merve, Fazil Onder Sonmez, Nuri Ersoy, M Koc, F O Sonmez, N Ersoy, and K Cinar. 2014. “Failure Prediction Capabilities of Composite Failure Criteria under Out-of-Plane Loads Characterisation of Failure in Composite Materials with Acoustic Emission and Correlation with Micromechanics View Project FAILURE PREDICTION CAPABILITIES OF COMPOSITE FAILURE CRITERIA UNDER OUT-OF-PLANE LOADS.” https://www.researchgate.net/publication/289593012.

Nyambeni, Ngeletshedzo, and Boy Raymond Mabuza. 2018. “Considerations of Failure Analysis in a Multi-Layered Composite Structure under Thermomechanical Loading.” In , 447. MDPI AG. https://doi.org/10.3390/icem18-05329.

Olewnik-Kruszkowska, Ewa, Jacek Nowaczyk, and Kornelia Kadac. 2017. “Effect of Compatibilizig Agent on the Properties of Polylactide and Polylactide Based Composite during Ozone Exposure.” *Polymer Testing* 60 (July): 283–92. https://doi.org/10.1016/j.polymertesting.2017.04.009.

Popescu, Diana, Aurelian Zapciu, Catalin Amza, Florin Baciu, and Rodica Marinescu. 2018. “FDM Process Parameters Influence over the Mechanical Properties of Polymer Specimens: A Review.” *Polymer Testing* 69: 157–66. https://doi.org/10.1016/j.polymertesting.2018.05.020.

Pramanik, Brahmananda, and P. Raju Mantena. 2011. “Viscoelastic Response of Graphite Platelet and CTBN Reinforced Vinyl Ester Nanocomposites.” *Materials Sciences and Applications* 02 (11): 1667–74. https://doi.org/10.4236/msa.2011.211222.

Priyanka, G. T.L., Kamlesh Kumar, V. Guru Prathap Reddy, and T. Tadepalli. 2021. “Mechanical Reliability of Extruded PLA Filaments.” *Materialia* 16 (November 2020): 101075. https://doi.org/10.1016/j.mtla.2021.101075.

Raj, S. Aravind, E. Muthukumaran, and K. Jayakrishna. 2018. “A Case Study of 3D Printed PLA and Its Mechanical Properties.” *Materials Today: Proceedings* 5 (5): 11219–26. https://doi.org/10.1016/j.matpr.2018.01.146.

Ryshkewitch, Eugene. n.d. “February 1953 Corn@ression Strength Compression Strength of Porous Sintered Alumina and Zirconia 9th Communication to Ceramography.”

Selmy, A. I., N. A. Azab, and Ma Abd El-Baky. 2014a. “Statistical Analysis of Monotonic Mechanical Properties for Unidirectional Glass Fiber (U)/Random Glass Fiber (R)/Epoxy Hybrid and Non-Hybrid Polymeric Composites.” *Journal of Composite Materials* 48 (4): 455–69. https://doi.org/10.1177/0021998312474046.

———. 2014b. “Statistical Analysis of Monotonic Mechanical Properties for Unidirectional Glass Fiber (U)/Random Glass Fiber (R)/Epoxy Hybrid and Non-

Hybrid Polymeric Composites." *Journal of Composite Materials* 48 (4): 455–69. https://doi.org/10.1177/0021998312474046.

Si, Wan Jie, Li Yang, Yun Xuan Weng, Jiang Zhu, and Jian Bing Zeng. 2018a. "Poly(Lactic Acid)/Biobased Polyurethane Blends with Balanced Mechanical Strength and Toughness." *Polymer Testing* 69 (March): 9–15. https://doi.org/10.1016/j.polymertesting.2018.05.004.

———. 2018b. "Poly(Lactic Acid)/Biobased Polyurethane Blends with Balanced Mechanical Strength and Toughness." *Polymer Testing* 69 (August): 9–15. https://doi.org/10.1016/j.polymertesting.2018.05.004.

Song, Y., Y. Li, W. Song, K. Yee, K. Y. Lee, and V. L. Tagarielli. 2017. "Measurements of the Mechanical Response of Unidirectional 3D-Printed PLA." *Materials and Design* 123: 154–64. https://doi.org/10.1016/j.matdes.2017.03.051.

Sood, Anoop Kumar, R. K. Ohdar, and S. S. Mahapatra. 2010. "Parametric Appraisal of Mechanical Property of Fused Deposition Modelling Processed Parts." *Materials and Design* 31 (1): 287–95. https://doi.org/10.1016/j.matdes.2009.06.016.

"Standard Test Method for Tensile Properties of Plastics 1." n.d. https://doi.org/10.1520/D0638-14.

"Standard Test Method for Tensile Strength and Young's Modulus for High-Modulus Single-Filament Materials 1." n.d.

Sun, Wei, Binil Starly, Andrew Darling, and Connie Gomez. 2004. "Computer-Aided Tissue Engineering: Application to Biomimetic Modelling and Design of Tissue Scaffolds." *Biotechnology and Applied Biochemistry* 39 (1): 49. https://doi.org/10.1042/ba20030109.

Tan, Jin Qiang, Mei Zhan, Shuai Liu, Tao Huang, Jing Guo, and He Yang. 2015. "A Modified Johnson-Cook Model for Tensile Flow Behaviors of 7050-T7451 Aluminum Alloy at High Strain Rates." *Materials Science and Engineering A* 631: 214–19. https://doi.org/10.1016/j.msea.2015.02.010.

Wang, Shuheng, Yongbin Ma, Zichen Deng, Sen Zhang, and Jiaxin Cai. 2020. "Effects of Fused Deposition Modeling Process Parameters on Tensile, Dynamic Mechanical Properties of 3D Printed Polylactic Acid Materials." *Polymer Testing*. https://doi.org/10.1016/j.polymertesting.2020.106483.

Wang, Yanen, Mingju Lei, Qinghua Wei, Yanmei Wang, Juan Zhang, Ying Guo, and Jabran Saroia. 2020. "3D Printing Biocompatible L-Arg/GNPs/PLA Nanocomposites with Enhanced Mechanical Property and Thermal Stability." *Journal of Materials Science* 55 (12): 5064–78. https://doi.org/10.1007/s10853-020-04353-8.

Wu, Wenzheng, Peng Geng, Guiwei Li, Di Zhao, Haibo Zhang, and Ji Zhao. 2015. "Influence of Layer Thickness and Raster Angle on the Mechanical Properties of 3D-Printed PEEK and a Comparative Mechanical Study between PEEK and ABS." *Materials* 8 (9): 5834–46. https://doi.org/10.3390/ma8095271.

Ziemian, Constance, Mala Sharma, and Sophia Ziemian. n.d. “7 Anisotropic Mechanical Properties of ABS Parts Fabricated by Fused Deposition Modelling.” www.intechopen.com.

APPENDIX-A

Matlab code for failure criteria

```
Xdata=[28.85 0 -18.10 -66.97 0 28.05];
Ydata=[0 20.81 18.10 0 -53.80 -28.05];
plot(Xdata,Ydata,'X','color','r','LineWidth',1)
hold on
plot([-66.97 28.86 28.86 -66.97 -66.97],[20.81 20.81 -53.80 -53.80
20.81],'m','LineWidth',2) %(Max stress)
plot([0 28.86 28.86 0 -66.97 -66.97 0],[20.81 20.81 0 -53.80 -53.80 0
20.81],'--','color','b','LineWidth',2) %(Tresca)
grid on
hold on
f1=@(x,y,z)   x.^2/1932.759   +   y.^2/1119.879   -   (x.*y)/1502.832+
z.^2/101.1219+(x)/50.71062+(y)/33.94025-1;
fimplicit3(f1,[-200         200         -200         200         -200
200],'edgeColor','r','FaceAlpha',.1,'LineStyle',':') %(Tsai-Wu)
hold on
f1=@(x,y,z)   x.^2/1932.759   +   y.^2/1119.879   -   (x.*y)/1502.832+
z.^2/101.1219+(x)/50.71062+(y)/33.94025-1;
fimplicit3(f1,[-200         200         -200         200         -200
200],'edgeColor','r','FaceAlpha',.01,'LineStyle',':') %(Tsai-Wu)
hold on
f1=@(x,y,z)   x.^2/832.8419   +   y.^2/433.1589   -   (x.*y)/832.8419+
z.^2/101.1219 -1;
f2=@(x,y,z)   x.^2/4485.316   +   y.^2/433.1589   -   (x.*y)/4484.316+
z.^2/101.1219 -1;
f3=@(x,y,z)   x.^2/4485.316   +   y.^2/2895.308   -   (x.*y)/4484.316+
z.^2/101.1219 -1;
f4=@(x,y,z)   x.^2/832.8419   +   y.^2/2895.308   -   (x.*y)/832.8419+
z.^2/101.1219 -1;
fimplicit3(f1,[0          100          0          100          -100
100],'edgeColor','b','FaceAlpha',.1,'LineStyle','-.') %(Tsai-Hill)
hold on
fimplicit3(f2,[-100          0          0          100          -100
100],'edgeColor','b','FaceAlpha',.1,'LineStyle','-.') %(Tsai-Hill)
hold on
fimplicit3(f3,[-100          0          -100          0          -100
100],'edgeColor','b','FaceAlpha',.1,'LineStyle','-.') %(Tsai-Hill)
```

```
hold on
fimplicit3(f4,[0 100 -100 0 -100
100],'edgeColor','b','FaceAlpha',.1,'LineStyle','-.') %(Tsai-Hill)
hold on
f1=@(x,y,z) x.^2/1932.759 + y.^2/1119.879 - (x.*y)/1932.759+
z.^2/101.1219+(x)/50.71062+(y)/33.94025-1;
fimplicit3(f1,[-100 100 -100 100 -100
100],'edgeColor','k','FaceAlpha',.01,'LineStyle','---') %(Hoffman)
hold on
f1=@(x,y,z) x.^2/832.842 + y.^2/433.1589 - (x.*y)/1201.25+
z.^2/101.1219 -1;
f2=@(x,y,z) x.^2/4485.316 + y.^2/433.1589 - (x.*y)/1393.864+
z.^2/101.1219 -1;
f3=@(x,y,z) x.^2/4485.316 + y.^2/2895.308 - (x.*y)/3603.66+
z.^2/101.1219 -1;
f4=@(x,y,z) x.^2/832.8419 + y.^2/2895.308 - (x.*y)/1552.847+
z.^2/101.1219 -1;
fimplicit3(f1,[0 200 0 200 -200
200],'edgeColor','m','FaceAlpha',.9,'LineStyle','---') %(Norris)
hold on
fimplicit3(f2,[-200 0 0 200 -200
200],'edgeColor','m','FaceAlpha',.9,'LineStyle','---') %(Norris)
hold on
fimplicit3(f3,[-200 0 -200 0 -200
200],'edgeColor','m','FaceAlpha',.9,'LineStyle','---') %(Norris)
hold on
fimplicit3(f4,[0 200 -200 0 -200
200],'edgeColor','m','FaceAlpha',.9,'LineStyle','---') %(Norris)
hold on
plot([-140 40], [0 0],'k','LineWidth',1.5)
plot([0 0], [-100 40],'k','LineWidth',1.5)
legend('Average','Hoffman','Tsai-Wu','Norris','Rankine','Tresca')
text (-130,-80,"Tsai-Wu",'color','r','LineWidth',1.5)
%text (-75,-68,"Hoffman",'color','k','LineWidth',1.5)
text (20,-57,"Rankine",'color','m','LineWidth',1.5)
text (20,-20,"Tresca",'color','b','LineWidth',1.5)
```